Structure, Dynamics, and Reactivity of Co_3O_4 Spinel Interacting with 2-Propanol and Water: Insights from Ab Initio Molecular Dynamics Simulations

Der Fakultät für Chemie der Universität Duisburg-Essen
vorgelegte
Dissertation
zur Erlangung des akademischen Grades eines Doktors der Naturwissenschaft (Dr. rer. nat.)

von
Amir Hossein Omranpoor
aus Juybar, Iran

June 2023

Erstgutachter:	Prof. Dr. Eckhard Spohr
Zweitgutachterin:	Prof. Dr. Marialore Sulpizi
Vorsitzender:	Prof. Dr. Michael Giese
Datum der mündlichen Prüfung:	18. August 2023

DOI: 10.17185/duepublico/78959
URN: urn:nbn:de:hbz:465-20230905-104234-8

Hiermit versichere ich, die vorliegende Dissertation selbstständig, ohne fremde Hilfe und ohne Benutzung anderer als den angegebenen Quellen angefertigt zu haben. Alle aus fremden Werken direkt oder indirekt übernommenen Stellen sind als solche gekennzeichnet. Die vorliegende Dissertation wurde in keinem anderen Promotionsverfahren eingereicht. Mit dieser Arbeit strebe ich die Erlangung des akademischen Grades Doktor der Naturwissenschaften (Dr. rer. nat.) an.

---

26 June 2023

Publications

1. A. H. Omranpoor, A. Bera, D. Bullert, M. Linke, S. Salamon, S. Webers, H. Wende, E. Hasselbrink, E. Spohr, and S. Kenmoe. "2-Propanol interacting with Co_3O_4 (001): A combined vSFS and AIMD study". *The Journal of Chemical Physics*, **2023** (doi:10.1063/5.0142707).

2. A. H. Omranpoor, T. Kox, E. Spohr, and S. Kenmoe. "Influence of temperature, surface composition and electrochemical environment on 2-propanol decomposition at the Co_3O_4 (001)/H_2O interface". *Applied Surface Science Advances*, **2022** (doi:10.1016/j.apsadv.2022.100319).

3. D. H. Douma, K. Nchimi Nono, A. H. Omranpoor, A. Lamperti, A. Debernardi, and S. Kenmoe. "Probing the local environment of active sites during 2-propanol oxidation to acetone on the Co_3O_4 (001) surface: insights from first principles O K-edge XANES spectroscopy". *The Journal of Physical Chemistry C*, **2023** (doi:10.1021/acs.jpcc.2c08959).

4. T. Kox, A. H. Omranpoor, and S. Kenmoe. "Structure and Reactivity of $CoFe_2O_4$ (001) Surfaces in Contact with a Thin Water Film". *Physchem*, **2022**. (doi:10.3390/physchem2040023).

Abstract

Heterogeneous catalysis plays a crucial role in the chemical industry, accounting for approximately 25% of industrial chemical production. Transition metal oxides (TMOs) have gained increasing attention as heterogeneous catalysts due to their abundance and lower cost compared to noble metal catalysts. Moreover, conducting oxidation reactions in the liquid phase instead of the gas phase offers several advantages, including milder reaction conditions and catalyst reusability. However, the transition from the metal/gas interface to the TMO/liquid interface introduces a new level of complexity that is challenging to investigate in detail using conventional experimental techniques. Ab initio Molecular Dynamics (AIMD) simulations have emerged as a powerful tool for studying these complex interfaces and capturing their dynamics at the atomistic level. Therefore, this study utilizes AIMD simulations to investigate the oxidation of 2-propanol at the Co_3O_4 (001)/H_2O interface. The choice of 2-propanol as a model reaction allows for the detailed study of a reaction that is complex enough to yield various products but simple enough to be thoroughly examined.

Quantum-mechanical Density Functional Theory with a Hubbard U value (DFT+U) is employed to describe the electronic structure of the Co_3O_4 spinel. The interaction between Co_3O_4 (001) and 2-propanol is thoroughly investigated, considering the influence of different parameters such as temperature, hydroxylation, and surface termination on the structure and activity of the interface. The activity of the Co_3O_4 (001) surface is then compared with that of the Co_3O_4 (111) and Co_3O_4 (110) surfaces. The partial oxidation of 2-propanol is explored in both the liquid and gas phases. In the liquid phase, the impact of temperature, electrochemical conditions, and surface structure is taken into account. Various stages of 2-propanol oxidation are examined through charge analysis. The favorability of the B-terminated Co_3O_4 (001) surface for 2-propanol oxidation is discussed. Additionally, the oxidation process in the gas phase is studied by incorporating a true oxidizing agent, such as oxygen species. Furthermore, the fundamental differences between the partial oxidation of 2-propanol in the liquid and gas phases are elucidated.

Zusammenfassung

Die heterogene Katalyse spielt eine entscheidende Rolle in der chemischen Industrie und macht etwa 25% der industriellen chemischen Produktion aus. Übergangsmetall-Oxide (TMOs) haben aufgrund ihrer Häufigkeit und geringeren Kosten im Vergleich zu Edelmetall-Katalysatoren zunehmend an Bedeutung gewonnen. Die Durchführung von Oxidationsreaktionen in der Flüssigphase bietet dabei Vorteile wie mildere Reaktionsbedingungen und die Wieder-verwendbarkeit des Katalysators. Allerdings führt der Übergang von der Metall /Gas-Grenzfläche zur TMO/Flüssig-Grenzfläche zu einer neuen Komplexität, die mit herkömmlichen experimentellen Techniken nur schwer detailliert untersucht werden kann. Ab initio-Molekulardynamik (AIMD)-Simulationen sind ein leistungsstarkes Werkzeug zur Untersuchung dieser komplexen Grenzflächen auf atomarer Ebene. Daher werden in dieser Studie AIMD Simulationen eingesetzt, um die Oxidation von 2-Propanol an der Co_3O_4 (001)/H_2O– Grenzfläche zu untersuchen. Die Wahl von 2-Propanol als Modellreaktion ermöglicht eine detaillierte Untersuchung einer Reaktion, die sowohl vielfältige Produkte erzeugt als auch gründlich untersucht werden kann und hinreichend einfach für eine theoretische untersuchung auf hohem Niveau ist.

Quantenmechanische Dichtefunktionaltheorie mit einem Hubbard U-Wert (DFT+U) wird verwendet, um die elektronische Struktur des Co_3O_4-Spinells zu beschreiben. Die Wechselwirkung zwischen Co_3O_4 (001) und 2-Propanol wird dabei gründlich untersucht, wobei Einflussfaktoren wie Temperatur, Hydroxylierung und Oberflächenabschluss auf die Struktur und Aktivität der Grenzfläche berücksichtigt werden. Die Aktivität der Co_3O_4 (001)-Oberfläche wird mit der von Co_3O_4 (111)- und Co_3O_4 (110)-Oberflächen verglichen. Die teilweise Oxidation von 2-Propanol wird sowohl in der Flüssig- als auch in der Gasphase untersucht, wobei Temperatur, elektrochemische Bedingungen und Oberflächenstruktur in der Flüssigphase berücksichtigt werden. Unterschiedliche Stadien der 2-Propanol-Oxidation werden durch Ladungsanalyse untersucht. Die Vorzüge der B-terminierten Co_3O_4 (001)-Oberfläche für die 2-Propanol-Oxidation wird diskutiert. Zudem wird der Oxidationsprozess in der Gasphase unter Verwendung eines echten Oxidationsmittels wie eine adsorbierten atomaren Sauerstoffspezies untersucht.

“ πάντα ῥεῖ ” (Panta rhei)
Everything flows.

Heraclitus

If the core message of this Ph.D. thesis were to be condensed into one statement, it would be as follows:

The traditional “structure–reactivity” paradigm in the field of heterogeneous catalysis should be revised to a more comprehensive “structure–dynamics–reactivity” paradigm.

Contents

Abbreviations

DFT	Density Functional Theory
AIMD	Ab Initio Molecular Dynamics
DOS	Density Of States
FCC	Face Centered Cubic
GGA	Generalized Gradient Approximation
LDA	Local Density Approximation
MD	Molecular Dynamics
PES	Potential Energy Surface
BOMD	Born-Oppenheimer Molecular Dynamics
GPW	Gaussian Plane Waves
KS	Kohn-Sham
PBE	Perdew-Burke-Ernzherhof
RDF	Radial Distribution Function
SCF	Self Consistent Field
VACF	Velocity Auto-Correlation Function
XC	Exchange and Correlation
vSFG	Vibrational Sum-Frequency Generation
TMO	Transition Metal Oxide
HPA	Hirshfeld Population Analysis
MPA	Mulliken Population Analysis
CDD	Charge Density Difference

1 Introduction

1.1 Overview

The use of catalysts is a fundamental aspect of many chemical processes and has significant implications in various fields, including industrial manufacturing, environmental science, and medicine, to name just a few. Catalysis is the science and technology of altering the rates of chemical reactions.[90] A substance known as a catalyst can do so by reducing the activation energy required for the reaction to occur, without itself being consumed or permanently altered in the process. This allows even a small amount of catalyst material to transform a large amount of reactant under milder conditions. Furthermore, if more than one reaction product is possible, the catalyst can alter the product distribution, enabling control of the selectivity of a chemical reaction. In order to obtain the desired products, catalysts must frequently prevent reactions from producing unwanted byproducts. Thus, the notion that catalysts solely accelerate reaction rates is a misnomer since they often have to impede reactions from generating such undesired products.[90]

In this chapter, the purpose is to provide a concise overview of the motivations behind this thesis. Firstly, in section 1.2, the rationale for employing transition metal oxides (TMOs) as catalysts is briefly discussed. Section 1.3 emphasizes the significance of selective oxidation of alcohols. However, due to the vast array of materials and molecules falling under the categories of TMOs and alcohols, it is not feasible to investigate them all within a single study. Therefore, this research focuses on exploring the utilization of Co_3O_4 as the catalyst material and 2-propanol as the molecule for the oxidation reaction. The scientific basis for these choices is explained in detail.

In section 1.4, a comprehensive description of the essential structure and characteristics of a Co_3O_4 spinel is provided. Subsequently, section 1.5 discusses previous studies that have employed Co_3O_4 for 2-propanol oxidation, highlighting the existing knowledge in this area. The strategy employed in this work is explained in section 1.6, outlining the approach taken to address the research objectives. Finally, section 1.7 presents an outline of the thesis, providing a preview of the subsequent chapters and their contents.

1.2 Heterogeneous Catalysis on Transition Metal Oxide

Transition metal oxides (TMOs) have emerged as a promising class of catalysts in heterogeneous catalysis due to their abundance, cost-effectiveness, and potential for high catalytic activity. These materials display diverse non-stoichiometric behaviors stemming from their partially filled 3d electron shells, which create opportunities for redox reactions and the formation of oxygen vacancies. One prominent example is oxygen-deficient perovskite oxides, which have garnered considerable attention for their oxygen storage capac-

ity and redox properties, making them valuable for total oxidation reactions.[98] Similarly, cation-deficient perovskites with oxygen defects exhibit enhanced electronic and oxygen ion mobility, rendering them suitable catalysts for reactions involving oxygen transfer.[98]

Despite advancements in understanding the catalytic activity of TMOs, significant challenges persist in fully elucidating the intricate relationship between their structure, composition, and reactivity, particularly at the solid-liquid interface. While volcano curves have been derived for certain mixed oxide systems, the complexity of TMOs and the limited experimental access to the solid-liquid interface impede a comprehensive understanding of their catalytic behavior. Moreover, reactions involving hydrocarbons often occur on intricate and multi-component catalysts, featuring multiple reaction pathways and inherent selectivity challenges.[75] Therefore, gaining a deeper understanding of the true structure and dynamic nature of TMO catalysts is crucial to fully exploit their potential as alternative catalysts to noble metals across a range of reactions.

1.3 Selective Oxidation of Alcohols

The selective oxidation of primary alcohols plays a crucial role in environmentally friendly synthesis of organic oxygenated compounds. While formaldehyde is commercially produced from methanol using mixed oxide catalysts in the gas phase, the aerobic oxidation of other alcohols to produce value-added chemicals, such as acetals, presents challenges and often requires complex multi-step processes.[75] Glycerol, for instance, has garnered attention as a starting material for the production of commodity chemicals,[59] with oxidative dehydrogenation to acrylic acid being a notable target. Acrylic acid is widely used as a monomer for the production of resins and superabsorbents.[74]

To optimize the efficiency and economics of these reactions, various factors must be considered, including the choice of reaction medium, batch vs. flow operation, oxidant selection, and catalyst design. Utilizing O_2 as an abundant and sustainable oxidant is desirable, but its activation poses challenges.[94] Different catalytic approaches, such as thermocatalysis, electrocatalysis, or photocatalysis, can be employed to drive these reactions, each presenting its own set of challenges and research questions. Understanding the phenomena occurring at the solid-liquid interface is essential for developing systematic approaches to study different catalysts, particularly through in-operando techniques.[75] Furthermore, exploring new materials with tailored properties in terms of activity, selectivity, and stability is a critical aspect of advancing catalysis research.

In this study, the selective oxidation of 2-propanol has been chosen as the model reaction for investigation. This selection is motivated by the relative simplicity of 2-propanol oxidation, allowing for a detailed examination of the underlying reaction mechanism, while still exhibiting sufficient complexity to yield diverse reaction products. The possible reactions involved in the gas-phase oxidation of 2-propanol are illustrated in Figure 1.

The desired outcome of this selective oxidation, namely the production of acetone and hydrogen, is achieved through the dehydrogenation of 2-propanol, which interacts with strongly basic and moderately acidic sites in its vicinity. The catalytic sites responsible for oxidative dehydrogenation also facilitate the oxidation of 2-propanol to acetone and water as coupled reaction products. Additionally, under the influence of strongly acidic sites near weakly basic sites, dehydration occurs, leading to the formation of propene and water. At elevated temperatures, total oxidation occurs, resulting in the generation of CO_2 as the primary reaction product.[29,89]

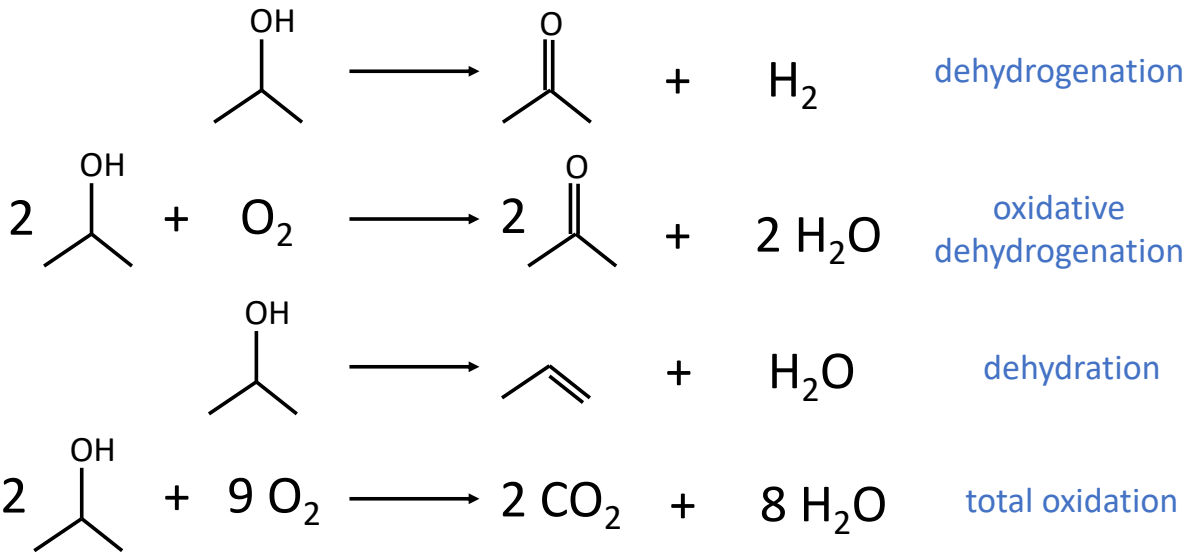

Figure 1: Possible reactions[29,89] for 2-propanol oxidation.

1.4 Co_3O_4 Spinel

Co_3O_4 has demonstrated great promise for various applications in energy and environmental fields due to its efficiency as a catalyst for water oxidation,[57] methane combustion,[54] CO oxidation,[104] as well as its use in lithium-ion batteries and gas sensors.[67] Among its various forms, Co_3O_4 spinel has received considerable attention for promoting oxidation reactions, particularly the selective oxidation of hydrocarbons.[101,49,33] Moreover, the diverse electronic, magnetic, and redox properties of Co_3O_4 have sparked numerous studies in recent years.[6,27,105,7,60,28]

In terms of crystal structure, Co_3O_4 adopts the cubic normal spinel structure, where cobalt ions exist in two different oxidation states, Co^{2+} and Co^{3+}. These ions occupy interstitial tetrahedral and octahedral sites, respectively, within the face-centered cubic (FCC) lattice formed by oxygen ions (see Figure 2 (a)).

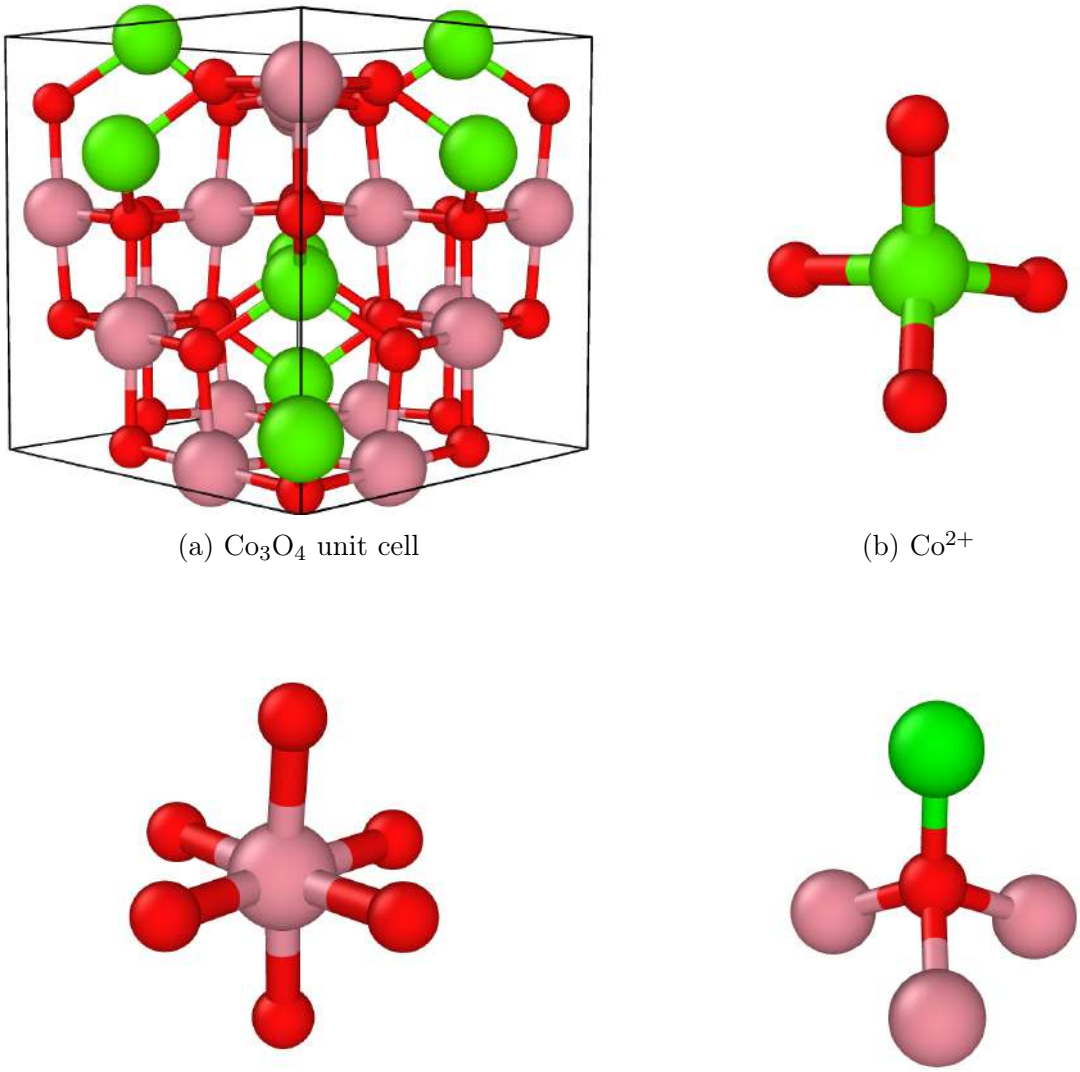

(a) Co_3O_4 unit cell

(b) Co^{2+}

(c) Co^{3+}

(d) O^{2-}

Figure 2: Structure of a Co_3O_4 spinel unit cell (a) consisted of tetrahedrally coordinated Co^{2+} ions (b), octahedrally coordinated Co^{3+} ions (c) and tetrahedrally coordinated O^{2-} ions (d) (Co^{2+} (green), Co^{3+} (pink) and O^{2-} (red)).

The crystal fields at these sites cause a splitting of the five degenerate atomic d orbitals into two groups, resulting in three unpaired d electrons on Co^{2+}, while all the d electrons of Co^{3+} are paired (see Figure 3). At room temperature, Co_3O_4 exhibits paramagnetic semiconductor behavior and transitions to an antiferromagnetic state below $T_N \approx 40$.[87] The antiferromagnetism is primarily attributed to weak coupling between nearest neighboring Co^{2+} ions. The conductivity of Co^{3+} is typically p-type at low temperatures and becomes intrinsic at high temperatures,[63] while the band gap is approximately 1.6 eV.[61,92]

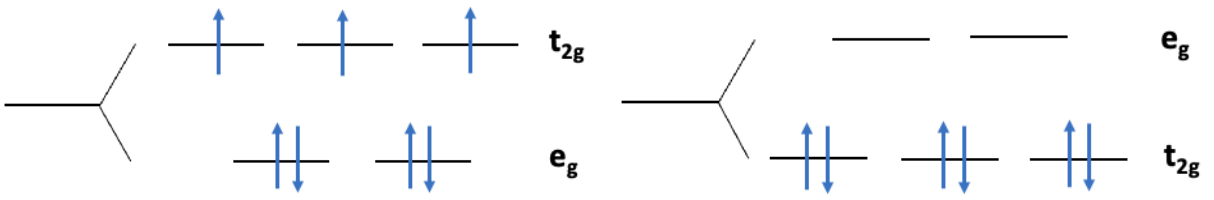

(a) Co^{2+} d7 configuration (b) Co^{3+} d6 configuration

Figure 3: Schematic diagram of crystal field splitting of the tetrahedrally coordinated Co^{2+} ion (a) and the octahedrally coordinated Co^{3+} ion (b).

The surface termination of bulk Co_3O_4 crystals can vary depending on the cutting plane, leading to different terminations. The nomenclature used for these terminations is based on the dominant cobalt ionic species present on the surface. The B-terminated surface is characterized by the prevalence of Co^{3+} ions, whereas the A-terminated surface consists of a mixture of Co^{3+} and Co^{2+} ions. For example, Figure 4 illustrates these two possible surface terminations for the Co_3O_4 (001) surface. Chapters 5 and 6 of this work will investigate how these distinct surface terminations influence the surface properties and its interaction with external adsorbates.

Despite extensive experimental investigations of 2-propanol oxidation on Co_3O_4 (001), the impact of different surface terminations has not been fully explored. Previous research[64] has demonstrated a significant difference in the stability and selectivity of A-terminated and B-terminated surfaces in water decomposition on Co_3O_4 (001), attributed to the distinct nature of Co^{2+} and Co^{3+} active sites.

1.5 Co_3O_4 Spinel as a Catalyst for Selective Oxidation of 2-propanol

Co_3O_4 spinel is a promising catalyst for a wide range of chemical reactions, particularly the selective oxidation of alcohols, which has been the focus of several recent studies.[6,27,105,7] For example, Anke et al.[6] investigated the gas-phase selective oxidation of 2-propanol on bulk Co_3O_4 and observed high activity and selectivity. They found that the highest conversion rates of 2-propanol to acetone occurs at temperatures between 373 K and 573 K, with a maximum conversion rate close to 100% achieved at 430 K. Similarly, another study[7] demonstrated the effectiveness of $CoFe_2O_4$ spinel in the selective oxidation of 2-propanol.

In a study by Falk et al.,[32] the oxidation of 2-propanol was examined on $Co_{1+x}Fe_{2-x}O_4$ spinel oxides in contact with both liquid and gas phases. They found that the catalytic activity increased with increasing Co content, indicating that iron-free Co_3O_4 samples exhibited the highest activity. XPS analysis further revealed that Co^{3+} sites were more active than Co^{2+} sites. Anke et al.[6] investigated the gas-phase oxidation of 2-propanol over Co_3O_4 nanoparticles and found that Co_3O_4 spinel displayed high activity and selectivity. In their study, theoretical investigations employing density functional theory

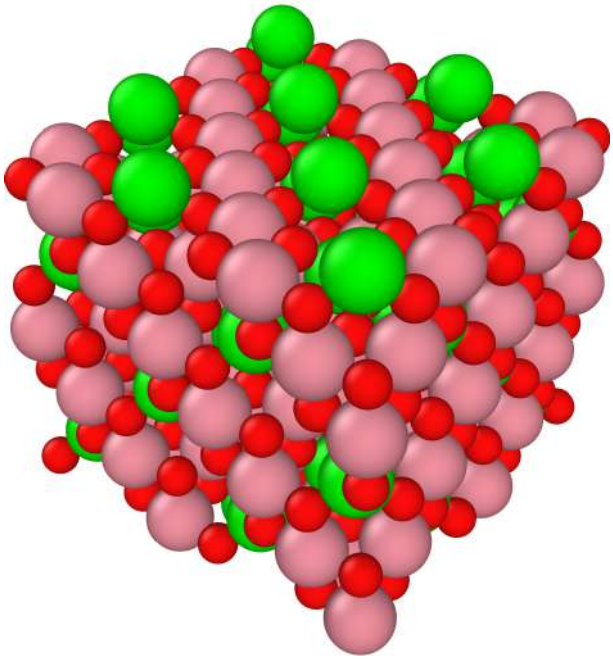

(a) A-terminated Co_3O_4 (001) surface

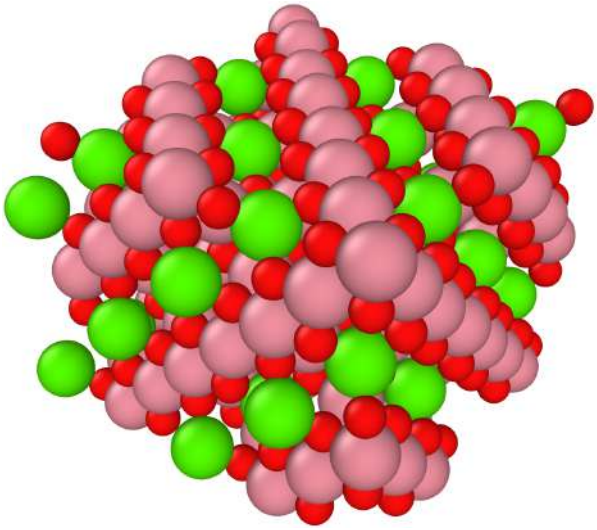

(b) B-terminated Co_3O_4 (001) surface

Figure 4: Two possible surface terminations for a Co_3O_4 (001) surface: (a) A-terminated Co_3O_4 (001) surface and (b) A-terminated Co_3O_4 (001) surface (Co^{2+} (green), Co^{3+} (pink) and O^{2-} (red)).

(DFT) method suggested a preference for a Langmuir-Hinshelwood mechanism on the Co_3O_4(001) surface.

In another study, Falk et al.[31] examined Co_3O_4 nanospheres with a preferential (110) surface orientation and reported complete conversion and 100% selectivity for 2-propanol oxidation to acetone at 430 K. In contrast to the theoretical finding for the (001) surface orientation, they proposed a preferential Mars-van Krevelen mechanism for the (110) surface.

In a more recent work by Zerebecki et al.,[106] a laser-doping technique was employed

to introduce iron cations into Co_3O_4 catalyst particles. The concentration of the laser-imprinted dopant on the surface was correlated with the catalyst's catalytic activity and selectivity. The doped catalysts exhibited enhanced activity with increasing doping depth, establishing a correlation between the laser-imprinted dopant surface concentration and catalytic activity. The doped catalysts were evaluated for 2-propanol gas-phase oxidation and liquid-phase electrochemical OER.

Despite the valuable insight gained from previous experimental and theoretical studies, several important questions regarding the selective oxidation of 2-propanol using Co_3O_4 spinel as a catalyst remain unanswered or only partially addressed. These questions pertain to the characterization of active sites and reaction mechanisms, the role of single versus multiple active sites, the oxidation states of cobalt ions during and after the reaction, and the similarities and differences between liquid-phase and gas-phase oxidation. Additionally, a comprehensive understanding of the dynamics of Co_3O_4/2-propanol and Co_3O_4/water interactions, as well as the influence of adsorbate concentration, temperature, and pH, is yet to be achieved.

This thesis aims to address some of these unanswered questions, or at least provide insights into them, through the utilization of various theoretical and computational techniques. The ultimate objective is to attain a thorough atomistic-level understanding of the fundamental mechanisms governing the selective oxidation of 2-propanol over Co_3O_4 spinel, which could potentially lead to the development of improved catalysts and more efficient industrial processes.

1.6 Strategy

This thesis is part of the CRC/TRR 247 project titled "Heterogeneous Oxidation Catalysis in the Liquid Phase". While traditional catalytic processes in the industry have typically utilized (noble) metal catalysts in the gas phase, using oxidants such as dioxygen, the objective of the CRC/TRR 247 project is to shift towards employing transition metal oxide catalysts in the liquid phase. This transition is motivated by the abundance and lower cost of transition metal oxides, as well as the potential for milder oxidation environments, reducing energy costs and enabling catalyst reusability. Such a shift introduces complexity in two dimensions: transitioning from noble metals to transition metal oxides, and moving from the gas phase to the liquid phase (Figure 5). Consequently, the complexity of the interface will be significantly increased.

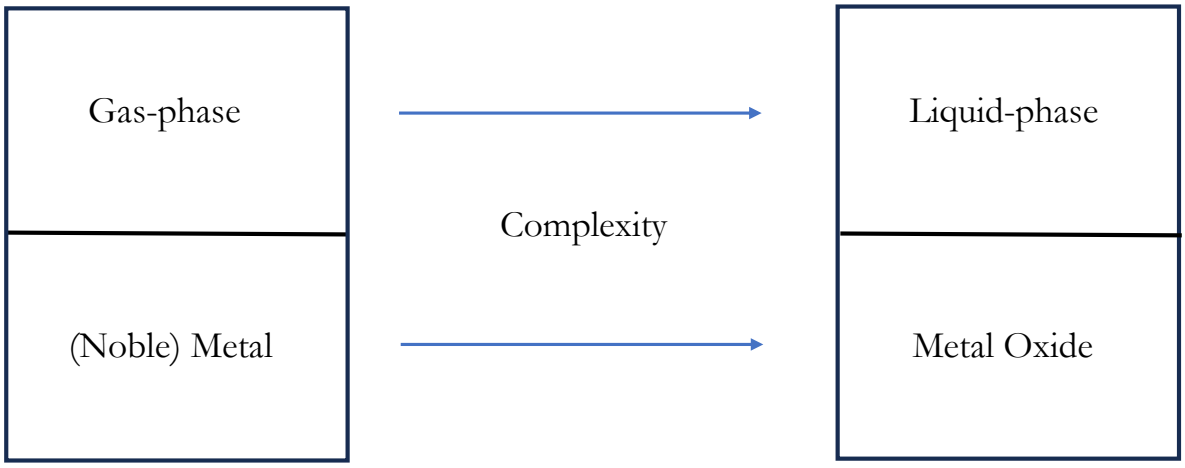

Figure 5: Illustration depicting the objective of the CRC/TRR 247 project: transitioning from the conventional utilization of metal catalysts in the gas phase to a more complex system of transition metal oxide catalysts in the liquid phase. This transition involves an increase in complexity at multiple levels, spanning from the shift in phase (gas to liquid) and the transition from metal catalysts to transition metal oxides. Consequently, the complexity of the interface will be significantly increased.

The study of these complex interfaces presents challenges for many experimental techniques, particularly when aiming for an *in operando* understanding at the atomic level. Atomistic simulation techniques, such as ab initio Molecular Dynamics, are therefore indispensable for studying such intricate interfaces.

Figure 6 illustrates the strategy employed in this work to gradually increase the system's complexity, approaching the objectives of the CRC/TRR 247 project as closely as possible. In Figure 6 (a), the bulk Co_3O_4 spinel is depicted, representing the system with the lowest complexity yet bearing crucial importance as the foundational system for more intricate interfaces. This system is explored in Chapter 4. Figure 6 (b) showcases the B-terminated Co_3O_4 (001)/water interface, which has been previously studied by Kox et al.[64] and will not be extensively discussed in this thesis. Chapter 5 focuses on the B-terminated Co_3O_4 (001)/2-propanol interface, as depicted in Figure 6 (c). Lastly, Chapter 6 of this thesis centers around the B-terminated Co_3O_4 (001)/water/2-propanol interface (Figure 6 (d)), where a 2-propanol molecule is immersed in an aqueous solution. This interface represents the highest level of complexity within the scope of this work.

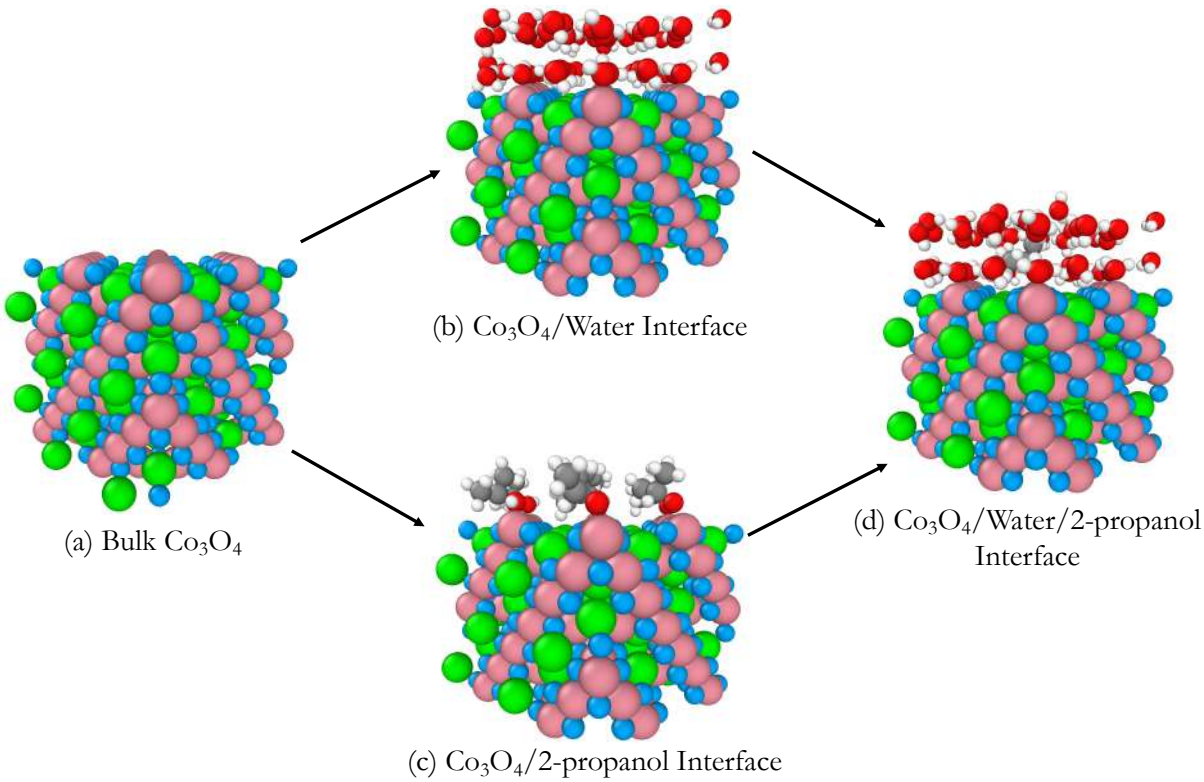

Figure 6: Schematic representation of the strategy employed in this study: (a) Bulk Co_3O_4 spinel, (b) B-terminated Co_3O_4 (001)/water interface, (c) B-terminated Co_3O_4 (001)/2-propanol interface, and (d) B-terminated Co_3O_4 (001)/water/2-propanol interface. The system's complexity increases from left to right. Co^{3+} (pink), Co^{2+} (green), O in Co_3O_4 (blue), O in 2-propanol and water (red), C (gray) and H (white).

1.7 Outline of This Thesis

Chapter 2 discusses the theoretical foundations of the methodology employed in this study, namely quantum-mechanical Density Functional Theory (DFT), Molecular Dynamics (MD), and ab initio Molecular Dynamics (AIMD). It provides a concise overview of how AIMD, in its Born-Oppenheimer implementation, combines approximate quantum mechanical calculations (DFT) to calculate forces and classical dynamics (Newton's equation of motion) to simulate the dynamics of the system.

Chapter 3 focuses on the parameters utilized in this study for setting up the simulations. It specifically addresses the construction of simulation cells and outlines the DFT and MD parameters employed to establish the AIMD simulations.

In Chapter 4, the results pertaining to the electronic and structural properties of the bulk Co_3O_4 spinel are presented. This includes calculated values for lattice parameters, band gap, and density of states. Additionally, this chapter serves as a validation of the model by assessing its ability to accurately represent the Co_3O_4 spinel's characteristics. The stability of the lattice parameter and the Hirshfeld and Mulliken population analyses

are also provided.

Chapter 5 delves into the dynamics of the interface between Co_3O_4 spinel and 2-peopanol molecules. This chapter examines the influence of various parameters such as temperature, surface hydroxylation, and surface structure. While the primary focus is on the Co_3O_4 (001) surface, some preliminary work on the Co_3O_4 (011) and Co_3O_4 (111) surfaces is also discussed. The activity of these surfaces for 2-propanol dissociation is compared, and the chapter concludes with a comparison of the power spectra of 2-propanol adsorbate species on these surfaces with that of a gas-phase 2-propanol molecule.

Chapter 6 investigates the catalytic properties of the Co_3O_4 (001) surface for the partial oxidation of 2-propanol. It explores the effects of various physical and chemical parameters on the oxidation reaction, such as temperature, electrochemical environment, and surface termination. The chapter discusses the adsorption geometry of different systems in detail and explains the four stages of the partial oxidation of 2-propanol, supplemented by charge analysis. To account for the realistic impact of temperature on 2-propanol oxidation, oxygen species are introduced into the system, and the gas-phase oxidation of 2-propanol is discussed. This chapter also highlights the major differences between 2-propanol oxidation in the liquid phase and gas phase, including the formation of acetone and water at high temperatures.

The final chapter, Chapter 7, provides the main conclusions drawn from this work. It summarizes the key findings and insights obtained throughout the study.

2 Theoretical Foundations

2.1 Molecular Dynamics

2.1.1 Overview

Molecular dynamics (MD)[35,97,20,45] is a simulation method that allows the study of the time evolution of a system of interacting particles, such as atoms or molecules, based on classical mechanics. The term "classical" here refers to the fact that the nuclear motion of the particles follows the laws of classical mechanics. The method is based on numerically solving the equations of motion for all particles in the system, using a numerical integration algorithm to propagate the system forward in time.

In MD simulations, the system is typically represented as a collection of point masses, each representing an atom or a group of atoms, and described by their positions and velocities at a given time. The forces acting on each particle are computed based on the interatomic potential energy surface, which can be derived from empirical, semi-empirical or first principle methods. The integration algorithm then updates the positions and velocities of the particles based on the forces, using a finite time step.

MD simulations share many similarities with real experiments.[35] In a typical experimental setup, we prepare a sample of the material we want to investigate, connect it to a measuring instrument, and measure the property of interest over a certain time interval. As measurements are typically affected by statistical noise, longer averaging times result in more accurate results. MD simulations follow a similar procedure. A model system consisting of N particles is selected, and Newton's equations of motion are solved until the system's properties reach a steady state (equilibration). Subsequently, the properties of interest can be measured. It is worth noting that mistakes made in MD simulations may also resemble those made in real experiments, such as incorrect sample preparation or insufficient measurement duration.

2.1.2 Equations of Motion

In order to explore the configuration space and study the dynamics of a classical many-body system, the motions of the nuclei can be calculated using Newton's equation of motion, based on the potential energy surface (PES) $E(\mathbf{R})$,

$$\mathbf{F}_A = M_A \ddot{\mathbf{R}}_A \tag{1}$$

with the force $\mathbf{F}_A$, mass M_A, and acceleration $\ddot{\mathbf{R}}_A$ of nucleus A. The force acting on a nucleus is calculated by taking the negative derivative of the PES with respect to its position, $\mathbf{R}_A$.

$$\mathbf{F}_A = -\frac{\partial E\left(\{\mathbf{R}_A\}\right)}{\partial \mathbf{R}_A} \tag{2}$$

However, it is not feasible to solve the many-body system analytically, so the MD method[1,2] is used to numerically integrate the coupled differential equations using finite time steps and algorithms such as position Verlet,[99] velocity Verlet,[95] leapfrog,[51] Beeman's,[10] or Gear predictor-corrector.[36]

2.1.3 Integrating the Equations of Motion

In the frequently applied velocity Verlet algorithm both position $\mathbf{R}_A$ and velocity $\mathbf{v}_A$ are explicitly propagated in time t

$$\mathbf{R}_A(t+\delta t) = \mathbf{R}_A(t) + \mathbf{v}_A(t)\delta t + \frac{\mathbf{F}_A(t)}{2M_A}\delta t^2 \tag{3}$$

$$\mathbf{v}_A(t+\delta t) = \mathbf{v}_A(t) + \frac{\mathbf{F}_A(t) + \mathbf{F}_A(t+\delta t)}{2M_A}\delta t \tag{4}$$

The position $\mathbf{R}_A(t+\delta t)$ (equation 3) obtained from the MD simulations can then be utilized to compute the forces $\mathbf{F}_A(t+\delta t)$ (equation 4) required for the velocity $\mathbf{v}_A(t+\delta t)$ (equation 2). To initiate the simulation, an initial atomic configuration and a distribution of initial velocities are necessary. The former is dictated by the system under study, while the latter can be derived by setting random velocity from the Maxwell-Boltzmann distribution at a given initial temperature. The velocity Verlet algorithm is time-reversible and conserves the system's phase space and angular momentum.

2.1.4 Lyapunov Instability

The trajectories that are generated by the MD simulations are highly sensitive to the initial conditions. For instance, let us consider the position ($\mathbf{R}_A$) of one of the N nuclei at time t. The position of this nucleus is a function of the initial positions and momenta at $t = 0$:

$$\mathbf{R}(t) = f\left[\mathbf{R}_A(0), \mathbf{P}_A(0); t\right] \tag{5}$$

If we were to perturb the initial conditions by a small amount ϵ, such as altering some of the momenta, the resulting position at time t would differ from the original. Hence, we would have a distinct value for $\mathbf{R}$ at time t:

$$\mathbf{R}'(t) = f\left[\mathbf{R}_A(0), \mathbf{P}_A(0) + \boldsymbol{\epsilon}; t\right] \tag{6}$$

$\Delta\mathbf{R}(t)$ represents the disparity between $\mathbf{R}(t)$ and $\mathbf{R}'(t)$. When considering short intervals, $\Delta\mathbf{R}(t)$ is proportional to ϵ in a linear fashion. Nevertheless, the coefficient for this linear

relationship diverge exponentially:

$$|\Delta\mathbf{R}(t)| \sim \epsilon \exp(\lambda t) \tag{7}$$

This so-called Lyapunov instability is the reason why we cannot predict a trajectory with accuracy unless it is a short simulation. The Lyapunov exponent, also known as the largest Lyapunov exponent, out of the $6N$ exponents, governs the long-term exponential divergence of initially close trajectories. To restrict $|\Delta\mathbf{R}(t)|$ within $0 < t < t_{\max}$ to a specified bound $\Delta_{\max}$, the maximum allowable initial error (ϵ) can be deduced from equation 7:

$$\epsilon \sim \Delta_{\max} \exp\left(-\lambda t_{\max}\right) \tag{8}$$

Consequently, the admissible deviation in our initial conditions diminishes exponentially as the duration of the run, $t_{\max}$, increases.[35] However, although Lyapunov instability implies that individual trajectories may display unstable behavior, the reliability of MD simulations does not solely rely on the stability of individual trajectories. Instead, reliability is evaluated through statistical analysis and ensemble averaging over multiple trajectories.

2.1.5 Statistical Ensembles

A statistical ensemble refers to a collection of possible states that a physical system can be in, where each state has a specific probability of occurrence. In statistical mechanics, this concept is used to describe how a large collection of particles or a system behaves, considering its microscopic properties such as energy and momentum, as well as macroscopic properties like temperature and pressure. There are different types of statistical ensembles that are characterized by specific macroscopic constraints, such as the number of particles, total energy, or temperature, which affect the probability distribution of the system's microstates.[35,37]

The microcanonical ensemble, also known as the NVE ensemble, is one such ensemble where the system's number of particles and total energy are fixed, and each member of the ensemble has the same total energy and particle number. For the system to remain in statistical equilibrium, it's total energy must be conserved.[37]

The canonical ensemble, also known as the NVT ensemble, is another type of statistical ensemble where the number of particles is fixed, but the energy is not precisely known. In this case, the temperature is specified, and the ensemble is used to describe a closed system that has been in contact with a heat bath. In a typical MD simulation, a thermostat is required to simulate a canonical (NVT) ensemble. For instance, the Andersen,[3] Berendsen,[12] Nosé-Hoover,[77,78,53] and Nosé-Hoover chain thermostats.[69] The well-established Nosé-Hoover thermostat extends the $6N$-dimensional phase space by two

artificial degrees of freedom simulating a coupling to a heat bath.

Lastly, the grand canonical ensemble or μVT ensemble is a statistical ensemble where neither the particle number nor the energy is fixed. Instead, the temperature and chemical potential are specified, and it is used to describe an open system that has been in weak contact with a reservoir through thermal, chemical, radiative, electrical, or other contacts.[37]

2.2 Density Functional Theory

2.2.1 Foundations of Density Functional Theory

The Many-Body Problem

The state of a quantum mechanical system, defined as a function of particle positions and spins, $\mathbf{x}$, and time t, is represented by a wave function $\Psi(\mathbf{x}, t)$.[48,16,15] A non-relativistic description of the system's time evolution can be defined from the time-dependent Schrödinger equation. This equation is represented by:[91]

$$\hat{H}(\mathbf{x}, t)\Psi(\mathbf{x}, t) = i\hbar\frac{\partial\Psi(\mathbf{x}, t)}{\partial t}, \tag{9}$$

where $\hat{H}$ is the Hamiltonian operator and $\hbar$ is the reduced Planck constant. When the Hamiltonian is not explicitly time-independent, the space and time dependence of the wave function can be separated, yielding the time-independent Schrödinger equation:

$$\hat{H}(\mathbf{x})\Psi(\mathbf{x}) = E\Psi(\mathbf{x}) \tag{10}$$

where E is the energy of stationary eigenstates. The probability density of the particles is given by the square of the absolute value of the wave function $|\Psi(\mathbf{x})|^2$.[15]
A system consisting of N nuclei and n electrons can be described by the Hamiltonian:

$$\hat{H} = \underbrace{-\frac{1}{2}\sum_{A=1}^{N}\frac{1}{M_A}\nabla_A^2}_{\hat{T}_\mathrm{N}} \underbrace{-\frac{1}{2}\sum_{i=1}^{n}\nabla_i^2}_{\hat{T}_\mathrm{e}} \underbrace{-\sum_{A=1}^{N}\sum_{i=1}^{n}\frac{Z_A}{r_{Ai}}}_{V_\mathrm{Ne}} \underbrace{\sum_{i=1}^{n}\sum_{j>i}^{n}\frac{1}{r_{ij}}}_{V_\mathrm{ee}} \underbrace{\sum_{A=1}^{N}\sum_{B>A}^{N}\frac{Z_A Z_B}{R_{AB}}}_{V_\mathrm{NN}} \tag{11}$$

where M, Z, R, and r are nuclear masses, charges, distances, and nucleus-electron and electron-electron distances in atomic units, respectively. The Hamiltonian contains the kinetic energy operators of nuclei, $\hat{T}_\mathrm{N}$, and electrons, $\hat{T}_\mathrm{e}$, as well as the potential energy operators of nucleus-electron, V_Ne, electron-electron, V_ee, and nucleus-nucleus, V_NN, interactions. The mass difference between nuclei and electrons enables a separation of their motions, allowing for an adiabatic description of the Born-Oppenheimer approximation.[14] In this description, the electrons move in a temporarily static field of nuclei, i.e., $\hat{T}_\mathrm{N} = 0$. This description yields the electronic Hamiltonian:

$$\hat{H}_{\mathrm{el}}(\mathbf{r}) = \hat{T}_{\mathrm{e}}(\mathbf{r}) + V_{\mathrm{Ne}}(\mathbf{r}) + V_{\mathrm{ee}}(\mathbf{r}) + V_{\mathrm{NN}} \tag{12}$$

where, V_{NN} is a constant term that depends on the fixed nuclear positions, which can be interpreted as the instantaneous molecular structure. Solving the electronic Schrödinger equation for various nuclear positions yields the potential energy surface (PES) $E(\mathbf{R})$, which describes the energy of an electronic state as a function of the molecular structure. To solve the electronic Schrödinger equation, the variational principle can be used[86]

$$E_0 \leq E_{\mathrm{trial}} = \langle \Phi(\mathbf{x}) | \hat{H}(\mathbf{x}) | \Phi(\mathbf{x}) \rangle \tag{13}$$

This principle states that the expectation value of the Hamiltonian for a normalized trial wave function $\Phi(\mathbf{x})$ cannot be lower than the exact ground state energy E_0.

Hohenberg-Kohn Theorems

The computational effort can be significantly reduced by replacing the $4n$-dimensional electronic wave function with the three-dimensional electron density in real space,

$$\rho(\mathbf{r}) = n \int \dots \int |\Psi(\mathbf{x})|^2 \, \mathrm{d}s_1 \, \mathrm{d}\mathbf{x}_2 \dots \mathrm{d}\mathbf{x}_n \tag{14}$$

where $\Psi(\mathbf{x})$ is the wave function of the system with n electrons and $\mathbf{x}$ is the set of all electron coordinates, spin coordinates, and nuclear coordinates. The electron density is obtained by integrating $|\Psi(\mathbf{x})|^2$ over all coordinates except for one electron's spatial coordinates. This density fully characterizes the system due to the existence of cusps at nuclear positions that provide information about nuclear charges.

Density functional theory (DFT) is based on the two Hohenberg-Kohn theorems.[52] The first theorem states that the ground state electron density is a unique functional of the electronic Hamiltonian since two different nuclear arrangements cannot yield the same ground state electron density. The second theorem states that the ground state electron density can be obtained using the variational principle, since the electron density uniquely defines the Hamiltonian and consequently the wave function. The electronic ground state energy,

$$E[\rho_0] = T[\rho_0] + E_{\mathrm{Ne}}[\rho_0] + E_{\mathrm{ee}}[\rho_0] + V_{\mathrm{NN}} \tag{15}$$

includes the kinetic energy of the electrons T, and the potential energies of nucleus-electron E_{Ne} and electron-electron E_{ee} interactions as a functional of the ground state electron density ρ_0.

Kohn-Sham Method

The interaction between the nucleus and electrons is described in the Kohn-Sham approach:[62]

$$E_{\mathrm{Ne}}\left[\rho_0\right] = \int V_{\mathrm{Ne}}\rho_0(\mathbf{r})\mathrm{d}\mathbf{r} \tag{16}$$

and the classical portion of the Coulomb energy resulting from electron-electron interaction is also considered:

$$J\left[\rho_0\right] = \frac{1}{2}\iint \frac{\rho_0\left(\mathbf{r}_1\right)\rho_0\left(\mathbf{r}_2\right)}{r_{12}}\,\mathrm{d}\mathbf{r}_1\,\mathrm{d}\mathbf{r}_2 \tag{17}$$

are derived exactly using the electron density. To compute the kinetic energy of a non-interacting reference system with the same electron density, one-electron orbitals ϕ_i are introduced, forming a Slater determinant:[93]

$$T_{\mathrm{S}}\left[\rho_0\right] = -\frac{1}{2}\sum_{i=1}^{n}\left\langle\phi_i(\mathbf{r})\left|\nabla^2\right|\phi_i(\mathbf{r})\right\rangle \tag{18}$$

An effective potential is used to incorporate indirect interactions among the Kohn-Sham orbitals to emulate the electron density of the real system, while the direct Coulomb repulsion among the electrons is not considered. The exchange-correlation functional is a combined representation of the non-classical aspects of the electron-electron interaction, including exchange, correlation, and self-interaction correction, as well as the difference in kinetic energy between the non-interacting reference system and the real system:

$$E_{\mathrm{xc}}\left[\rho_0\right] = \left(E_{\mathrm{ee}}\left[\rho_0\right] - J\left[\rho_0\right]\right) + \left(T\left[\rho_0\right] - T_{\mathrm{S}}\left[\rho_0\right]\right) \tag{19}$$

To summarize, the primary components of the energy functional for the ground state are:

$$E\left[\rho_0\right] = T_{\mathrm{S}}\left[\rho_0\right] + E_{\mathrm{Ne}}\left[\rho_0\right] + J\left[\rho_0\right] + E_{\mathrm{xc}}\left[\rho_0\right] + V_{\mathrm{NN}} \tag{20}$$

All the components of the energy functional for the ground state, except for the exchange-correlation functional, are accurately known. The Kohn-Sham equations are employed to determine the Kohn-Sham orbitals:

$$\begin{aligned}\hat{f}_{\mathrm{KS}}\phi_i\left(\mathbf{r}_1\right) =& \left(-\frac{1}{2}\nabla^2 - \sum_{A=1}^{N}\frac{Z_A}{r_{A1}} + \sum_{j=1}^{n}\int\frac{\left|\phi_j\left(\mathbf{r}_2\right)\right|^2}{r_{12}}\,\mathrm{d}\mathbf{r}_2 + \frac{\partial E_{\mathrm{xc}}\left[\rho_0(\mathbf{r})\right]}{\partial\rho_0(\mathbf{r})}\right)\phi_i\left(\mathbf{r}_1\right) \\ =& \epsilon_i\phi_i\left(\mathbf{r}_1\right)\end{aligned} \tag{21}$$

where the Kohn-Sham operator $\hat{f}_{\mathrm{KS}}$ and orbital eigenvalues ϵ_i, can be solved through a self-consistent approach. A basis set expansion can be utilized to describe the Kohn-Sham orbitals of molecular systems:

$$\phi_i(\mathbf{r}) = \sum_{\mu} c_{\mu i} \chi_\mu(\mathbf{r}) \tag{22}$$

by using atom-centered Gaussians or numerical atomic orbitals, with basis functions χ_μ and coefficients $c_{\mu i}$. In the case of condensed systems, periodic boundary conditions must be applied. As per Bloch's theorem,[13] the Kohn-Sham orbitals can be constructed through the product of a function that has the same periodicity as the lattice, denoted as $u_{i,\mathbf{k}}$, and a plane wave with any vector $\mathbf{k}$ present in the first Brillouin zone:[44]

$$\phi_{i,\mathbf{k}}(\mathbf{r}) = u_{i,\mathbf{k}}(\mathbf{r}) \exp(\mathrm{i}\mathbf{k}\mathbf{r}) \tag{23}$$

A linear combination of plane waves or periodically replicated atom-centered basis functions can be used to express the function $u_{i,\mathbf{k}}$.

Spin Polarized Density Functional Theory

The densities of electrons with different spins (up and down) in open-shell systems

$$\begin{aligned} \rho^{\uparrow}(\mathbf{r}) &= n \int \dots \int |\Psi(\mathbf{x})|^2 \, \mathrm{d}\mathbf{x}_2 \dots \mathrm{d}\mathbf{x}_n \quad \text{for } s_1 = +\frac{1}{2}, \\ \rho^{\downarrow}(\mathbf{r}) &= n \int \dots \int |\Psi(\mathbf{x})|^2 \, \mathrm{d}\mathbf{x}_2 \dots \mathrm{d}\mathbf{x}_n \quad \text{for } s_1 = -\frac{1}{2} \end{aligned} \tag{24}$$

are considered separately to account for spin density difference and, thus, spin polarization. This approach is supported by an extension of the first Hohenberg-Kohn theorem,[100,81,43] which shows that it is possible to calculate the lowest energy state of each symmetry:

$$E^{\mathrm{u}}\left[\rho^{\uparrow}, \rho^{\downarrow}\right] = T_{\mathrm{S}}^{\mathrm{u}}\left[\rho^{\uparrow}, \rho^{\downarrow}\right] + E_{\mathrm{Ne}}[\rho] + J[\rho] + E_{\mathrm{xc}}^{\mathrm{u}}\left[\rho^{\uparrow}, \rho^{\downarrow}\right] \tag{25}$$

2.2.2 Exchange-Correlation Functionals

Jacob's Ladder of Exchange-Correlation Functionals

The Kohn-Sham Density Functional Theory (DFT) is fundamentally exact, but since the exchange-correlation functional is unknown,[18,76,85] approximate functionals must be utilized.[84] Several functionals have been proposed in recent decades, which can be ordered in a hierarchy with an increasing level of accuracy. However, a systematic improvement of these functionals is not possible. The simplest approach is the Local Density Approximation (LDA), which has a local dependence on the electron density. The Generalized Gradient Approximation (GGA) includes the reduced density gradient to account for the local inhomogeneity of the electron density. The Meta-GGA method introduces a dependence on the kinetic energy density. Orbital-dependent approaches, such as hy-

brid methods, introduce exact Hartree-Fock exchange.[46,34] Double-hybrid methods add a correlation contribution using second-order Møller-Plesset perturbation theory (MP2).[71] Alternatively, the DFT+U method,[4] which adds a Hubbard-like term with parameter U to LDA and GGA functionals, can be used to improve the description of the strong on-site Coulomb interaction of localized electrons.

Generalized Gradient Approximation (GGA)

In real systems, the density of electrons $n(\boldsymbol{r})$ varies across space, but the Local Density Approximation (LDA) only considers the density at a specific point. This limitation can be overcome by using Generalized Gradient Approximations (GGA), which include information about the local gradient of the exchange-correlation density. The GGA functional is given by the equation:

$$E_{XC}[n] \approx E_{XC}^{GGA} := \int d^3\boldsymbol{r} n(\boldsymbol{r}) \epsilon_{XC}\left(n, \nabla n, \nabla^2 n, \ldots\right) \tag{26}$$

Over the three decades, various types of GGA have been proposed, with the PW91[103,83] and PBE[82] functionals being the most commonly used. GGAs generally provide better results than LDA for describing ground-state energies, molecular binding energies, hydrogen bonds, and simple metal lattice constants. However, GGAs still have shortcomings, such as the inability to describe dispersion interactions, an underestimation of bond strengths, and an unphysical exponential decay of the electrostatic potential above surfaces.

2.2.3 Hubbard-U Correction

Overview

One of the limitations of Density Functional Theory is its failure in describing strongly correlated materials, such as many transition metal oxides that are insulators, but are predicted to be conductive by DFT. The underestimation of the bandgap of these materials can be explained by the over-delocalization of the highly correlated electrons in the d-orbitals and f-orbitals, which results from the self-interaction of the electrons that does not completely cancel within the LDA and the GGA functionals.

One approach to improving the description of these materials is by using hybrid functionals. Hybrid functionals incorporate the exact exchange interaction, leading to a better cancellation of the self-interaction. However, calculating the exact exchange is computationally demanding, making the use of hybrid functionals feasible only for small systems. To address this issue, the DFT+U model was developed, inspired by the Hubbard model used in band theory to correctly describe Mott insulators. The Hubbard model considers the Coulomb repulsion for electrons, but only for electrons that are at the same atom, the on-site interaction. In the DFT+U model, the on-site Hubbard-like interaction E_{Hub} is added to the DFT energy E_{DFT}. However, the Coulomb interaction of electrons at the

same atom is already included in an average manner in the DFT term, which results in double counting. Therefore, a double counting term E_{DC} must be subtracted:

$$E_{DFT+U}[n(r)] = E_{DFT}[n(r)] + E_{Hub}\left[\left\{n^{I\sigma}_{m,m'}\right\}\right] - E_{DC}\left[\left\{n^{I\sigma}\right\}\right] \tag{27}$$

The Hubbard term is reliant on the atomic orbital occupations $n^{I\sigma}_{m,m'}$, where the site (atom) index I and the orbital index m are taken into consideration. The averaged interaction is defined by summing the orbital occupation $n^{I\sigma}$ for the atom I.
Multiple methods exist for defining these orbital occupations, including atomic orbitals, Wannier functions, and Mulliken population. However, the most commonly used method involves defining them as projections of occupied Kohn-Sham orbitals ψ^{σ}_{kv} onto local basis function sets ϕ^{I}_{m}:

$$n^{I\sigma}_{m,m'} = \sum_{k,v} f^{\sigma}_{k,v} < \psi^{\sigma}_{k,v} \left|\phi^{I}_{m'}\right>\left<\phi^{I}_{m}\right| \psi^{\sigma}_{k,v} > \tag{28}$$

The term $f^{\sigma}_{k,v}$ is the Fermi-Dirac occupation of the Kohn-Sham orbital with the k-point k and the band index v.
There are different formulations for the DFT+U terms in use, the most common method is:

$$\begin{aligned} E_U\left[\left\{n^{I\sigma}_{m,m'}\right\}\right] &= E_{Hub}\left[\left\{n^{I\sigma}_{m,m'}\right\}\right] - E_{DC}\left[\left\{n^{I\sigma}\right\}\right] \\ &= \textstyle\sum_{I,\sigma} \frac{U^I}{2} \operatorname{Tr}\left[n^{I\sigma} - \left(n^{I\sigma}\right)^2\right] \end{aligned} \tag{29}$$

The meaning of these terms is that the value of the parameter U^I is used to scale the Coulomb interaction of the localized orbitals that are occupied minus the Coulomb interaction of the average occupied orbitals. This scaling results in a penalty for orbitals that are half-occupied, causing less-than-half filled orbitals to be destabilized and more-than-half filled orbitals to be stabilized.[5,68]

Linear Response Method

One way of calculating the Hubbard$-U$ value from first principle is to use linear response theory.[24] Linear response theory is based on the premise that, in a crystal, atoms can only exchange integer numbers of electrons. Consequently, fractional occupation is only possible as a statistical mixture of fully occupied orbitals, and not through fractional occupation of individual orbitals. The energy of a system with fractional occupation, denoted by E_n, depends on the energies of two states: E_N, which corresponds to a state with N electrons, and E_{N+1}, which corresponds to a state with $N+1$ electrons, as well as the statistical weight ω associated with E_{N+1}.
The relationship between the energies of the three states can be expressed mathematically as follows:

$$E_n = (1-\omega)E_N + \omega E_{N+1} \tag{30}$$

The energy difference between the two states depends linearly on ω, which is observed in exact DFT. However, LDA and GGA show a non-linear energy dependency for fractional occupation.

The goal of the linear response method is to scale the U-value in such a way that it compensates for the incorrect total energy description in LDA and GGA. This is accomplished by constraining the occupation of localized orbitals on one atom in a supercell and examining the energy dependency on the occupation. However, the energy cost of localization is not the only contribution to the total energy. Another factor to consider is the rehybridization that occurs when a different occupation is constrained. To separate this effect from the total energy, the method of Lagrange multipliers is used to constrain the orbital occupation of Kohn-Sham orbitals, denoted by q_I.

$$\begin{aligned} E\left[\{q_I\}\right] &= \min\left\{E[n(r)] + \sum_I \lambda\left(n_I - q_I\right)\right\} \\ E^{KS}\left[\{q_I\}\right] &= \min\left\{E^{KS}[n(r)] + \sum_I \lambda^{KS}\left(n_I - q_I\right)\right\} \end{aligned} \tag{31}$$

The U-value can be determined by calculating the difference between the linear response of the total energy and the linear response of the rehybridization.

$$U = \frac{\delta^2 E\left[\{q_I\}\right]}{\delta^2 q_I} - \frac{\delta^2 E^{KS}\left[\{q_I\}\right]}{\delta^2 q_I} \tag{32}$$

An alternative method is employed in practice, which involves the introduction of an independent variable α_I:

$$\begin{aligned} E\left[\{q_I\}\right] &= \min\left\{E[n(r)] + \sum_I \alpha_I n_I\right\} \\ E^{KS}\left[\{q_I\}\right] &= \min\left\{E^{KS}[n(r)] + \sum_I \alpha_I^{KS} n_I\right\} \end{aligned} \tag{33}$$

The given approach provides the response functions as follows:

$$\begin{aligned} \chi_{IJ} &= \frac{\delta^2 E}{\delta\alpha_I \delta\alpha_J} = \frac{\delta n_I}{\delta\alpha_J} \\ \chi_{IJ}^{KS} &= \frac{\delta^2 E^{KS}}{\delta\alpha_I^{KS}\delta\alpha_J^{KS}} = \frac{\delta n_I^{KS}}{\delta\alpha_J^{KS}} \end{aligned} \tag{34}$$

And thus the U-value is calculated as:

$$U = \frac{1}{\chi_{IJ}^{KS}} - \frac{1}{\chi_{IJ}} \tag{35}$$

2.2.4 Dispersion Correction

Overview

London dispersion forces[30] arise from long-range electron correlation effects involving instantaneous dipole-induced dipole interactions. These correlations are weak and not accounted for in semi-local or hybrid DFT, which mainly considers short-range correlations.[42] To address this issue, various semi-classical methods have been developed to incorporate dispersion corrections into DFT, such as DFT-D1 to DFT-D4,[38,39,40,19] Tkatchenko-Scheffler,[96] exchange-hole dipole moment,[9] and local response dispersion.[88] Non-local van der Waals density functionals are another approach to account for these effects.[26]

D3(BJ) Dispersion Correction

The D3[40] dispersion correction using Becke-Johnson damping[58,41] is used in this work. In this method the dispersion corrected energy,

$$E^{\mathrm{DFT-D3(BJ)}} = E^{\mathrm{DFT}} + E^{\mathrm{DFT}}_{\mathrm{D3(BJ)}}, \tag{36}$$

equals the sum of the DFT energy E^{DFT} and the dispersion correction,

$$E^{\mathrm{DFT}}_{\mathrm{D3(BJ)}} = -\frac{1}{2}\sum_{A\neq B}\sum_{n=6,8} s_n \frac{C_n^{AB}}{(R_{AB} + f_{\mathrm{damp}})^n} \tag{37}$$

with the damping function

$$f_{\mathrm{damp}} = a_1\sqrt{\frac{C_8^{AB}}{C_6^{AB}}} + a_2 \tag{38}$$

The specific dispersion coefficients C_n^{AB} between pairs of atoms are determined by fractional coordination numbers, based on their local atomic environment. These coefficients rely on pre-calculated linear-response time-dependent DFT data. The parameter s_6 ensures correct asymptotic behavior. The parameters s_8, a_1, and a_2 can be adjusted for different DFT functionals to optimize the correction in the short- and medium-range, where the DFT functional contributes to the correlation. They also ensure that singularities are avoided at short distances. The parameters are determined by performing a least-squares fit to reference energies from non-covalent interaction benchmark sets, calculated using high-level coupled cluster theory (CCSD(T)).[23] It should be noted that the dispersion correction is not equal to the physical dispersion energy. Three-body corrections, based on the Axilrod-Teller-Muto model,[8] can be added if necessary. A cutoff radius is used to restrict the number of dispersion correction terms for periodic and non-periodic systems that are large.

2.3 Ab Initio Molecular Dynamics

2.3.1 Overview

In Molecular Dynamics (MD), the mathematical objective is to calculate the expectation value $\langle \mathcal{O} \rangle$ of a given operator $\mathcal{O}(\boldsymbol{R}, \boldsymbol{P})$ based on the Boltzmann distribution:[65]

$$\langle \mathcal{O} \rangle = \frac{\int d\boldsymbol{R} d\boldsymbol{P} \mathcal{O}(\boldsymbol{R}, \boldsymbol{P}) e^{-\beta E_{\text{pot}}(\boldsymbol{R}, \boldsymbol{P})}}{\int d\boldsymbol{R} d\boldsymbol{P} e^{-\beta E_{\text{pot}}(\boldsymbol{R}, \boldsymbol{P})}} \tag{39}$$

where $\boldsymbol{R}$ and $\boldsymbol{P}$ represent nuclear positions and momenta, respectively and $\beta = 1/k_{\text{B}}T$ denotes the inverse temperature. The total energy function:

$$E_{\text{pot}}(\boldsymbol{R}, \boldsymbol{P}) = \sum_{I=1}^{N} \frac{\boldsymbol{P}_I^2}{2M_I} + E_{\text{pot}}\left[\{\psi_i\}; \boldsymbol{R}\right] \tag{40}$$

The first term represents the nuclear kinetic energy, $E_{\text{pot}}\left[\{\psi_i\}; \boldsymbol{R}\right]$ represents the potential energy function, N represents the number of nuclei, and M_I represents their corresponding masses.

Assuming the ergodicity hypothesis, the thermal average $\langle \mathcal{O} \rangle$ can be determined not only as an ensemble average of a Monte Carlo (MC) simulation, but also as a temporal average by means of AIMD.[65]

$$\langle \mathcal{O} \rangle = \lim_{\mathcal{T} \to \infty} \frac{1}{\mathcal{T}} \int dt \mathcal{O}(\boldsymbol{R}(t), \boldsymbol{P}(t)), \tag{41}$$

In the context of propagating the classical many-body system in time using Newton's equation of motion, the nuclei are commonly treated as classical, which is usually an inconsequential approximation. Nevertheless, in scenarios involving very light atoms or low temperatures, where nuclear quantum effects can have a notable impact, the application of a quantum formalism like imaginary-time path integrals becomes imperative.

In CP2K,[56] AIMD is available in two schemes: Born-Oppenheimer Molecular Dynamics (BOMD) and second-generation Car-Parrinello Molecular Dynamics (CPMD). However, since this work utilizes only the former, the discussion in the following section will be limited to this method. In the following, it is assumed that the potential energy function is computed on the fly using KS-DFT. This implies that $E_{\text{pot}}\left[\{\psi_i\}; \boldsymbol{R}\right] = E^{\text{KS}}\left[\{\psi_i[\rho(\boldsymbol{r})]\}; \boldsymbol{R}\right] + E_{II}(\boldsymbol{R})$.

2.3.2 Born-Oppenheimer Molecular Dynamics

One way of incorporating electronic structure in molecular dynamics simulations involves solving the static electronic structure problem for each step of the simulation, while holding the nuclear positions constant. This reduces the electronic structure problem to a time-independent quantum problem, such as solving the stationary Schrödinger equation.

The nuclei are then propagated with the calculated forces using classical mechanics so that the time dependence of the electronic structure imposed by its dependence on the classical dynamics of the nuclei. The resulting method, known as Born-Oppenheimer molecular dynamics, can be easily formulated and defined.

$$\begin{aligned} M_I \ddot{\mathbf{R}}_I(t) &= -\nabla_I \min_{\Psi_0} \left\{ \langle \Psi_0 | \mathcal{H}_\mathrm{e} | \Psi_0 \rangle \right\} \\ E_0 \Psi_0 &= \mathcal{H}_\mathrm{e} \Psi_0 \end{aligned} \tag{42}$$

for the electronic ground state.[70] In Born-Oppenheimer MD, at every AIMD step the potential energy $E_\mathrm{pot}\left[\{\psi_i\}; \boldsymbol{R}\right]$ is minimized with respect to $\{\psi_i(\boldsymbol{r})\}$ under the holonomic orthonormality constraints $\langle \psi_i(\boldsymbol{r}) \mid \psi_j(\boldsymbol{r}) \rangle = \delta_{ij}$ which leads to the following Lagrangian:

$$\begin{aligned} \mathcal{L}_\mathrm{BO}\left(\{\psi_i\}; \boldsymbol{R}, \dot{\boldsymbol{R}}\right) =& \frac{1}{2} \sum_{I=1}^{N} M_I \dot{\boldsymbol{R}}_I^2 - \min_{\{\psi_i\}} E_\mathrm{pot}\left[\{\psi_i\}; \boldsymbol{R}\right] \\ &+ \sum_{i,j} \Lambda_{ij} \left(\langle \psi_i \mid \psi_j \rangle - \delta_{ij} \right), \end{aligned} \tag{43}$$

where $\boldsymbol{\Lambda}$ is a Hermitian Lagrangian multiplier matrix. The Euler-Lagrange equations:

$$\begin{aligned} \frac{d}{dt} \frac{\partial \mathcal{L}}{\partial \dot{\boldsymbol{R}}_I} &= \frac{\partial \mathcal{L}}{\partial \boldsymbol{R}_I}, \\ \frac{d}{dt} \frac{\partial \mathcal{L}}{\partial \left\langle \dot{\psi}_i \right|} &= \frac{\partial \mathcal{L}}{\partial \langle \psi_i |}, \end{aligned} \tag{44}$$

can be used to obtain the associated Newtonian equation of motion:

$$\begin{aligned} M_I \ddot{\boldsymbol{R}}_I =& -\nabla_{\boldsymbol{R}_I} \left[\min_{\{\psi_i\}} E_\mathrm{pot}\left[\{\psi_i\}; \boldsymbol{R}\right] \Big|_{\{\langle \psi_i | \psi_j \rangle = \delta_{ij}\}} \right] \\ =& -\frac{\partial E}{\partial \boldsymbol{R}_I} + \sum_{i,j} \Lambda_{ij} \frac{\partial}{\partial \boldsymbol{R}_I} \langle \psi_i \mid \psi_j \rangle \\ & - 2 \sum_i \frac{\partial \langle \psi_i |}{\partial \boldsymbol{R}_I} \left[\frac{\delta E_\mathrm{pot}}{\delta \langle \psi_i |} - \sum_j \Lambda_{ij} | \psi_j \rangle \right] \end{aligned} \tag{45}$$

$$\begin{aligned} 0 \lesssim& -\frac{\delta E_\mathrm{pot}}{\delta \langle \psi_i |} + \sum_j \Lambda_{ij} | \psi_j \rangle \\ =& -\hat{H}_e \left\langle \psi_i \right| + \sum_j \Lambda_{ij} \left| \psi_j \right\rangle \end{aligned} \tag{46}$$

The right-hand side of equation 45 can be decomposed into three components. The initial term is commonly known as the Hellmann-Feynman force. The second term, referred to as the Pulay or wavefunction force, arises from the holonomic orthonormality constraint and is present only when the basis functions have an explicit dependence on the atomic

positions. The final term originates from the implicit reliance of the electronic structure on the atomic positions, and it persists regardless of the chosen basis set. The factor of 2 in equation 45 arises from the assumption that the Kohn-Sham orbitals are real. However, this term becomes null if the orbitals are eigenfunctions of the Hamiltonian within the subspace spanned by the basis set, which is a weaker condition than the original Hellmann-Feynman theorem. The last component of equation 45 is known as the non-self-consistent force, as the eigenfunctions of the Kohn-Sham Hamiltonian are only achieved at exact self-consistency. Unfortunately, achieving exact self-consistency is not feasible in numerical calculations, leading to inconsistent forces and, consequently, the inequality stated in equation 46.[65]

As a consequence of the Born-Oppenheimer (BO) approximation, the electronic and nuclear subsystems are completely decoupled from one another. This adiabatic separation allows for the integration time step to be selected without any additional constraints, allowing it to be chosen up to the limit of nuclear resonance. Remarkably, this remains true regardless of the band gap, meaning that even metals can be treated directly and without complication in principle.

3 Computational Details

When setting up a simulation, there are typically three sequential steps to follow: pre-processing, processing, and post-processing. In this chapter, we will delve into the specifics of the initial structure and parameters necessary for setting up the simulations, focusing on the pre-processing step. As discussed in the previous section, the Born-Oppenheimer Molecular Dynamics simulation can be divided into two distinct parts: calculating forces at each step using quantum mechanical density functional theory, and incorporating these forces into classical equations of motion to determine the system's dynamics. Therefore, in this chapter, we will also address the parameters for calculating forces and dynamics in two separate subsections.

3.1 Simulation Cells

Chapter 1 provides essential information about the Co_3O_4 spinel. To simulate the systems studied in this work, simulation cells are constructed by utilizing the bulk structure of Co_3O_4 spinel and introducing specific surface coverages of 2-propanol molecules, water, or both, along with a vacuum region (Figure 7 (a) and (b)).

For instance, Figure 7 (a) depicts a simulation cell consisting of the B-terminated Co_3O_4 (001) surface covered with 8 2-propanol molecules. The slab is constructed using an orthorhombic supercell with (2x2) periodicity in the lateral directions (x,y), measuring 16.18 Å × 16.18 Å. To prevent interactions between the bottom and top surfaces of the Co_3O_4 slab, a vacuum region of 30 Å is introduced. Figure 7 (b) presents another example featuring the B-terminated Co_3O_4 (001) surface covered by a single 2-propanol molecule, surrounded by an aqueous solution containing 60 water molecules.

In the case of A-terminated and B-terminated (001) surfaces, 11 and 13 layers, respectively, are utilized. The bottom 5 and 6 layers of the slab are held fixed to mimic the bulk behavior of a real Co_3O_4 catalyst.

3.2 Density Functional Theory

Spin-polarized quantum mechanical density functional theory (DFT) is utilized to calculate forces at each step for a given set of nuclear coordinates. All DFT calculations, whether for geometry optimization or ab initio molecular dynamics simulation, are conducted using the CP2K/Quickstep package.[65]

To account for exchange and correlation effects, the Generalized Gradient Approximation (GGA) within the PBE formulation[82] is employed. Additionally, a U correction of the Hubbard type[55] is included to accurately describe the Co $3d$ states. The value of U for both Co^{2+} and Co^{3+} ions is set to 2 eV, as adapted from a previous study.[64] This U value will be shown in the next chapter to adequately capture the band gap of Co_3O_4, which

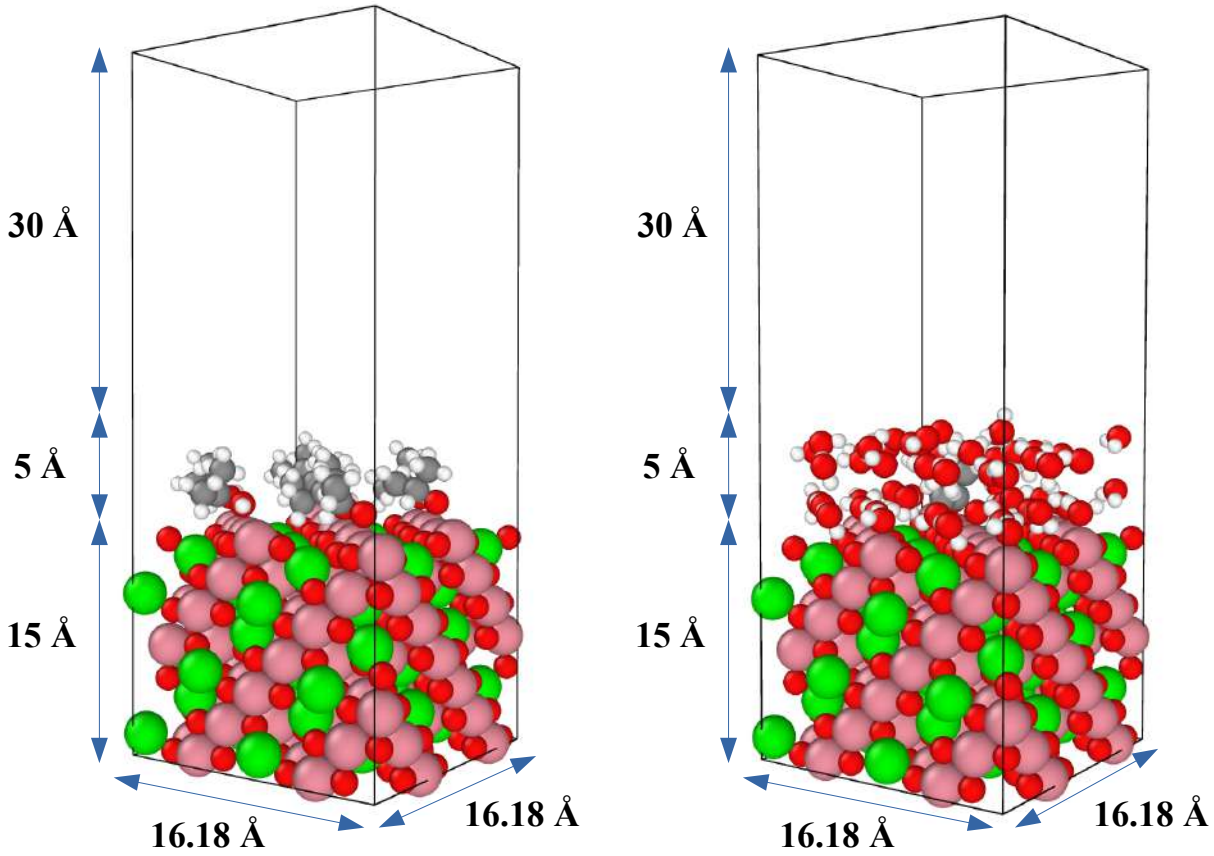

(a) (b)

Figure 7: Simulation cell consisted of the B-terminated Co_3O_4 (001) surface: (a) covered by eight 2-propanol molecules and (b) covered by a single 2-propanol molecule solvated in aqueous solution. (Co^{2+} (green), Co^{3+} (pink), O^{2-} (red), C (gray) and H (white)).

is of significant importance. Moreover, the Grimme D3 correction[40] is incorporated into the PBE exchange-correlation functional to consider dispersion interactions, particularly in the water films.

For treatment of core electrons, Goedecker-Teter-Hutter (GTH) pseudopotentials are employed. The $2s$ and $2p$ electrons of oxygen, and the $3s$, $3p$, $3d$, and $4s$ electrons of cobalt are considered as valence electrons. The basis sets used in this study consist of plane wave functions with an energy cutoff of 500 Ry and a double-ζ quality local basis set with a single set of polarization functions (DZVP) in mixed representation. The same type of pseudopotentials (GTH) and polarization functions (DZVP) are also utilized for carbon and hydrogen atoms.

Due to the asymmetry of the slab and the one-sided adsorption of liquid film molecules, a dipole correction as described by Bengtsson[11] and implemented in the CP2K/Quickstep package is introduced in the Z direction to counteract the artificial electric field.

3.3 Ab Initio Molecular Dynamics

To investigate the dynamics of interactions, ab initio molecular dynamics (AIMD) simulations based on the Born-Oppenheimer scheme (BOMD) are performed using the CP2K/ Quickstep package.[65] These simulations are conducted at the Γ point for all simulations in this work, unless stated otherwise. Forces are calculated from density functional theory, as described in Chapter 2, to integrate Newton's equations of motion.

To achieve system equilibration, the canonical ensemble (NVT) is utilized. NVT conditions are imposed on the system using a Nosé-Hoover thermostat with a time constant of 1 ps and target temperatures ranging from 300 K to 450 K.

The simulations are conducted for a production phase of approximately 20 ps, utilizing a simulation time step of 0.5 fs after an initial equilibration period of at least 1 ps. However, for the simulation in chapter 4, which is consisted of the bulk Co_3O_4 spinel, a time step of 2 ps is employed as an exception. For all other systems investigated in this work, which involve hydrogen atoms, a time step of 0.5 fs is used.

Trajectories obtained from the AIMD simulations are utilized to compute various properties, such as radial distribution function, angle distribution, velocity autocorrelation function, and more. The pre-equilibrium portion of the trajectories is excluded from the analysis.

4 Structure and Dynamics of Bulk Co_3O_4 Spinel

4.1 Overview

This chapter focuses on examining the properties of the bulk Co_3O_4 spinel, including the density of states. Specifically, the dynamics of the lattice parameter at room temperature, its evolving electronic structure, and the Hirshfeld and Mulliken population analyses are presented. The primary objective is to demonstrate the stability of these critical parameters throughout the simulation.

4.2 Density of States

The initial step involves performing a geometry optimization or energy minimization calculation to obtain a relaxed structure of the bulk Co_3O_4. The projected density of states (PDOS) for this configuration can then be determined by projecting the Kohn-Sham states onto atomic orbitals centered on the oxygen and cobalt ions (Figure 8). The PDOS provides valuable information about orbital occupations. Additionally, the oxidation states and spin states can be approximated using this information, allowing for qualitative comparisons with experimental observations to validate the electronic structure calculation.

Figure 8 illustrates that the total valence bandwidth of the bulk Co_3O_4 is approximately 8.3 eV. The lower energy level valence band is predominantly composed of O^{2-} states, with a maximum peak at around – 4.7 eV. Conversely, the upper valence band, particularly near the valence band edge, mainly originates from the Co^{3+} d states. The lower portion of the conduction band is primarily influenced by the Co^{3+} d states, with some contribution from Co^{2+} d states and a minor contribution from O^{2-} states.

These observations align with previous theoretical calculations by Chen et al.[21] and Creazzo et al.,[25] both utilizing the PBE+U scheme, as well as an experimental report by Langell et al.[66] The calculated band gap of approximately 1.6 eV is consistent with an independent calculation performed by subtracting the highest occupied molecular orbital (HOMO) from the lowest unoccupied molecular orbital (LUMO) using the CP2K/Quickstep package.[65]

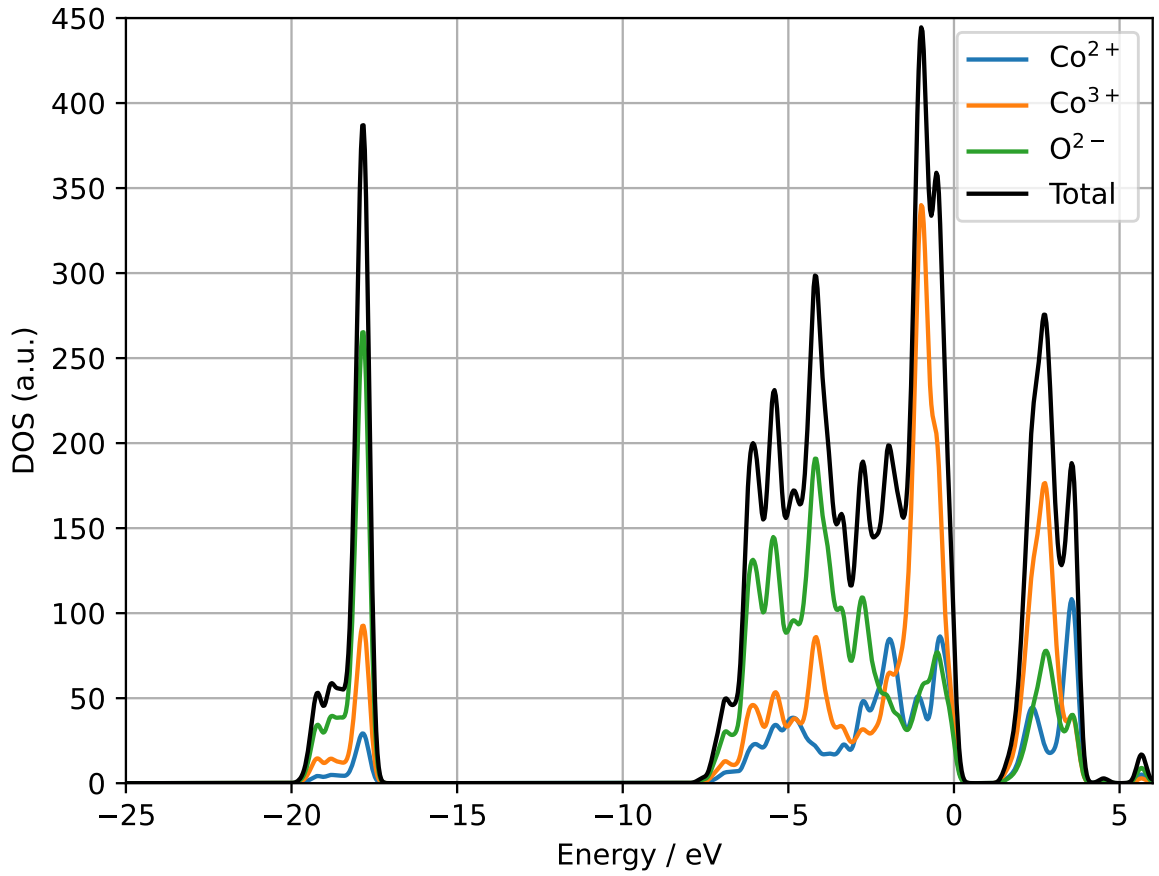

Figure 8: Projected Density of States (PDOS) of the optimized Co_3O_4 spinel.

4.3 AIMD Simulation of the Bulk Co_3O_4 Spinel

The geometry-optimized sample obtained from the previous section serves as the initial configuration for an ab initio molecular dynamics (AIMD) simulation, which is run for a total of 72 ps (Figure 9 (a)). In Figure 9 (b), the AIMD simulation trajectory lines are displayed for Co^{2+} ions (green), Co^{3+} ions (pink), and O^{2-} ions (red) during the 72 ps AIMD simulation run. The ions primarily exhibit fluctuations around their initial positions throughout the simulation. Finally, Figure 9 (c) presents the final configuration of the AIMD simulation.

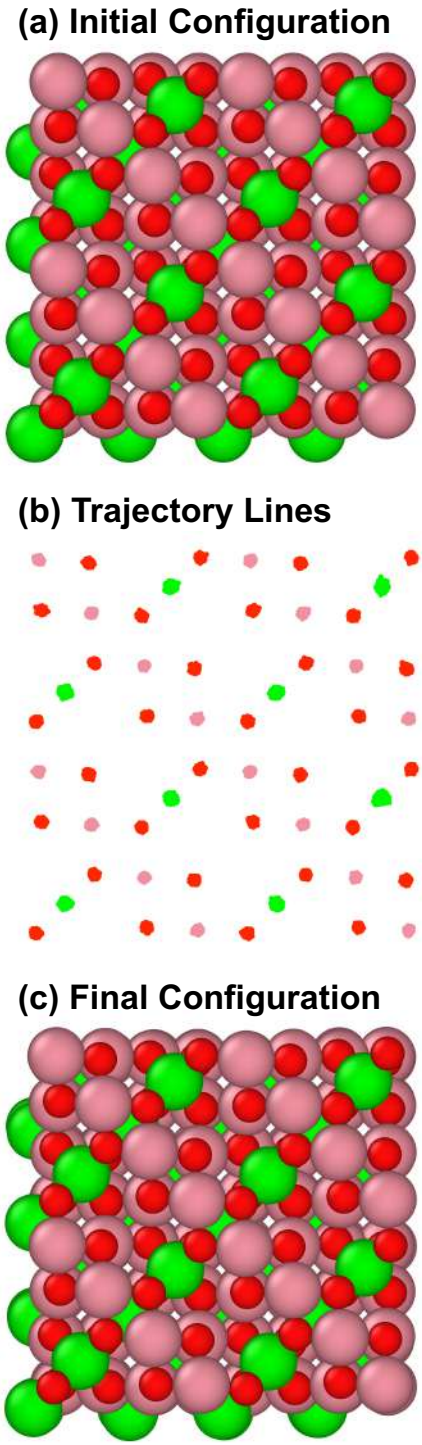

Figure 9: (a) Initial configuration (top view) of the bulk Co_3O_4 spinel, (b) trajectory lines of Co^{2+} (green), Co^{3+} (pink), and O^{2-} (red) during the 72 ps AIMD simulation, and (c) Final configuration (top view).

4.4 Lattice Parameter

Figure 10 illustrates the evolution of the lattice parameter for the bulk Co_3O_4 during the 72 ps AIMD simulation at room temperature. The plot includes 36000 data points

represented by light blue points, along with a smoothed representation obtained using a Savitzky–Golay filter, shown as the dark blue line. As observed in the figure, the equilibrated Co_3O_4 lattice parameter exhibits fluctuations around 8.13 Å. This demonstrates the stability of the lattice parameter throughout the entire 72 ps simulation, indicating no significant drift occurring.

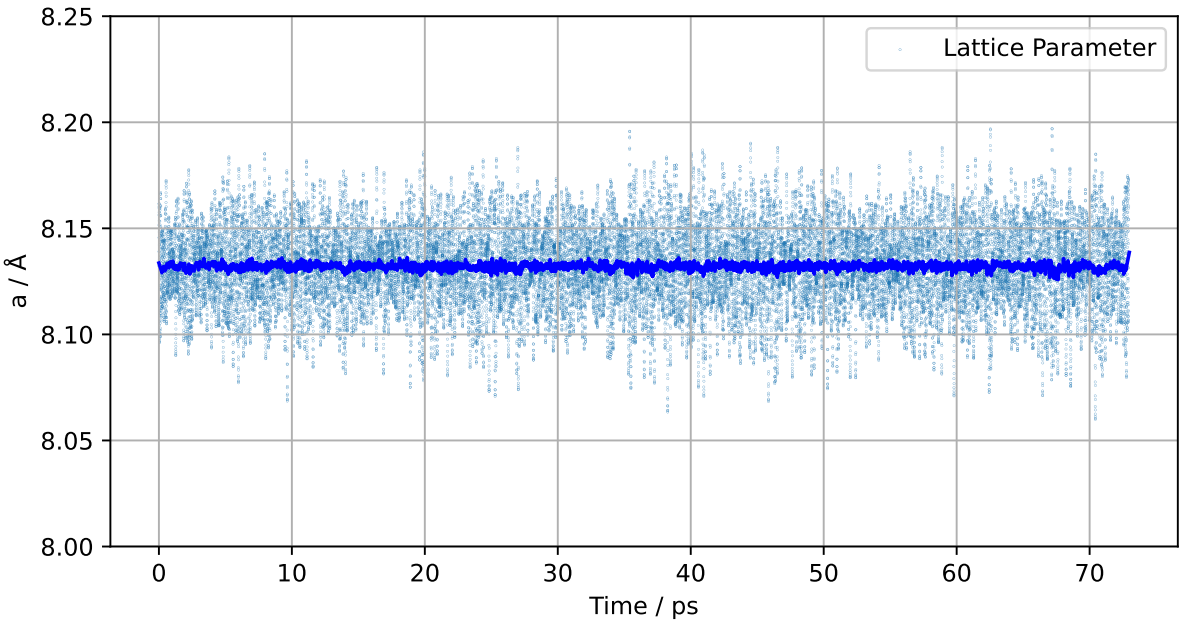

Figure 10: The evolution of the bulk Co_3O_4 lattice parameter during the 72 ps AIMD simulation.

4.5 Mulliken and Hirshfeld Population Analysis

Both Mulliken population analysis (MPA)[72] and Hirshfeld population analysis (HPA)[50] are approximate methods used to calculate the partial charges of ions within a molecule. However, they differ in their underlying principles and the way they partition the electron density. These analyses rely on various factors such as the choice of basis set, functional, material or molecule under study. The impact of such parameters on different types of population analysis has been studied in detail by Choudhuri and Truhlar.[22] In this work, the absolute values obtained from these population analyses will not be used to draw conclusions. Instead, the focus will be on observing how the relative charge changes over time, particularly during an oxidation reaction.

Figure 11 displays the evolution of Mulliken charges during the 72 ps AIMD simulation. The Mulliken charges for Co^{2+} (blue), Co^{3+} (green), and O^{2-} (purple) fluctuate around 0.75 e, 0.59 e, and – 0.48 e, respectively. Similarly, Figure 12 illustrates the fluctuation of Hirshfeld charge values for Co^{2+} (blue), Co^{3+} (green), and O^{2-} (purple) around – 0.77 e, – 1.35 e, and 0.80 e, respectively. The key observation is that these charges remain *stable* during the 72 ps of the AIMD simulation.

While the charges of all Co^{2+}, Co^{3+}, and O^{2-} ions within the bulk Co_3O_4 spinel fluctuate around similar values, for simplicity, only one ion of each type is randomly chosen from the bulk sample in Figure 11 and Figure 12.

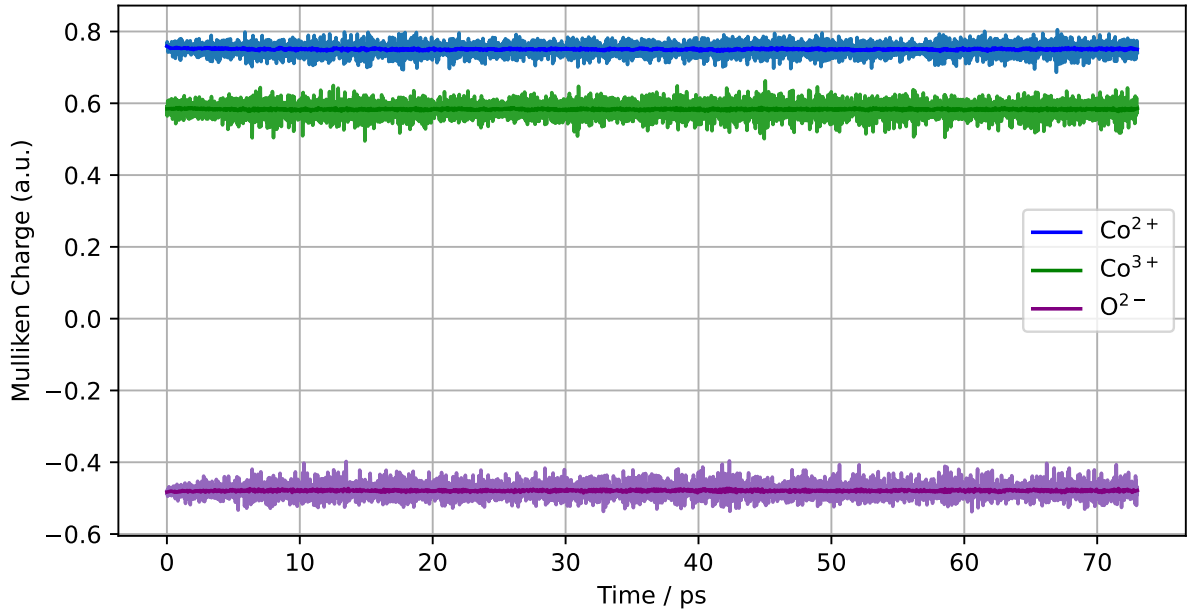

Figure 11: Evolution of Mulliken charges of Co^{2+} (blue), Co^{3+} (green), and O^{2-} (purple) during the 72 ps AIMD simulation.

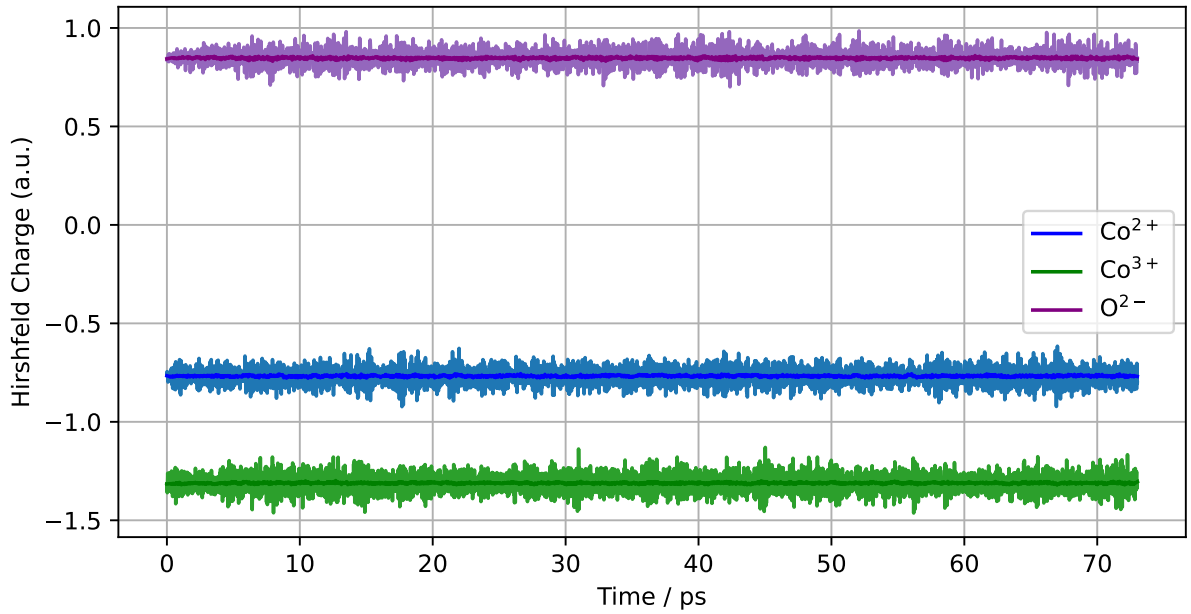

Figure 12: Evolution of Hirshfeld charges of Co^{2+} (blue), Co^{3+} (green), and O^{2-} (purple) during the 72 ps AIMD simulation.

5 Structure, Dynamics and Reactivity of Co_3O_4 / 2-propanol Interface

Note: some parts of this chapter have been previously published in the Journal of Chemical Physics under the title "2-Propanol Interacting with Co_3O_4 (001): A Combined vSFS and AIMD Study".[80]

5.1 Overview

The interaction of 2-propanol with various Co_3O_4 surfaces is investigated through simulations conducted under different conditions. The reference system chosen is the B-terminated Co_3O_4 (001) surface, based on our previous work[79] and an experimental report by Falk et al.,[32] which demonstrates the favorability of such surface termination for 2-propanol oxidation. In addition, it has been also previously shown that the B-terminated (001) surface is thermodynamically more stable over the entire range of oxygen chemical potentials.[47] The impacts of surface hydroxylation, elevated temperature, and a comparison with the A-terminated Co_3O_4 (001) surface are also discussed. The interaction of the B-terminated (111) and (110) surfaces with 2-propanol is also studied and compared with that of the (001) surface.

It is found that 2-propanol is molecularly adsorbed on the (001) surfaces, although minor dissociation is also observed. The presence of a hydroxylated surface hinders such minor dissociation. Moreover, higher temperatures decrease the interactions between the adsorbate species and the surface, thereby preventing dissociation. Conversely, on the A-terminated (001) surface, more dissociation is observed, indicating its superior activity for 2-propanol dissociation, which is consistent with previous computational experiments[64] for the Co_3O_4 (001)/water interface. Details regarding 2-propanol adsorption, including adsorption geometry and partial charge transfers, are also discussed.

On the B-terminated (111) surface, complete dissociation of all 2-propanol molecules at the interface is observed, contrasting the behavior observed on the (001) surface. A Mars-van Krevelen-type mechanism is also observed on the (111) surface. Similarly, the B-terminated (110) surface exhibits high activity for 2-propanol dissociation, particularly at higher temperatures, which can be attributed to the presence of two-fold coordinatively unsaturated oxygen on the surface. When comparing these three surfaces, (001), (111), and (110), it is found that both (111) and (110) surfaces are more favorable for 2-propanol activation (dissociation) than the (001) surface. The surface reconstructions occurring between these three surfaces are also investigated.

Recently, researchers reported the spectra of 2-propanol on Co_3O_4-based spinel using diffuse reflectance infrared Fourier transform spectroscopy techniques (DRIFTS).[29] However, attributing various peaks to their corresponding vibrational modes is known

to be a non-trivial task, requiring explanations from theoretical frameworks. Therefore, power spectra of the above systems (which closely resemble the experimental systems) are calculated using velocity time autocorrelation functions of the AIMD trajectories. The advantage of obtaining such spectra from computer simulations lies in the ability to include or exclude specific modes, enabling a more accurate attribution of each peak in the spectra.

5.2 Co_3O_4 (001) / 2-propanol Interaction

5.2.1 B-terminated (001) Pristine Surface (Reference System)

An AIMD simulation is performed for a system consisting of the B-terminated pristine surface at 300 K. The snapshots from the last configuration, obtained after a 20 ps run, are shown in Figure 13. Throughout the simulation, six out of eight 2-propanol molecules molecularly adsorb on the Co^{3+} sites of the surface. No adsorption on the Co^{2+} sites is observed. After 5 ps, one of the 2-propanol molecules dissociates, as depicted in Figure 15. The transfer of the proton to the surface lattice oxygen can be observed in Figure 13, denoted by a black circle. The dissociated 2-propanol is shown by a yellow circle. Additionally, one of the 2-propanol molecules is also mobile in the contact layer, temporarily adsorbing on different adsorption sites. The observation of dominant molecular adsorptions is in agreement with vibrational sum frequency generation spectroscopy experiment.[80] No partial oxidation of 2-propanol, and consequently, the formation of acetone, is observed. This lack of observation of acetone formation is also consistent with the aforementioned experiment.

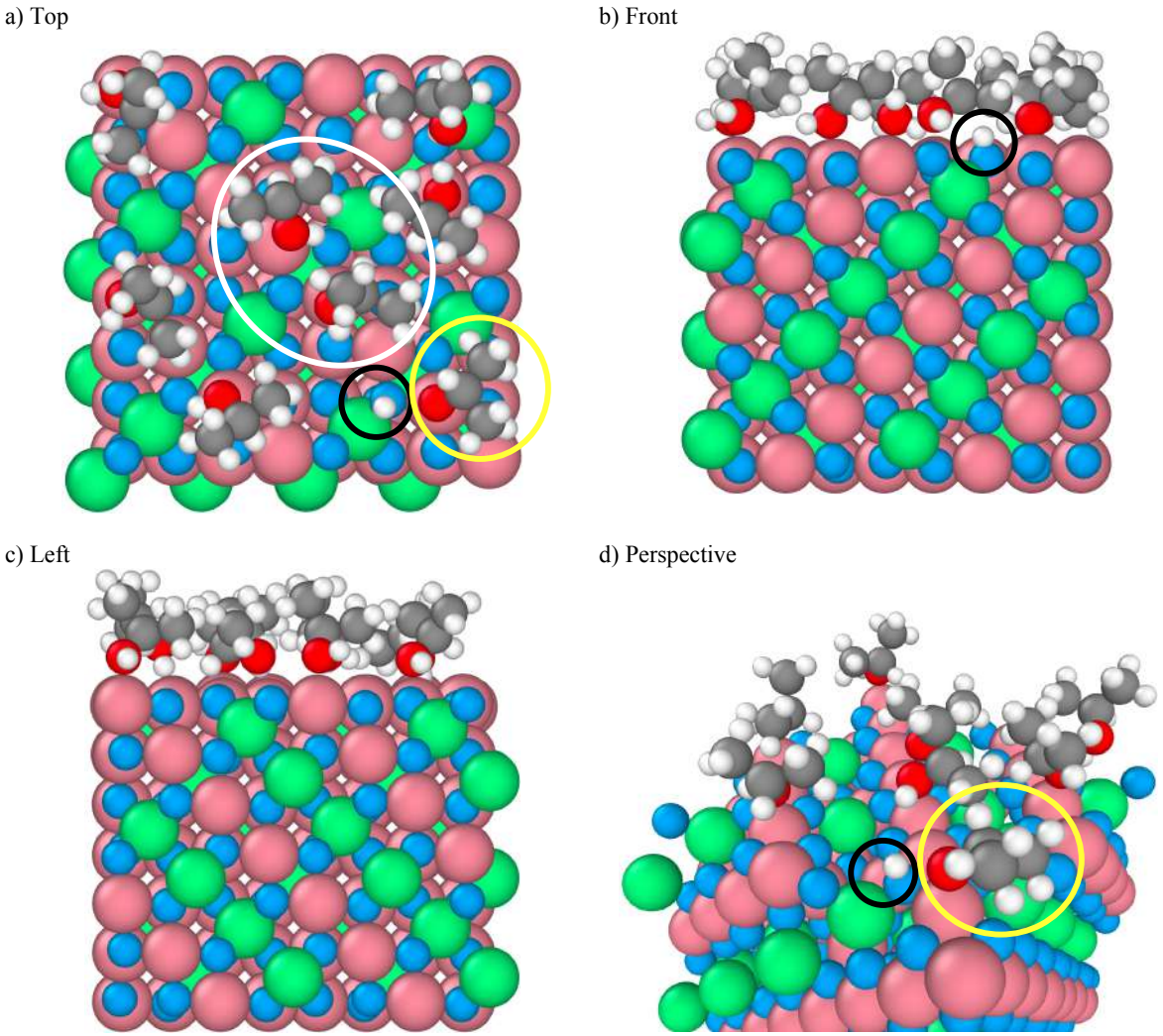

Figure 13: Snapshots of the final configuration of the AIMD simulation (top, front, left and perspective views) for 2-propanol adsorption on the B-terminated pristine Co_3O_4 (001) surface at 300 K. Co^{3+} (pink), Co^{2+} (green), O in Co_3O_4 (blue), O in 2-propanol (red), C (gray) and H (white). A single proton transfer to the surface lattice oxygen can be observed (highlighted in black circle). The dissociated 2-propanol is denoted in yellow circle.

Molecular Adsorption

The Figure 14 presents the time evolution of the O–H, C–H, C–O, and Co^{3+}–O distances for a molecularly adsorbed 2-propanol molecule during a 20 ps AIMD simulation. Similar behavior is observed for six out of the other seven 2-propanol molecules. The figure shows that all the mentioned bonds exhibit fluctuations around their initial distances throughout the simulation. Notably, the Co^{3+}–O bond shows the highest fluctuation, while the O–H and C–H bonds exhibit the lowest fluctuations, which is expected due to their relatively shorter lengths. Interestingly, in the evolution of the O–H bond, peaks can be observed at approximately 3.5 ps, 8 ps, and 19 ps, which correspond to failed attempts of proton transfer or exchange between 2-propanol and lattice oxygen.

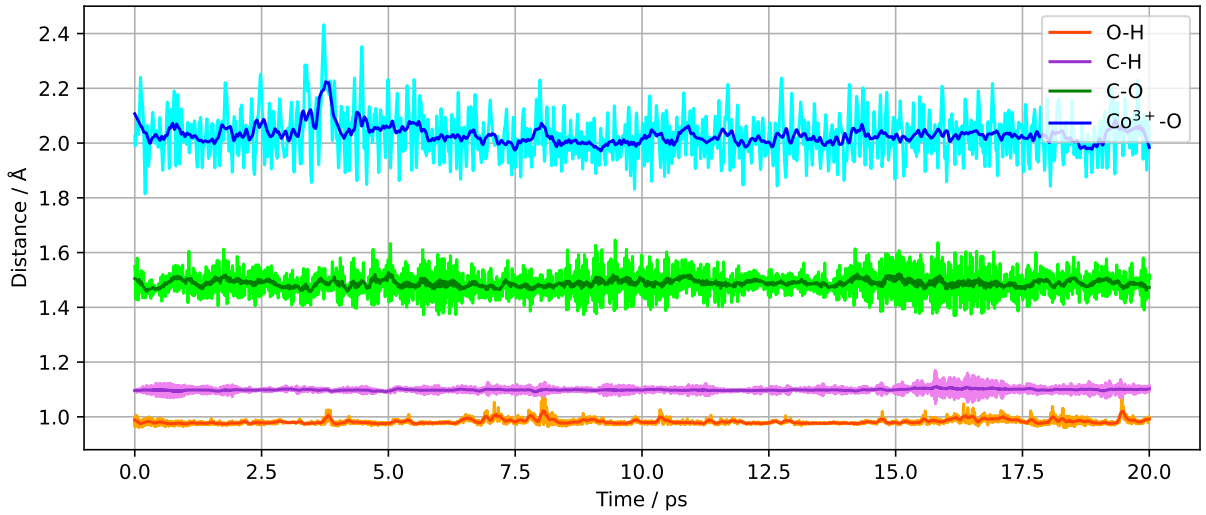

Figure 14: Evolution of O–H, C–H, C–O and Co^{3+}–O distances for a molecularly adsorbed 2-propanol molecule.

Dissociative Adsorption

Figure 15 illustrates the evolution of the O–H, C–H, C–O, and Co^{3+}–O distances for a dissociatively adsorbed 2-propanol molecule during the 20 ps AIMD simulation. As depicted in the figure, the cleavage of the O–H bond (orange) occurs after approximately 5 ps of simulation, leading to a shortening of the Co^{3+}–O distance (blue). Additionally, a slight shortening of the C–O bond (green) can also be observed. The C–H bond remains relatively unchanged throughout the simulation, indicating the absence of dehydrogenation (C–H bond cleavage).

The failed attempt for O–H bond cleavage observed during the early 5 ps is also present, similar to the case of molecular adsorption (Figure 14). One would expect that after 5 ps, when one proton is transferred to the surface, the surface would become more stable and less active, resulting in increased stability of the O–H bond in other 2-propanol molecules. However, Figure 14 shows the opposite, indicating an increase in O–H fluctuation after 5 ps of simulation time. One possible explanation is based on the formation of a 2-propoxide molecule, which promotes proton exchange between 2-propanol and 2-propoxide molecules. Another explanation could be attributed to the dynamic nature of 2-propanol and the varying orientations they adopt at different stages of the simulation. Therefore, in this case, it can be concluded that the orientation of 2-propanol in the later stages of the simulation brings the O–H vector closer to a lattice oxygen.

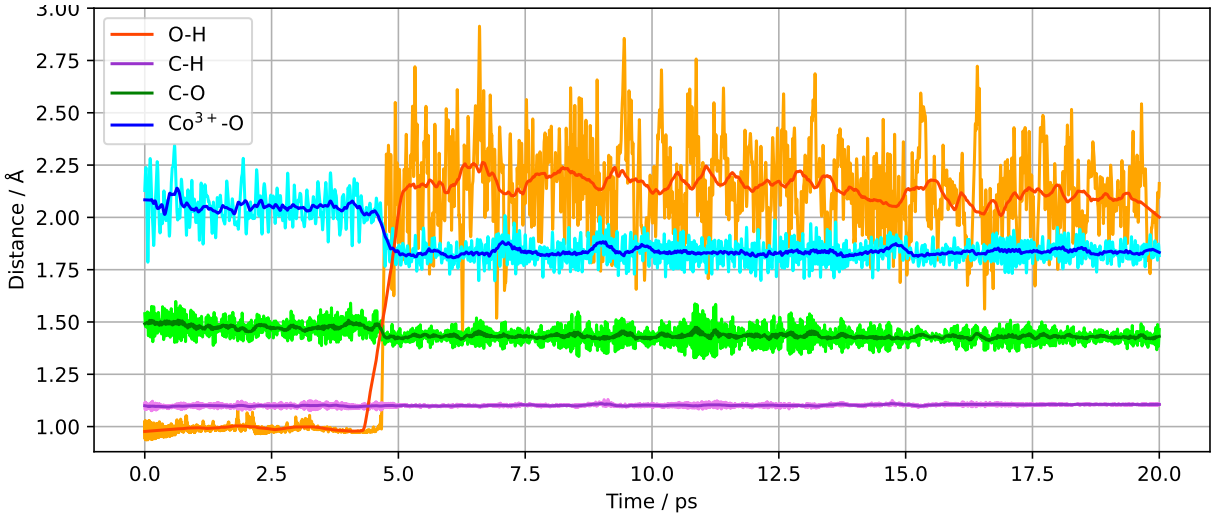

Figure 15: Evolution of O–H, C–H, C–O and Co^{3+}–O distances for a dissociatively adsorbed 2-propanol molecule.

5.2.2 Population Analysis: Hirshfeld, Mulliken, and Bader Charges

Charge Density Difference

Figure 16 illustrates the charge density difference (CDD) plot obtained from the last step of the AIMD simulation of the system depicted in Figure 13. This system consists of the B-terminated pristine Co_3O_4 (001) surface at 300 K, featuring both molecularly and dissociatively adsorbed 2-propanol. The CDD is computed by subtracting the electron density contributions of the pure substrate and the adsorbates from the total system electron density. The plot highlights yellow regions representing electron density accumulation and cyan regions denoting electron density depletion. From this CDD plot, several insight can be drawn:

- The bonding between the adsorbate and Co^{3+}, emphasized by orange rectangles and predominantly characterized by yellow regions, indicates a transfer of electron density towards $O_{2\text{-propanol}}$–Co^{3+} bonds upon adsorption.
- The regions surrounding $O_{2\text{-propanol}}$, depicted by red ellipses and primarily exhibiting cyan color, signify a loss of electron density upon adsorption.
- The cyan regions surrounding the hydrogen atoms of the CH_3 groups, marked by black rectangles and oriented towards the surface, indicate a depletion of electron density in these regions.
- The topmost Co^{2+} sites, highlighted by black circles, although coordinatively saturated and not directly involved in 2-propanol adsorption, exhibit electronic involvement in the adsorption process.

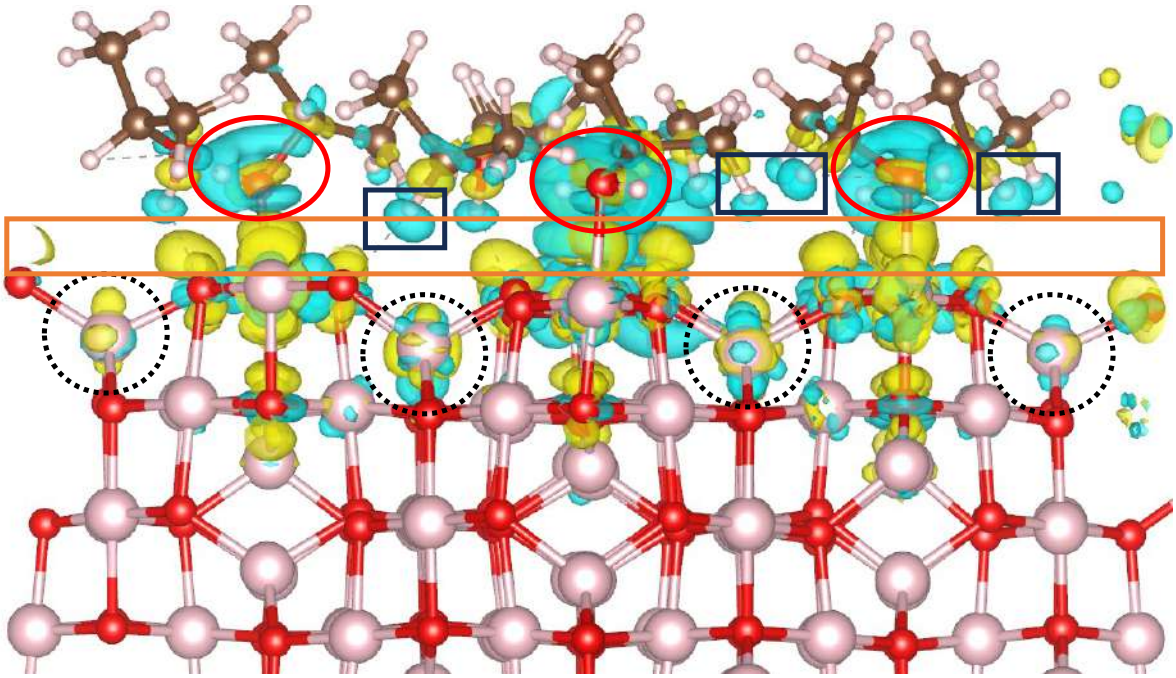

Figure 16: Charge density difference plot for the adsorption of 2-propanol on Co^{3+} sites of the B-terminated Co_3O_4 (001) surface at 300 K. The iso-surfaces are drawn at density levels of – 0.003 (cyan) and + 0.003 (yellow) e $Å^{-3}$. The yellow regions indicate the accumulation of electron density, while the cyan regions indicate the depletion of electron density.

While CDD plots provide qualitative insight into charge distribution during adsorption, the inclusion of additional population analysis methods such as Hirshfeld population analysis (HPA) and Mulliken population analysis (MPA) can offer a complementary understanding of charge evolution. In the following sections, the application of these methods to investigate charge dynamics during both molecular and dissociative adsorption processes are demonstrated.

Molecular Adsorption

Figure 17 illustrates the evolution of Hirshfeld and Mulliken atomic charges for various atoms during the molecular adsorption of a 2-propanol molecule. The atoms considered are O (orange), the central carbon atom C2 (violet), the hydroxyl hydrogen (green), and the hydrogen in C2–H (blue). As mentioned in the previous chapter, the relative changes in population analysis are of significance, rather than their absolute values.

In both Hirshfeld charges (Figure 17 (a)) and Mulliken charges (Figure 17 (b)), the majority of the charges remain relatively stable compared to their initial values, except for the final few picoseconds of the simulation. Notably, the oxygen atom displays the highest fluctuations in both Hirshfeld and Mulliken charges due to the more dynamic nature of the Co^{3+}–O bond. However, in the last picoseconds of the simulation, a temporary drop in the oxygen's charge (in both Hirshfeld and Mulliken analysis) is observed, followed by

a recovery to its original value in the final steps. The hydroxyl hydrogen also experiences a small decrease in its charges, particularly noticeable in MPA. This behavior can be attributed to the presence of another 2-propanol molecule in proximity, which has changed its adsorption site, thus stimulating proton exchange between the two. These two 2-propanol molecules are indicated by a white ellipse in Figure 15.

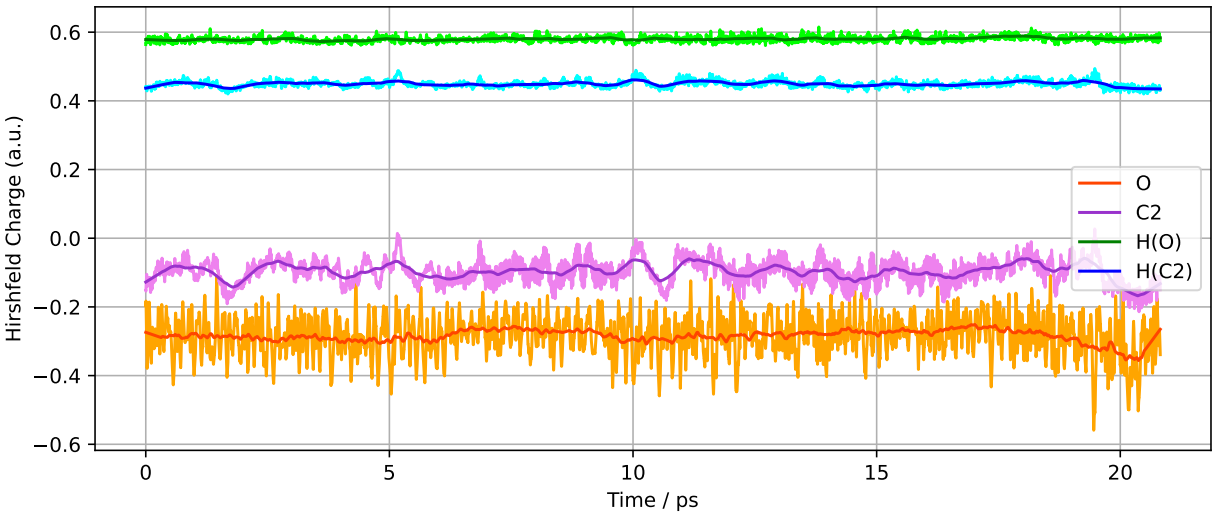

(a)

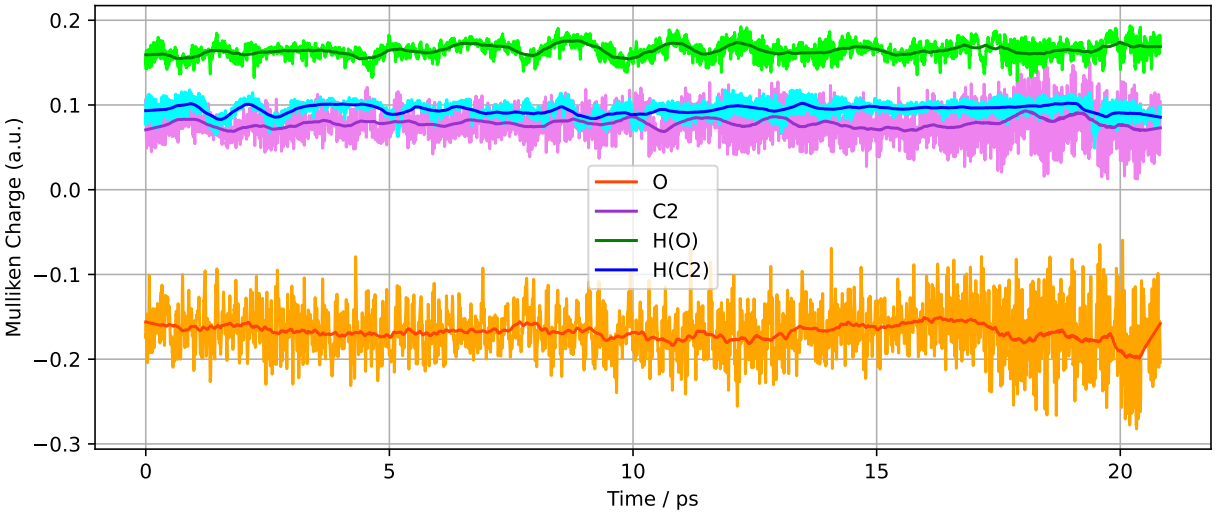

(b)

Figure 17: Evolution of Hirshfeld (a) and Mulliken (b) atomic charges of O (orange), C2 (violet), hydroxyl hydrogen (green) and hydrogen in C2–H (blue) during the molecular adsorption of a 2-propanol molecule.

Dissociative Adsorption

During dissociation, a significant shift in atomic charges occurs. Figure 18 depicts the evolution of Hirshfeld and Mulliken atomic charges during the dissociative adsorption of a 2-propanol molecule. Approximately 4 ps after the initiation of dissociation, there is a noticeable change in the charge of oxygen (orange) in both HPA and MPA. However, the behavior differs between HPA and MPA: in HPA, the oxygen charge increases towards

more positive values, while in MPA, it decreases to a lower value. Intuitively, MPA is more consistent, as one would expect that after the dissociation of 2-propanol (specifically, the abstraction of the hydroxyl hydrogen), oxygen would possess more electron density.

The charge of the C2 atom (violet) initially drops within the first picosecond of the simulation before stabilizing for a few picoseconds. This initial 1 ps can be disregarded since the system is in the equilibration phase during that time. After dissociation, the C2 charge gradually increases (more noticeably in HPA) until 15 ps of the simulation. At 15 ps, a sudden shift in the Hirshfeld charge of C2 is observed, whereas the MPA shows a more gradual transition. Additionally, the charge of the hydrogen atom in the CH group (blue) also decreases at 15 ps of the simulation.

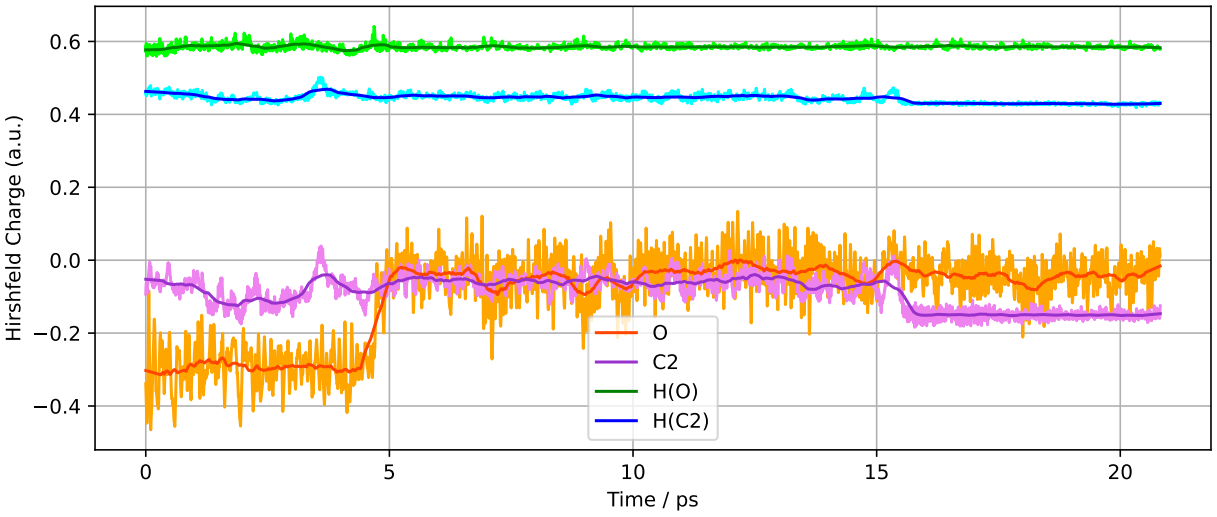

(a)

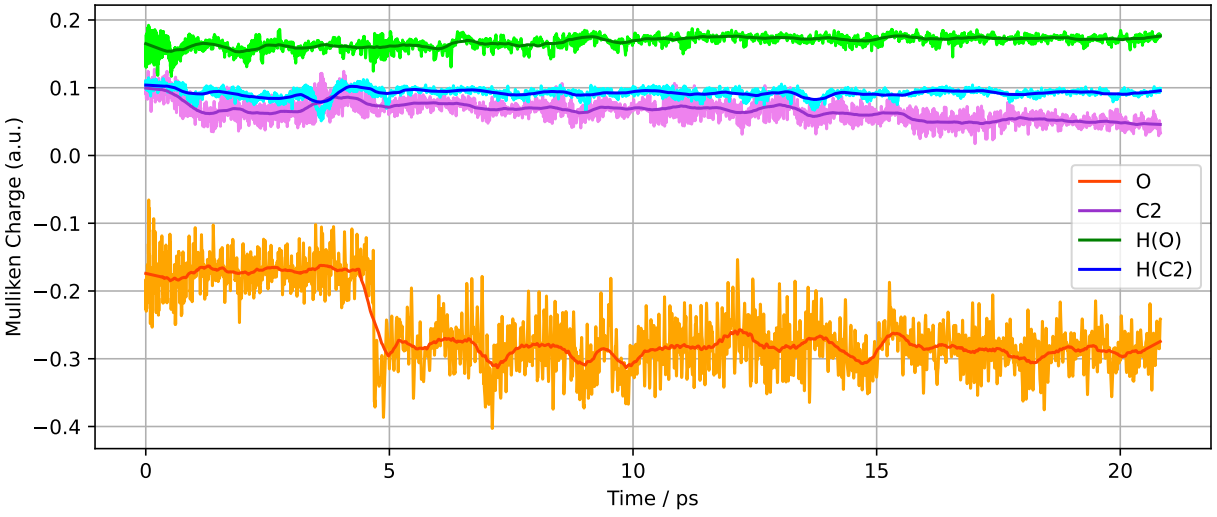

(b)

Figure 18: Evolution of Hirshfeld (a) and Mulliken (b) atomic charges of O (orange), C2 (violet), hydroxyl hydrogen (green) and hydrogen in C2–H (blue) during the dissociative adsorption of a 2-propanol molecule.

The orientation of the 2-propanol/2-propoxide molecule is depicted in Figure 19 at

three stages of the simulation. The hydrogen in the CH group is highlighted in yellow for emphasis. Figure 19 (a) represents the orientation of 2-propanol before dissociation, (b) represents the orientation of the resulting 2-propoxide, while Figure 19 (c) shows the orientation of 2-propoxide after 15 ps. Notably, the CH vector points towards the surface in (a) and (b), but it points away from the surface in (c) and maintains this orientation for the remainder of the simulation. This transition from stages (a) and (b) to stage (c), leading to the orientational change, explains the observed electronic charge shifts in the C2 atom and the hydrogen of the CH group. These two types of orientations represent the only scenarios observed throughout this study.

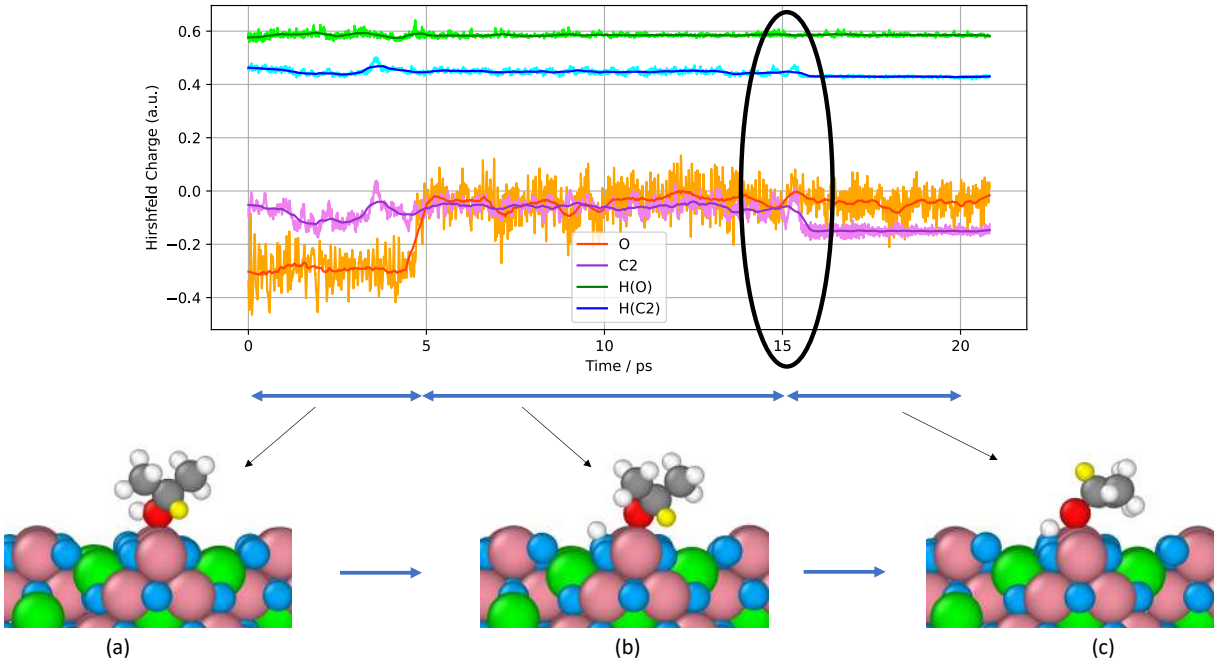

Figure 19: Illustration of the orientation of the 2-propanol/2-propoxide molecule at different stages of the simulation. The CH group's hydrogen is highlighted in yellow. In (a) and (b), representing the orientation before dissociation, the CH vector points towards the surface. In (c), the orientation of 2-propoxide after 15 ps, the CH vector points away from the surface and remains in that configuration for the rest of the simulation. This transition from (a) and (b) to (c) corresponds to the observed electronic charge shifts in the C2 atom and the hydrogen of the CH group.

5.2.3 B-terminated (001) Hydroxylated Surface

In realistic experimental conditions, the presence of a small amount of water at ambient conditions is inevitable.[80] As a result, the surface undergoes hydroxylation. In this study, the hydroxylated system is prepared by exposing the system to liquid water and equilibrating it at room temperature. During this process, water dissociation occurs, and protons transfer to the surface lattice oxygen. Subsequently, the excess H_2O/OH^- species are removed from the system, and eight 2-propanol molecules are introduced.

On the B-terminated (001) surface, as observed in previous research,[64] the degree of hydroxylation can vary from one to five surface OH groups, depending on factors such as water pressure. Figure 20 depicts the final snapshots of the AIMD simulation for the hydroxylated surface, illustrating that no dissociation of 2-propanol occurs, unlike on the pristine surface discussed previously. The black circle in Figure 20 represents the single pre-existing surface OH group resulting from the prior water dissociation.

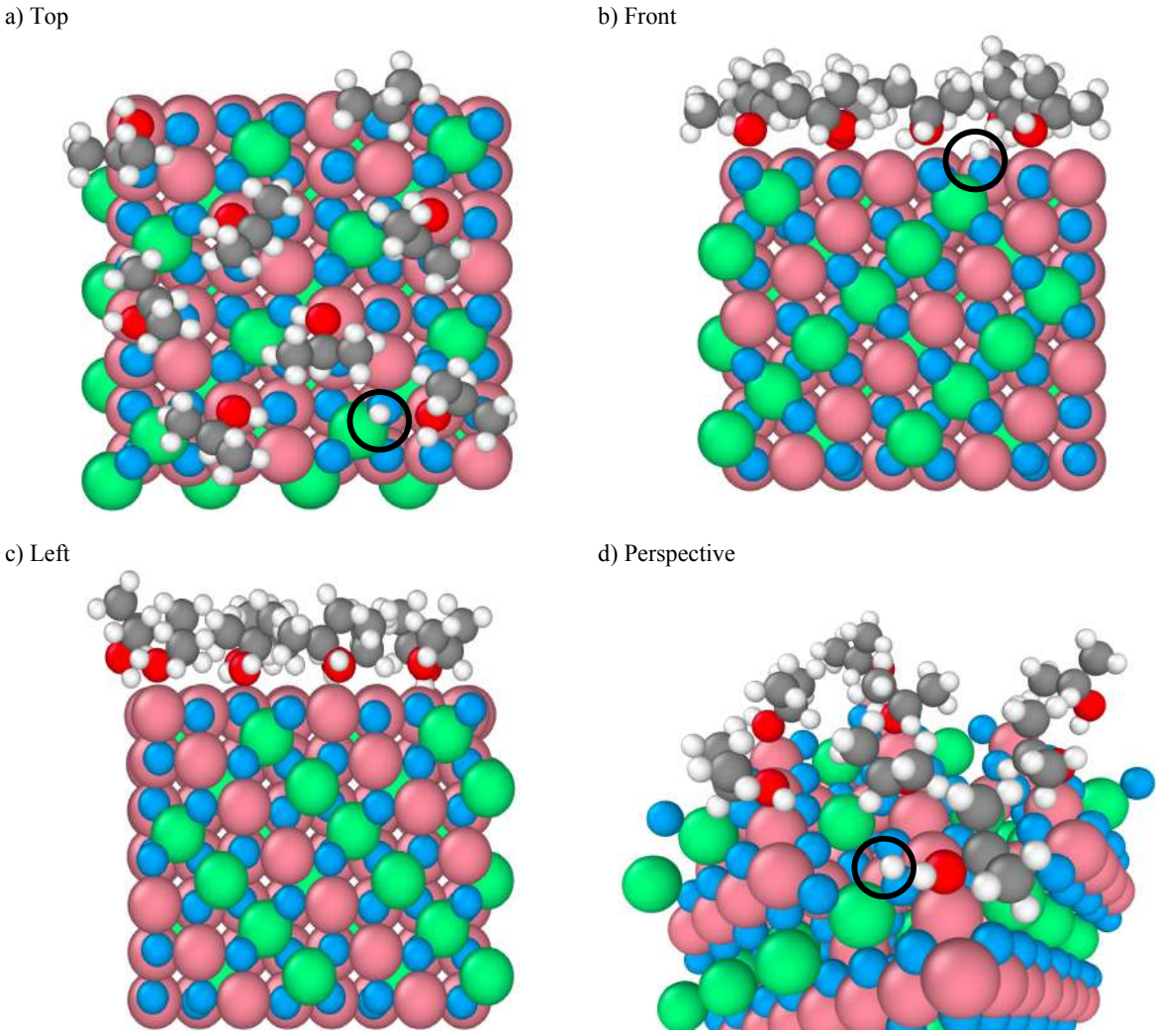

Figure 20: Snapshots of the final configuration of the AIMD simulation (top, front, left and perspective views) for 2-propanol adsorption on the B-terminated hydroxylated Co_3O_4 (001) surface at 300 K. Co^{3+} (pink), Co^{2+} (green), O in Co_3O_4 (blue), O in 2-propanol (red), C (gray) and H (white). The single surface OH group is highlighted by black circle.

O–H Bonds

Figure 21 compares the radial distribution functions (RDFs) of different pairs of atoms between a pristine surface (black dash-dotted line) and a hydroxylated surface (cyan line), both at 300 K. In Figure 21 (a), the RDF of $O_{alcohol}$ ($O_{2\text{-propanol}}/O_{2\text{-propoxide}}$) and all H atoms is shown. The peak around 1 Å corresponds to the distance between the

oxygen of 2-propanol molecules and the hydroxyl hydrogen. The peak for the pristine system is approximately 10% lower than that for the hydroxylated system, indicating the dissociation of a single 2-propanol molecule in the pristine system. The second peak around 2.1 Å represents the distance between the oxygen of 2-propanol molecules and the carbon in the CH group. The black dash-dotted line (pristine system) exhibits a slight shift towards shorter distances due to the presence of one 2-propoxide molecule in the system.

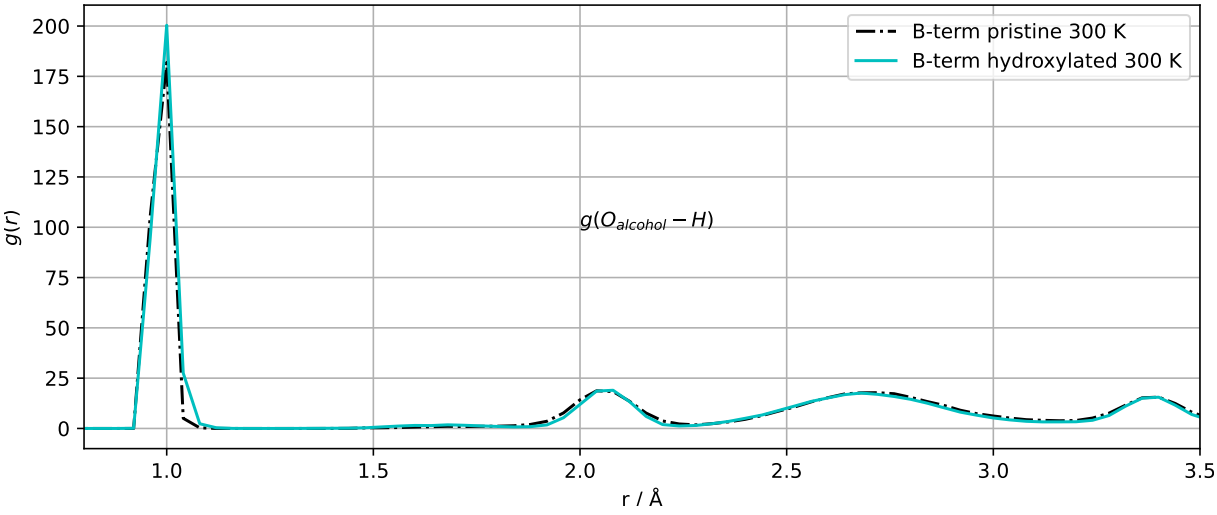

(a)

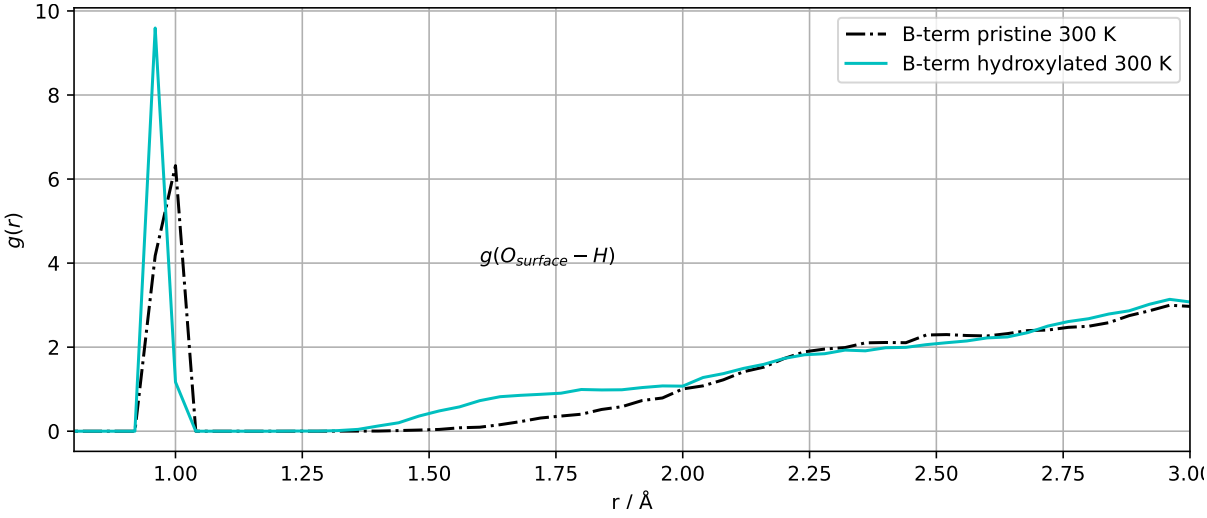

(b)

Figure 21: Radial distribution function of (a) $O_{alcohol}$ ($O_{2\text{-propanol}}$/$O_{2\text{-propoxide}}$) and all H and (b) $O_{surface}$ and all H.

Figure 21 (b) displays the radial distribution function (RDF) of surface oxygen atoms ($O_{surface}$) and all hydrogen atoms. This RDF provides information about the degree of surface hydroxylation and the probability of finding a hydroxyl hydrogen (from 2-propanol molecules) in their vicinity. Both systems exhibit a peak around 1 Å, indicating surface hydroxylation. The peak for the hydroxylated system is shifted to shorter distances,

indicating a stronger pre-existing surface OH group compared to the surface OH group resulting from 2-propanol dissociation in the pristine system. Moreover, in the region between 1.4 Å and 2 Å, the hydroxylated system shows a higher probability of finding a hydroxyl hydrogen from 2-propanol in its vicinity, suggesting a propensity for proton transfer from 2-propanol to the surface oxygen.

C–O Bond

Figure 22 illustrates the radial distribution function (RDF) of $O_{alcohol}$ and all C atoms. The first peak around 1.5 Å corresponds to the distance between $O_{alcohol}$ and the carbon of the CH group (C2), while the second peak around 2.4 Å represents the distance between $O_{alcohol}$ and the carbons of the CH_3 groups (C1 and C3). The black dash-dotted line exhibits a slight shift towards shorter distances, indicating a stronger $O_{2\text{-propoxide}}$–C2 bond compared to the $O_{2\text{-propanol}}$–C2 bond. This observation is consistent with the evolution of the C–O bond length shown in Figure 15 (green), where the C–O bond is shortened upon dissociation. The second peaks remain relatively close, indicating that the $O_{alcohol}$–C1 and $O_{alcohol}$–C3 bonds have similar average distances in both the pristine and hydroxylated systems.

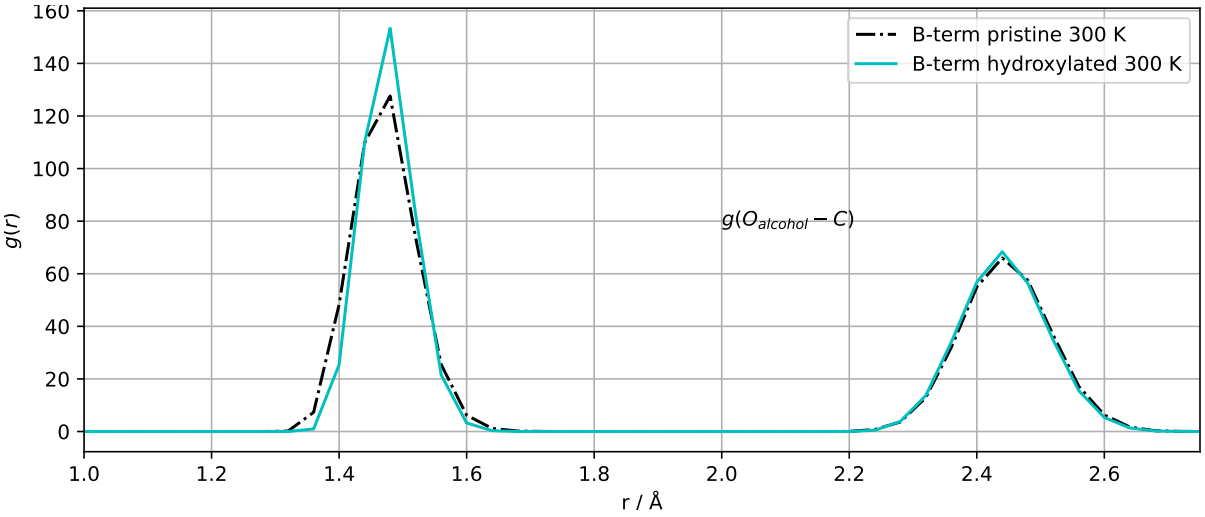

(a)

Figure 22: Radial distribution function of $O_{alcohol}$ and all C atoms.

Adsorption

Additionally, Figure 23 presents the RDF of $O_{alcohol}$ to the closest Co ion, which corresponds to the Co^{3+} adsorption site for the B-terminated (001) surfaces. In the pristine system, two closely separated peaks can be observed in this region, indicating a stronger bond between the oxygen of 2-propoxide and the Co^{3+} adsorption sites compared to other 2-propanol molecules. This observation is supported by the evolution of the Co^{3+}–O distance shown in Figure 15 (blue), where the bond is immediately shortened

upon adsorption, from 2.1 Å to 1.82 Å. Comparing the peaks for $O_{2\text{-propanol}}$–Co in the two systems reveals an average distance of 2 Å for the pristine system and 2.1 Å for the hydroxylated system, indicating a stronger Co^{3+}–$O_{2\text{-propanol}}$ bond in the pristine system.

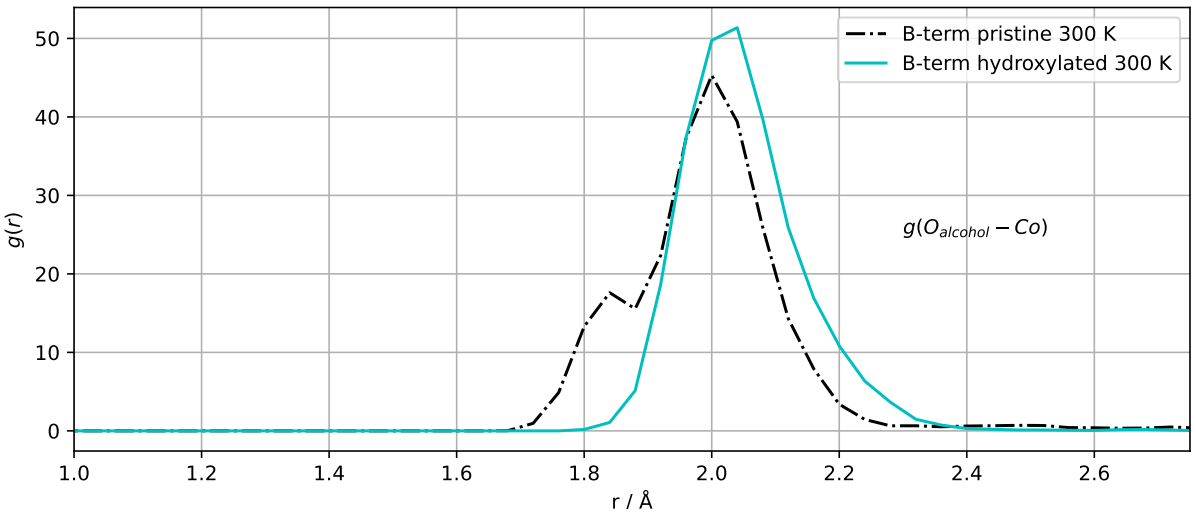

(a)

Figure 23: Radial distribution function of $O_{alcohol}$ to the closest Co ion.

Overall, the comparison between the pristine and hydroxylated systems highlights a significant difference in simulation outcomes, primarily the prevention of 2-propanol dissociation when the surface is hydroxylated. This suggests that even minor surface hydroxylation reduces surface activity by deactivating the lattice oxygen, thereby hindering 2-propanol dissociation. This finding aligns with previous studies using DFT calculations, which have investigated the impact of surface hydroxylation on surface reactivity.[102]

5.2.4 Impact of Temperature

The initial configuration of the pristine system (see Figure 13) is also utilized for AIMD simulation at 450 K to investigate the effect of elevated temperature on 2-propanol adsorption. As depicted in Figure 24, all eight 2-propanol molecules remain molecularly adsorbed on the surface without undergoing any dissociation.

O–H Bonds

Figure 25 compares the distributions of $O_{alcohol}$ and all H (a) and $O_{surface}$ and all H (b) for the pristine surface at two different temperatures: 300 K and 450 K. In particular, Figure 25 (a) shows the $O_{alcohol}$–H distribution, with the peak around 1 Å representing the distance between the oxygen of the alcohol molecules and the hydroxyl hydrogen. The peak for the 300 K system is approximately 5% lower than that for the 450 K system, attributed to the dissociation of 2-propanol in the 300 K system. The second peak around 2.1 Å represents the distance between the oxygen of alcohol molecules and the hydrogen

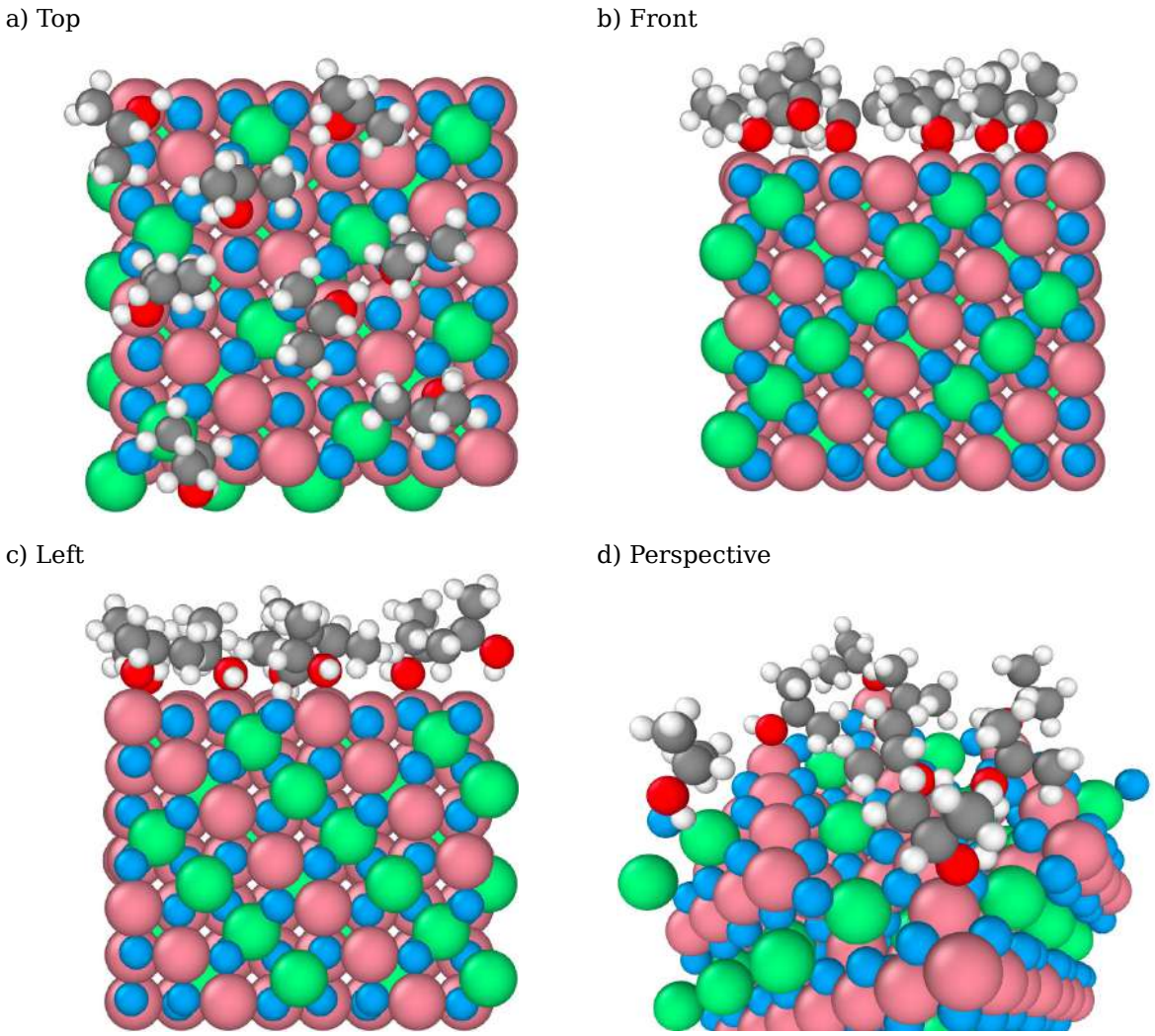

Figure 24: Snapshots of the final configuration of the AIMD simulation (top, front, left and perspective views) for 2-propanol adsorption on the B-terminated pristine Co_3O_4 (001) surface at 450 K. Co^{3+} (pink), Co^{2+} (green), O in Co_3O_4 (blue), O in 2-propanol (red), C (gray) and H (white).

of the CH group. The RDF curves for the 450 K system exhibit a slight broadening around all three peaks, which is a well-known effect of elevated temperature resulting in increased molecular mobility and a broader range of motion. Figure 25 (b) shows the RDFs of surface oxygens ($O_{surface}$) and hydrogen atoms. The notable difference between the two systems can be observed around the first peak at 1 Å, indicating surface hydroxylation in the 300 K system but not in the 450 K system.

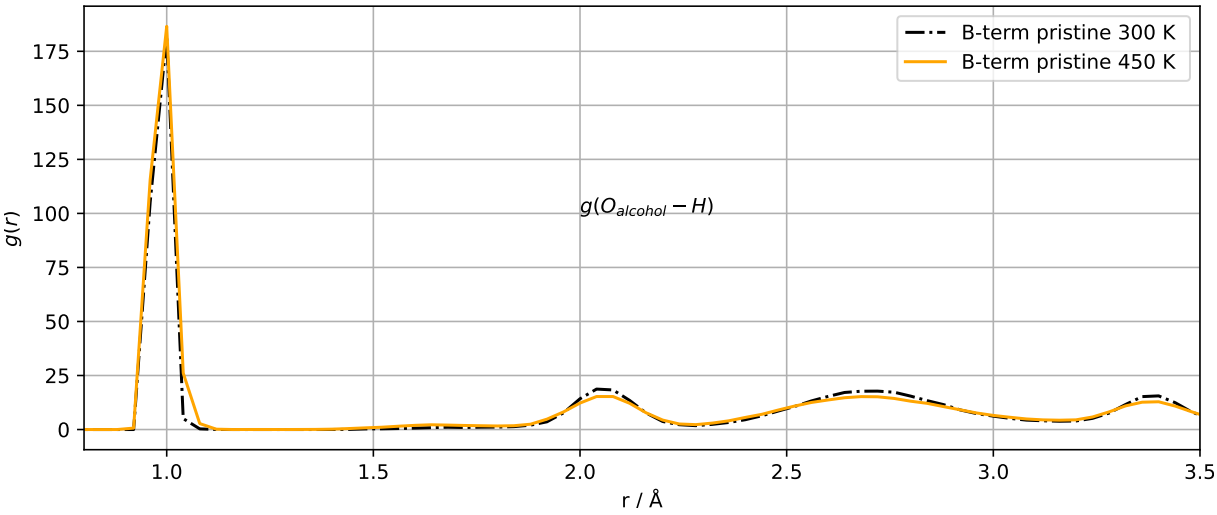

(a)

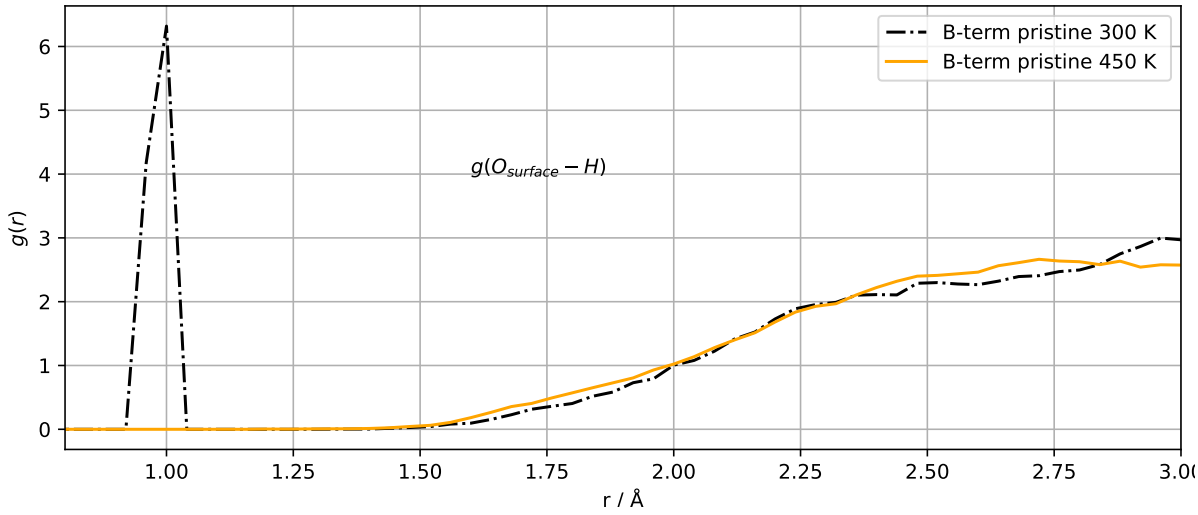

(b)

Figure 25: Radial distribution function of (a) $O_{alcohol}$ and all H and (b) $O_{surface}$ and all H.

C–O Bond

Figure 26 illustrates the RDF of $O_{alcohol}$ and all C atoms, where the first peak around 1.5 Å represents the distance between $O_{alcohol}$ and the C2 atom, and the second peak around 2.4 Å represents the distance between $O_{alcohol}$ and the C atoms in the CH_3 groups (C1 and C3). The RDF for the 450 K system exhibits a reduction of approximately 8% compared to that of the 300 K system for both peaks, along with a broadening of the distribution in both peaks due to increased fluctuations induced by the elevated temperature.

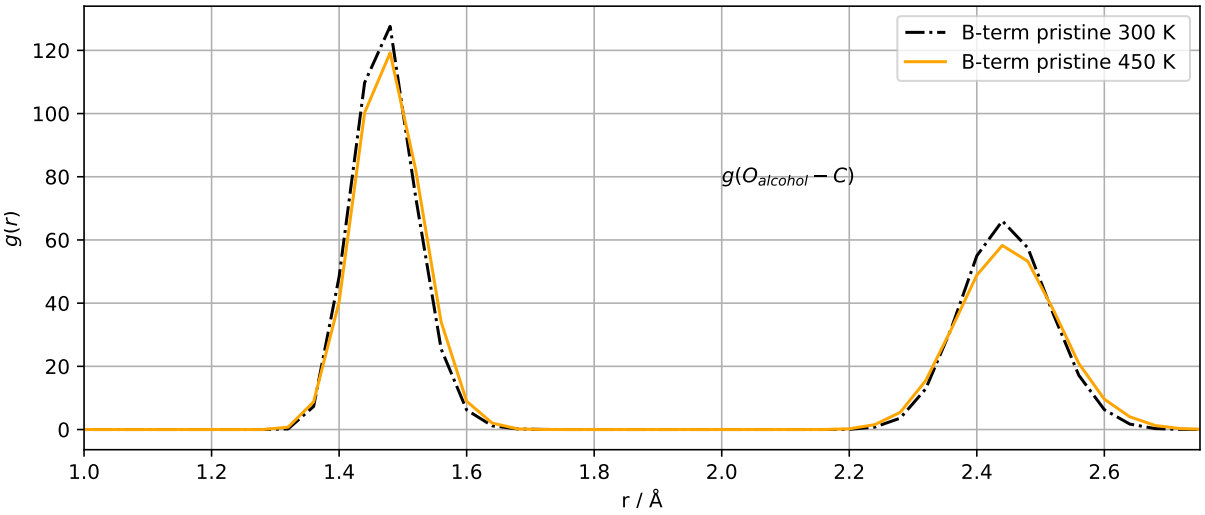

(a)

Figure 26: Radial distribution function of $O_{alcohol}$ and all C atoms.

Adsorption

The $O_{alcohol}$–Co RDF (Figure 27) reveals that the peaks around 2 Å, representing the $O_{2\text{-propanol}}$–Co^{3+} distance, are close at both temperatures. However, the peak for the 450 K system exhibits a slight broadening due to thermal effects. The RDF curve for the 300 K system demonstrates stronger bonds in both for the first peak due to 2-propoxide.

As mentioned earlier, no dissociation occurs on the pristine surface at 450 K, indicating the absence of hydroxylation. To explain this observation, trajectory lines were compared under various conditions. Figure 28 illustrates the trajectory lines of 2-propanol molecules, where only $O_{2\text{-propanol}}/O_{2\text{-propoxide}}$ are chosen to trace the trajectories to avoid complications. The middle panel of the figure shows the dynamics of the hydroxylated surface, clearly demonstrating that the adsorbed 2-propanol molecule exhibits lower mobility compared to the other systems. In contrast, the adsorbed species on the pristine surface at 450 K show the highest mobility, particularly in the vertical direction of the surface plane. This observation aligns with the findings in Figure 27, which demonstrate that at 450 K, the adsorbed species have, on average, a greater distance from the Co^{3+} adsorption sites. Thus, it can be concluded that by increasing the temperature to 450 K, the adsorbed species are expected to move further away from the Co^{3+} adsorption sites, a finding that is also supported by vSFG experimental results[80]

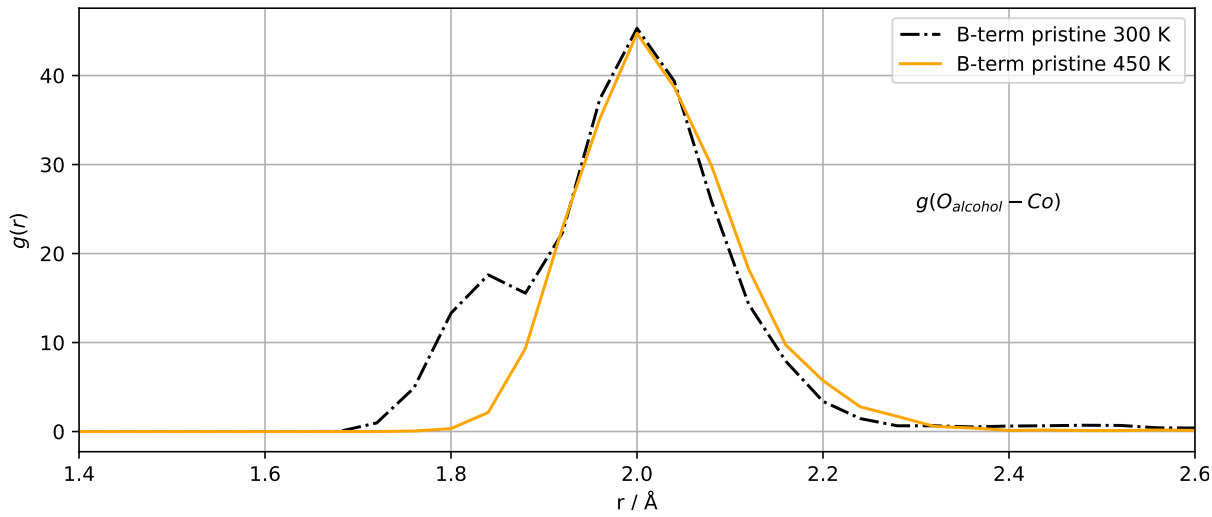

(a)

Figure 27: Radial distribution function of $O_{alcohol}$ to the closest Co ion.

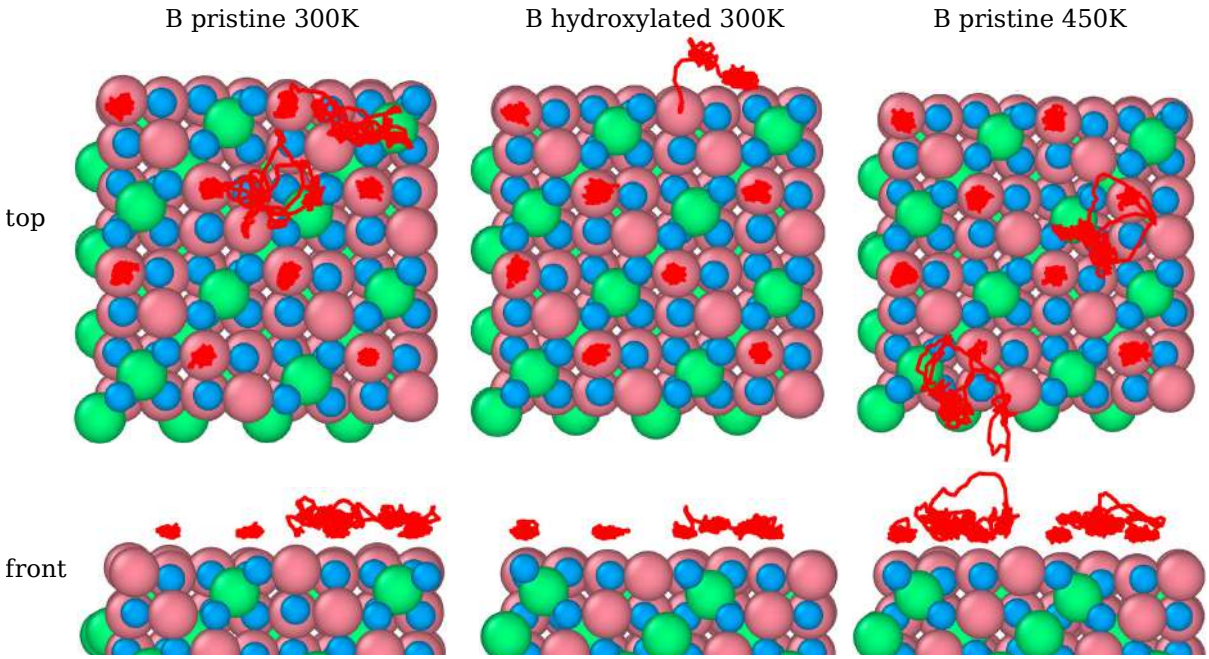

Figure 28: Trajectory lines of 2-propanol molecules ($O_{2\text{-propanol}}/O_{2\text{-propoxide}}$). Trajectory lines (red), Co^{3+} (pink), Co^{2+} (green), O in Co_3O_4 (blue), C (gray) and H (white).

Adsorption Geometry

Figure 29 illustrates the orientational distribution of the angle between the $O_{alcohol}$–H bond and the surface normal Z (001) axis (Figure 29 (b)), as well as the angle between the $O_{alcohol}$–C2 bond and the surface normal Z (001) axis (Figure 29 (c)). Although these angles are not directly accessible by the current vSFG experimental procedure, they provide valuable insights into the experiments.[80]

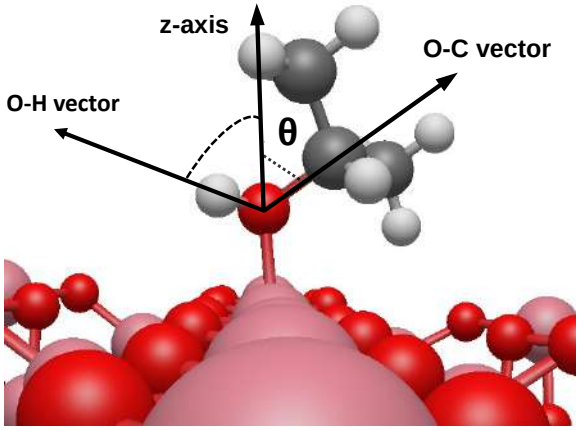

(a)

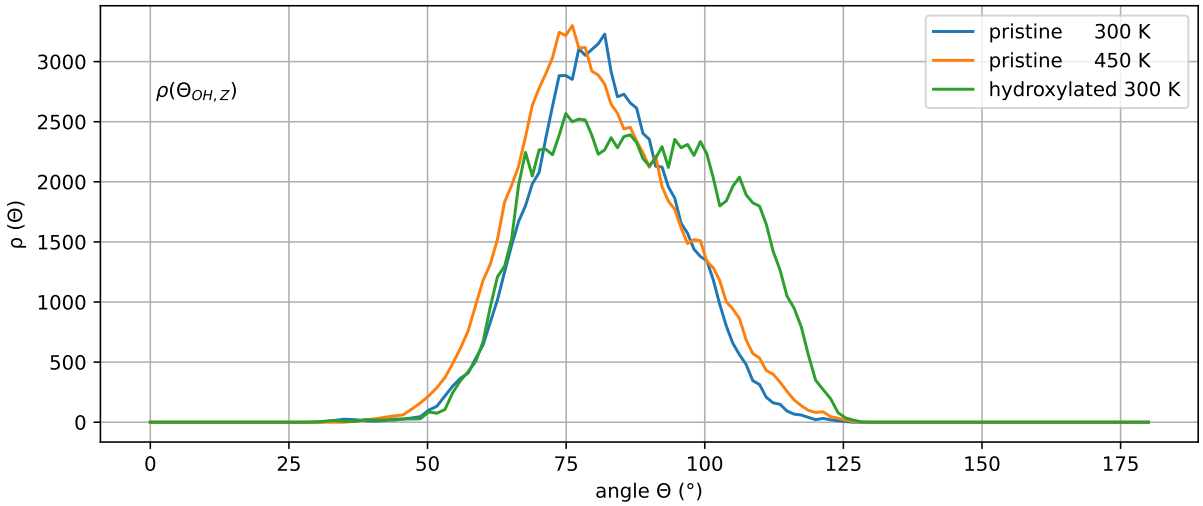

(b)

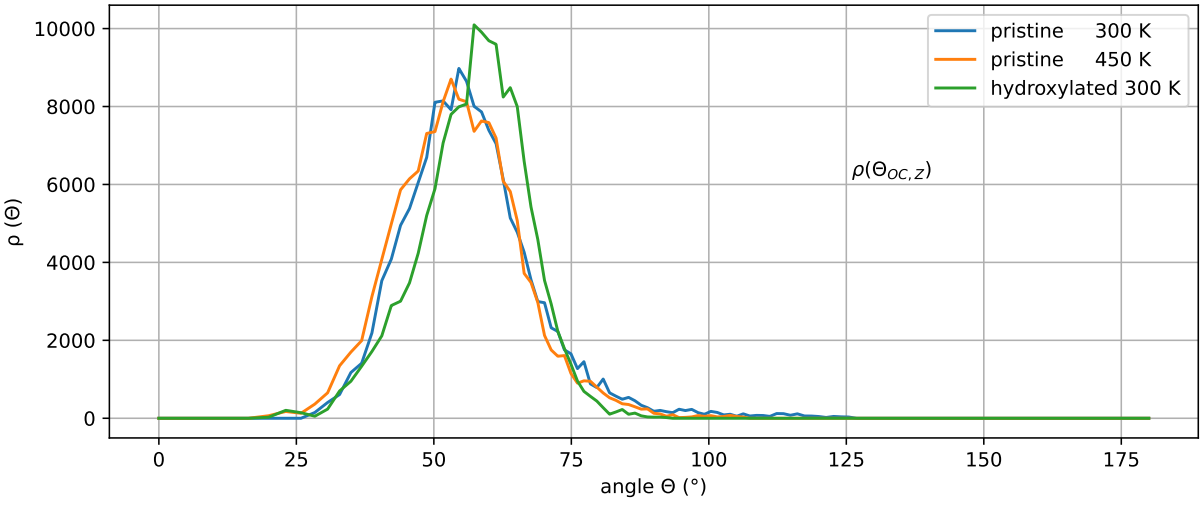

(c)

Figure 29: Distribution of orientations: (a) schematic representation of the angle, (b) angle between $O_{alcohol}$–H bond and surface normal Z (001) axis, and (c) angle between $O_{alcohol}$–C2 bond and surface normal Z (001) axis.

The distribution of the OH-Z angle (Figure 29 (b)) ranges from 50° to 125° for all three cases, with the highest probability between 70° and 90°. This suggests that the OH bond

points slightly away from the surface in all three cases. The hydroxylated system has a broader range of orientations and is wider for orientations higher than 90°, indicating that for the hydroxylated system, the OH bond points towards the surface at least one-third of the simulation time. This observation indicates an inclination for deprotonation in the hydroxylated system. However, once again, there is no significant difference in the orientation of adsorbed 2-propanol molecules between the pristine system at either 300 K or 450 K, with a slight broadening of the 450 K system due to the OH bonds being more dynamic at 450 K.

The distribution of the OC-Z angle (Figure 29 (c)) ranges from 25° to 90° for all three cases, with the highest probability occurring around 60°. This indicates that the OC vector points away from the surface. The orientation of adsorbed 2-propanol molecules does not differ significantly between the pristine system at either 300 K or 450 K, suggesting that temperature does not have a substantial impact on the orientation of adsorbed 2-propanol molecules.

5.2.5 A-terminated (001) Surface

To compare the results with the B-terminated (001) surfaces discussed in the previous sections, AIMD simulations for the A-terminated pristine (001) surfaces are also performed. Figure 30 and Figure 31 present the snapshots of the last configurations (after 20 ps AIMD runs) of simulations at 300 K and 450 K, respectively. As explained below (and evident in these figures), there are two main differences between the A-terminated and B-terminated (001) surfaces: (1) the nature of adsorption sites (Co^{2+}/Co^{3+} ions) and (2) surface reactivity (due to coordinatively unsaturated surface O^{2-} ions).

In Figure 30, it can be observed that at 300 K, all eight 2-propanol/2-propoxide molecules are adsorbed on the Co^{2+} (green) sites (as seen in the top view). This is in contrast to the behavior observed on the B-terminated surfaces, where only the Co^{3+} sites served as the adsorption sites. Additionally, two dissociation reactions of adsorbed 2-propanol occur, resulting in the formation of two 2-propoxide molecules. The two surface OH groups are highlighted by black circles in the snapshots. Four out of the total eight 2-propanol molecules remain molecularly adsorbed throughout the entire 20 ps AIMD simulation, while the remaining two 2-propanol molecules are mostly mobile in the contact layer.

Figure 31 demonstrates that at 450 K, the surface activity increases, leading to four dissociative adsorptions (indicated by black circles). In other words, an increase in temperature enhances surface reactivity and promotes proton transfer from the 2-propanol hydroxyl group to the surface lattice oxygen. This differs from the temperature impact on the B-terminated surface, where increasing the temperature did not induce 2-propanol dissociation (as discussed in section 5.2.4). The disparity in behavior and the higher reactivity of the A-terminated (001) surface can be attributed to the role of coordina-

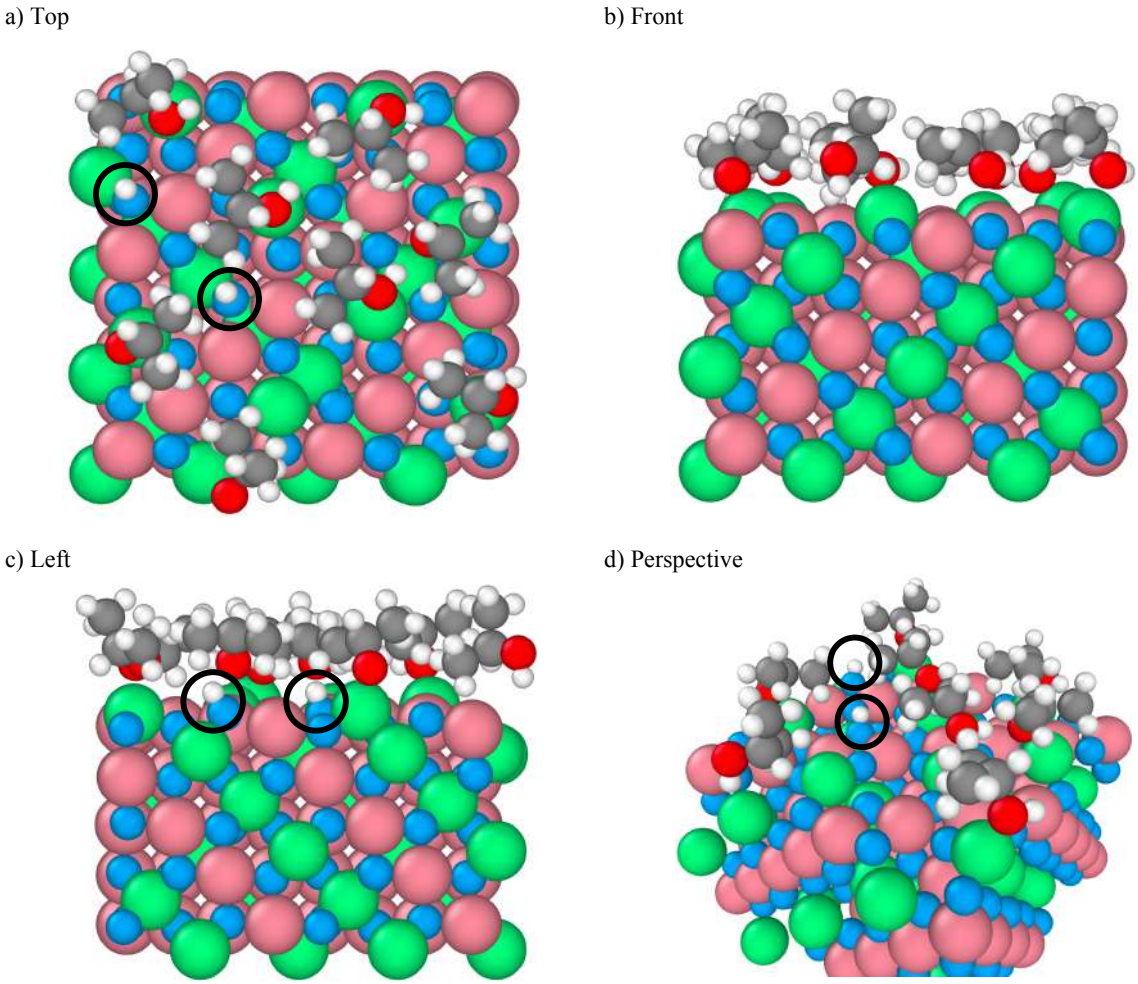

Figure 30: Snapshots of the final configuration of the AIMD simulation (top, front, left and perspective views) for 2-propanol adsorption on the A-terminated pristine Co_3O_4 (001) surface at 300 K. Co^{3+} (pink), Co^{2+} (green), O in Co_3O_4 (blue), O in 2-propanol (red), C (gray) and H (white). The surface OH groups are highlighted by black circle.

tively unsaturated lattice oxygen. The A-terminated (001) surface consists of two types of oxygen species: four-fold coordinatively saturated oxygen species and three-fold coordinatively unsaturated oxygen species. The latter is responsible for 2-propanol dissociation at both 300 K and 450 K (denoted by blue-colored atoms and highlighted by black circles in Figure 30 and Figure 31). A similar observation has been previously made for water dissociation on the Co_3O_4 (001) surfaces,[64] where these lattice oxygens were found to be responsible for the higher activity of the A-terminated surfaces in water dissociation.

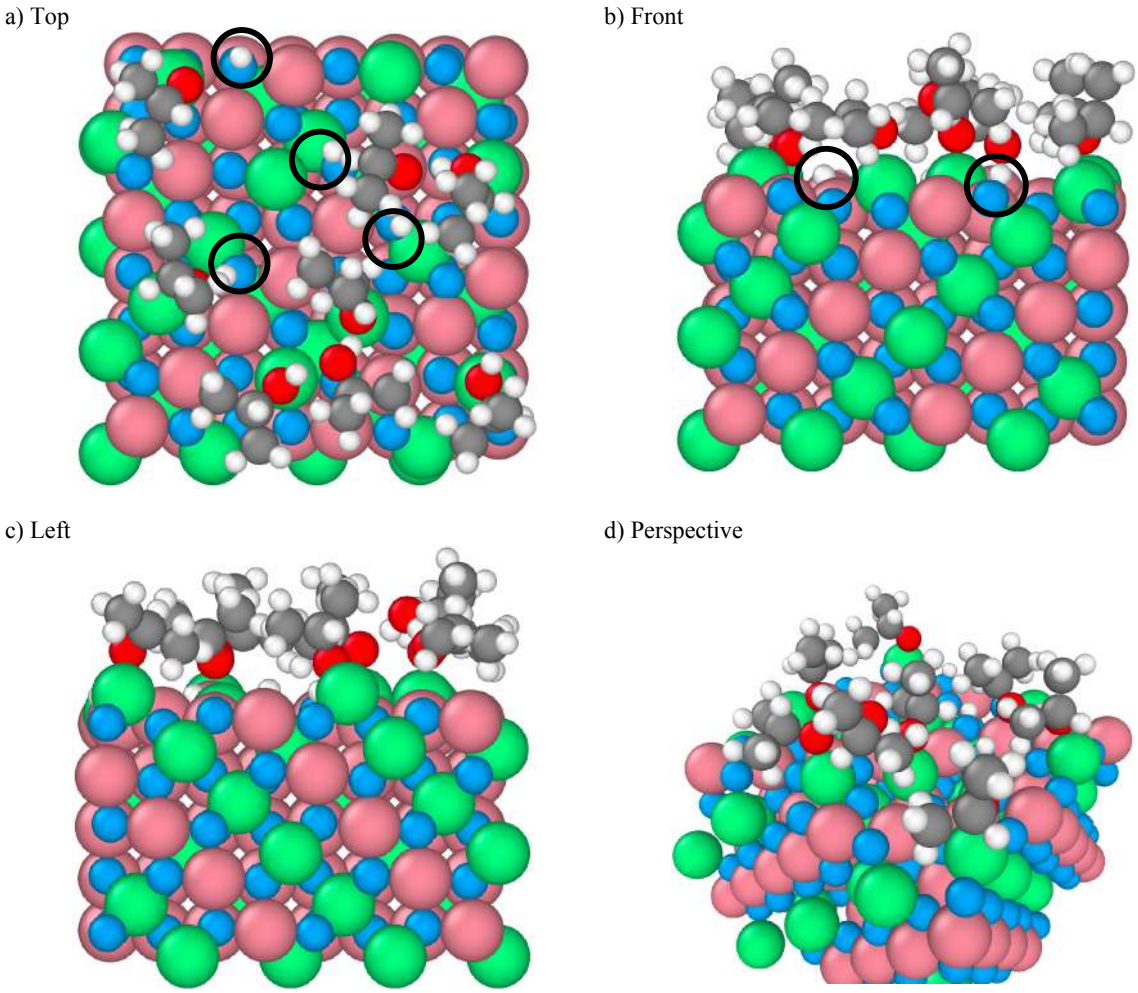

Figure 31: Snapshots of final configuration of AIMD simulation (top, front, left and perspective views) for 2-propanol adsorption on the A-terminated pristine Co_3O_4 (001) surface at 450 K. Co^{3+} (pink), Co^{2+} (green), O in Co_3O_4 (blue), O in 2-propanol (red), C (gray) and H (white). The surface OH groups are highlighted by black circle.

Proton Transfer

Figure 32 compares the $O_{alcohol}$–H (a) and $O_{surface}$–H (b) RDFs for the A-terminated (001) surfaces at two different temperatures: 300 K (green) and 450 K (violet). The RDFs for the corresponding B-terminated surfaces discussed in previous sections are shown by black and red dash-dotted lines, respectively.

In the $O_{alcohol}$–H RDFs (Figure 32 (a)), the peaks around 1 Å for the 300 K system (green) is approximately 70% higher than that of the 450 K system (violet), indicating more dissociation of 2-propanol at 450 K. The second peak (around 2.1 Å) represents the distance between the oxygen of the 2-propanol/2-propoxide molecules and the hydrogen of the CH group. The 450 K system (violet) exhibits a lower peak but wider distribution due to higher thermal fluctuations. In the distance between these two peaks, i.e., between 1.1–2 Å, the A-terminated systems have a higher probability compared to the B-terminated system, which are indicative of proton sharing.

Figure 32 (b) ($O_{surface}$–H RDFs) shows the major difference between the A-terminated and B-terminated systems around the first peak at 1 Å, indicating a higher degree of surface hydroxylation for the A-terminated systems. In the distance range of 1.75–2.75 Å, both B-terminated systems have a higher likelihood of finding a hydrogen atom near the $O_{surface}$. This is due to the greater accessibility of the 2-propanol hydroxyl hydrogen in their vicinity.

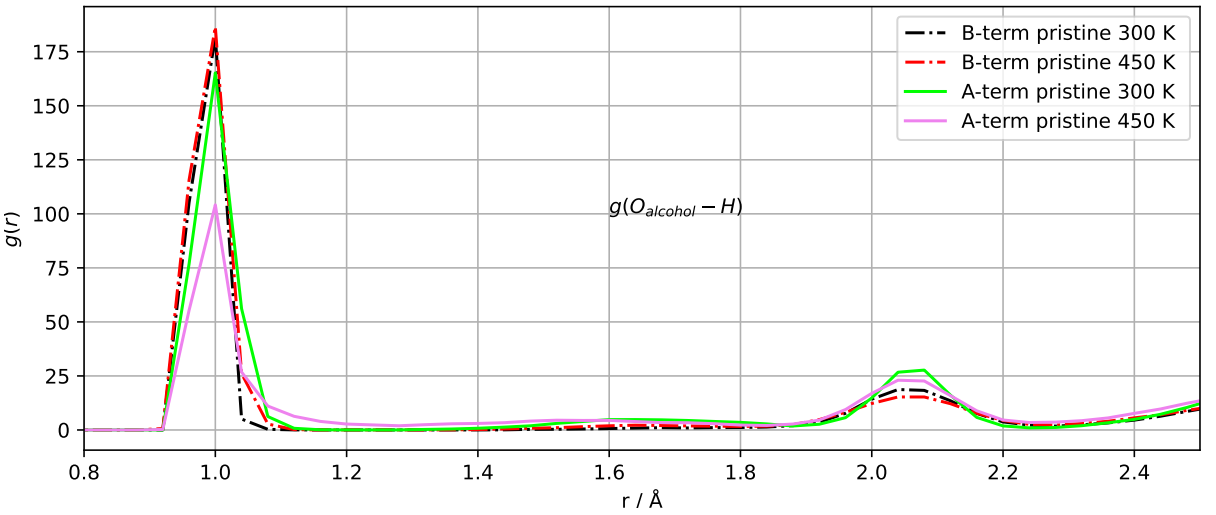

(a)

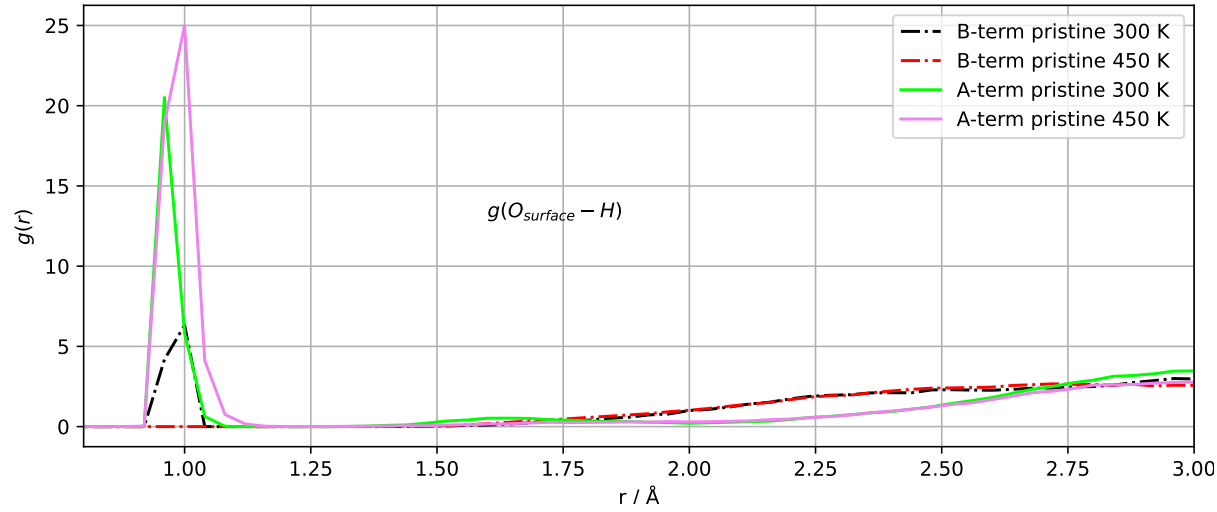

(b)

Figure 32: Radial distribution function of (a) $O_{alcohol}$ and all H and (b) $O_{surface}$ and all H.

C–O Bond

The $O_{alcohol}$–C RDFs (Figure 33) reveal significant differences between the A-terminated and B-terminated systems, particularly around the first peak. As depicted in this figure, the peaks for the B-terminated systems are approximately 20% lower and centered around the 1.5 Å region, indicating shorter C–O bonds of the adsorbed 2-propanol in the A-terminated systems.

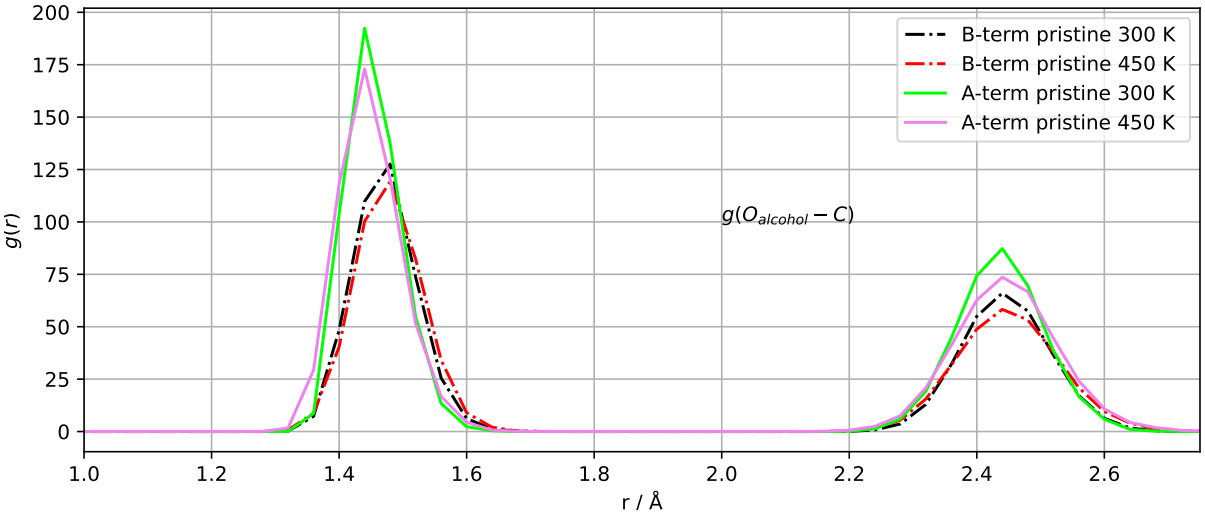

(a)

Figure 33: Radial distribution function of $O_{alcohol}$ and all C atoms.

Adsorption Geometry

The radial distribution functions between $O_{alcohol}$ and the closest Co ions (Figure 34) reveal distinct characteristics between the A-terminated and B-terminated systems. In the A-terminated systems, the first peak around 2 Å is split into two peaks: one at approximately 1.85 Å and the other at around 2.1 Å. This splitting is not observed in the RDFs of the B-terminated surfaces, where a single peak is dominant at the 2 Å distance. This discrepancy signifies the different nature of the adsorption sites between the two terminations. In the A-terminated systems, the adsorption sites primarily correspond to the Co^{2+} ions at a distance of 1.85 Å, while the nearby Co^{3+} ions contribute to the peak around 2.1 Å or occasionally act as temporary adsorption sites. Conversely, the B-terminated surfaces exclusively feature Co^{3+} ions as the adsorption sites without the presence of other Co^{2+} or Co^{3+} sites in their proximity.

In order to compare the orientation of adsorbed 2-propanol species on the A-terminated and B-terminated (001) surfaces, we analyze the orientational distribution of the angle between the $O_{alcohol}$–C2 vector and the surface normal Z (001) axis, as shown in Figure 35.

Figure 35 depicts the distribution of the OC–Z angle, which spans from 0° to 90° for both A-terminated systems (at 300 K and 450 K), with the highest probability observed between 30° to 50°. An angle of 0° signifies that the O–C vector is parallel to the surface normal, indicating a vertical adsorption orientation of the 2-propanol molecule on the A-terminated (001) surface. Conversely, an angle of 90° indicates a more horizontal arrangement of the 2-propanol molecules on the surface.

The distributions for the A-terminated systems are wider compared to those of the B-terminated systems, indicating increased dynamics of the adsorbed 2-propanol species on the A-terminated surfaces. Furthermore, the distributions for the 450 K system (violet) are broader than those for the 300 K system, indicating a wider range of mobility for

the 2-propanol molecules at higher temperatures. This behavior contrasts with the B-terminated systems, where the temperature does not exert a significant influence on the orientation of the 2-propanol molecules.

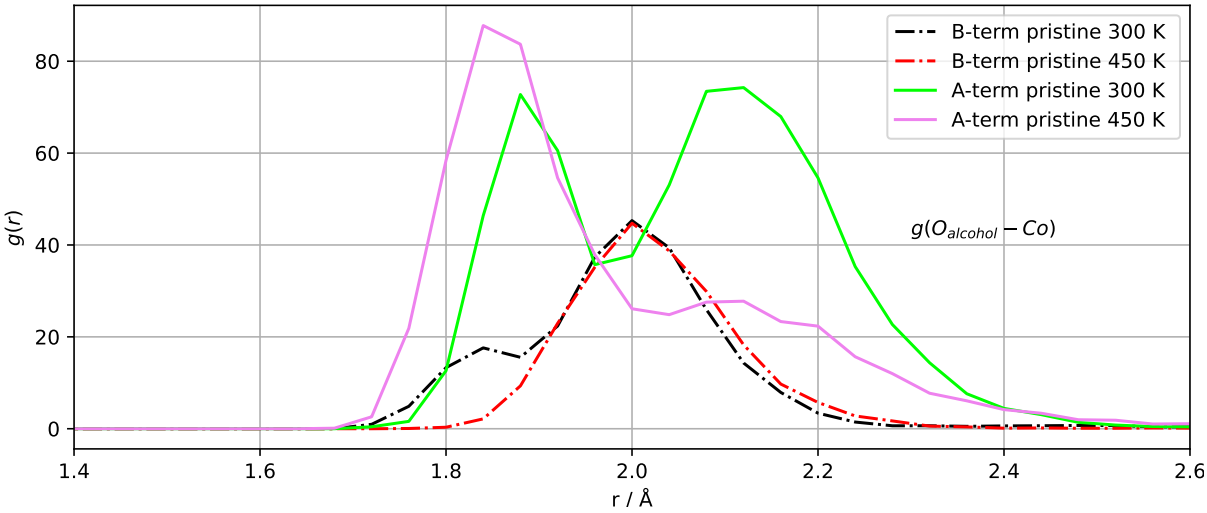

(a)

Figure 34: Radial distribution function of $O_{alcohol}$ and the closest Co ion.

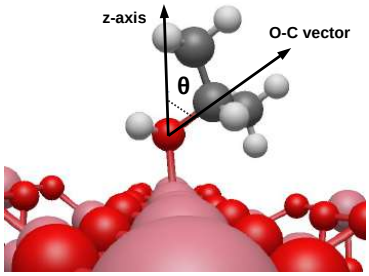

(a)

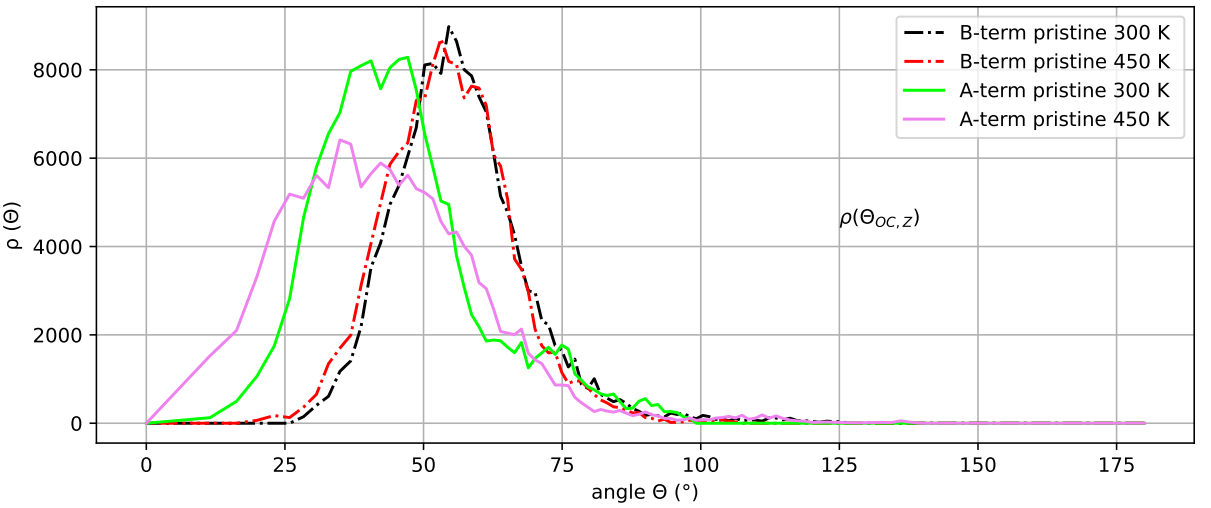

(b)

Figure 35: Distribution of angle between $O_{alcohol}$–C2 vector and surface normal Z (001) axis.

5.3 Co_3O_4 (111) / 2-propanol Interaction

Although the primary focus of this work is on the Co_3O_4 (001) surface, this section also presents some preliminary findings on the (111) and (110) surfaces, specifically regarding 2-propanol activation. The objective is to develop a comparative understanding of the three surfaces and determine which one exhibits higher reactivity for 2-propanol activation.

AIMD simulations are conducted for a system comprising a pristine Co_3O_4 (111) surface at 300 K. Figure 36 displays snapshots from the final configuration (after 20 ps run) of the simulation for the pristine surface. All eight 2-propanol molecules undergo dissociative adsorption on the Co^{3+} sites. Comparison between the initial and final configurations reveals that the associated Co^{3+} adsorption sites remain unchanged throughout the simulation. From the perspective views, it is evident that surface hydroxylation occurs, resulting from eight proton transfers to the surface lattice oxygen. No partial oxidation of 2-propanol or the formation of acetone is observed during the 20 ps simulation.

The evolution of distances of O–H, C–H, C–O, and Co^{3+}–O for a dissociatively adsorbed 2-propanol molecule during 20 ps of AIMD simulation is shown in Figure 37. The figure illustrates that the O–H bond cleavage occurs after approximately 2.5 ps of the simulation, which leads to a shortening of the Co^{3+}–O distance. Additionally, a relatively small shortening of the C–O bond is observed, while the C–H bond remains relatively unchanged throughout the simulation, suggesting that no dehydrogenation (C–H bond cleavage) has occurred.

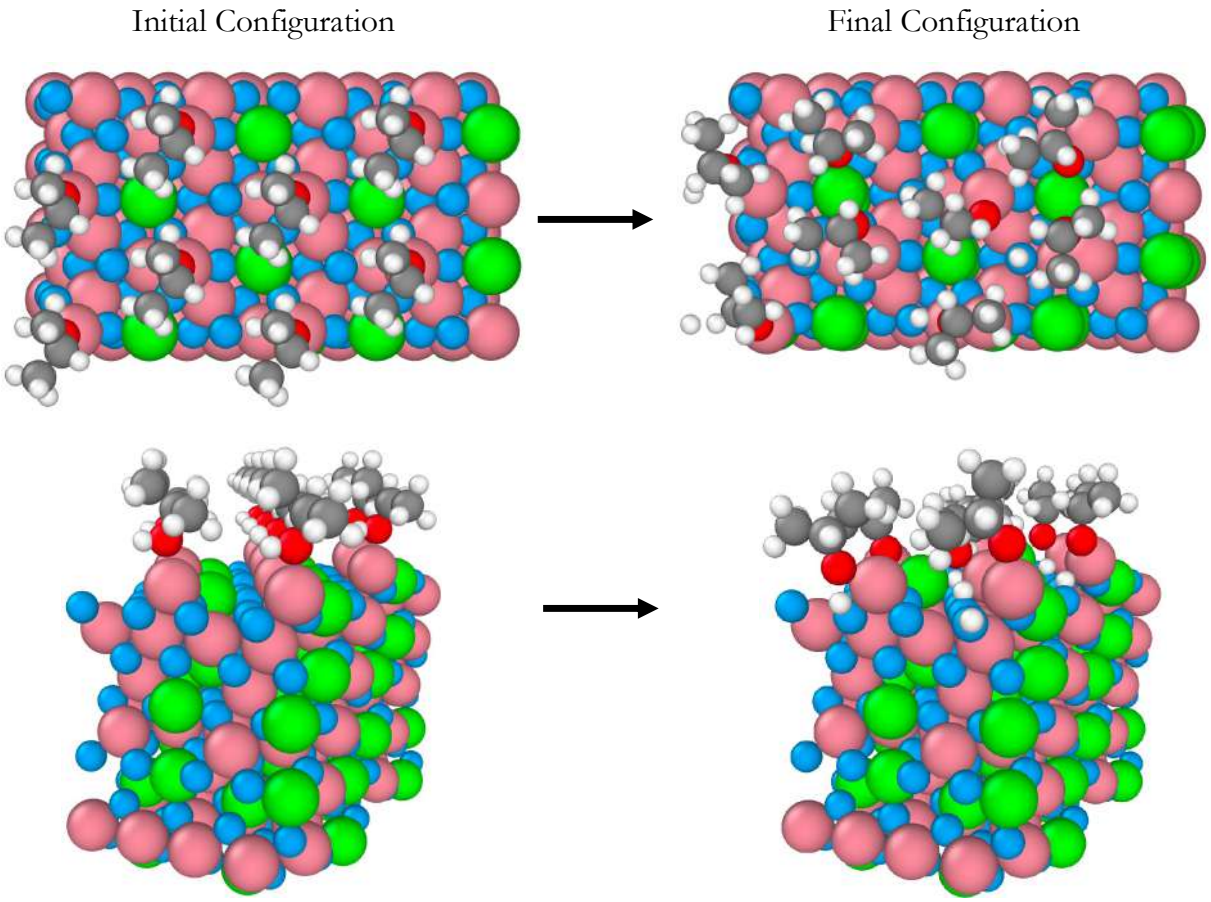

Figure 36: Snapshots of the initial and final configurations of the AIMD simulation (top and perspective views) for 2-propanol adsorption on the B-terminated pristine Co_3O_4 (111) surface at 300 K. Co^{3+} (pink), Co^{2+} (green), O in Co_3O_4 (blue), O in 2-propanol (red), C (gray) and H (white). Eight proton transfers to the surface lattice oxygen can be observed.

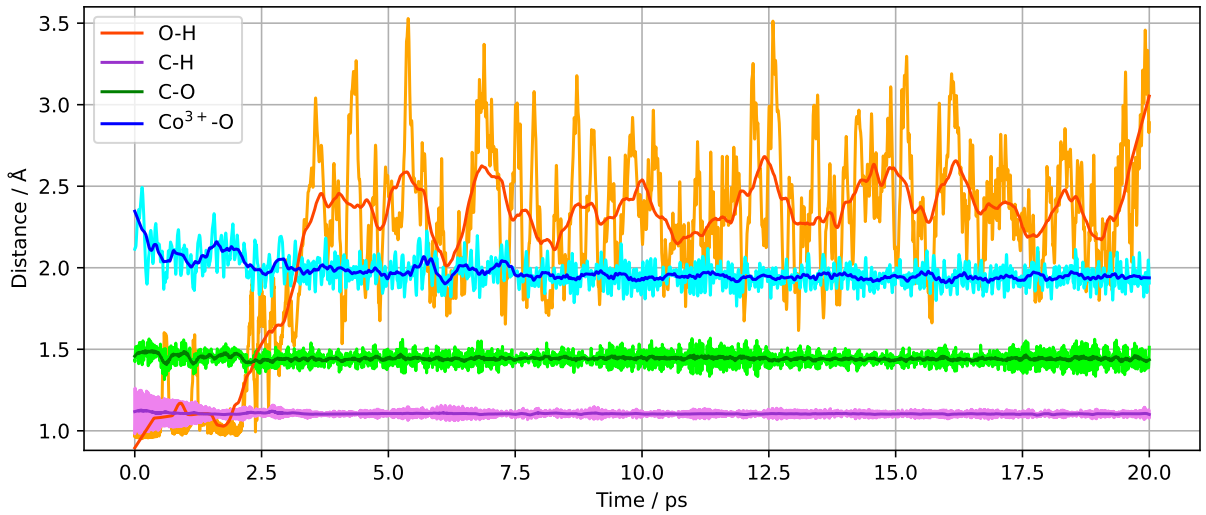

Figure 37: Evolution of O–H, C–H, C–O and Co^{3+}–O distances for a dissociatively adsorbed 2-propanol molecule.

A notable distinction between the B-terminated (111) and (001) surfaces is the formation of Co^{3+}– $O_{2\text{-propoxide}}$ – Co^{2+} bridges between adsorption sites and the adsorbates on the (111) surface. Figure 38 depicts a simulation snapshot illustrating two such bridges represented by black lines. The formation of these bridges can be attributed to the unique characteristics of the surface's tetrahedrally coordinated Co^{2+} ions. While the topmost Co^{2+} ions on the B-terminated (001) surface are coordinatively saturated, the three-fold coordinatively unsaturated nature of these ions on the B-terminated (111) surface leads to their inclination to participate in 2-propanol adsorption, as seen in Figure 38.

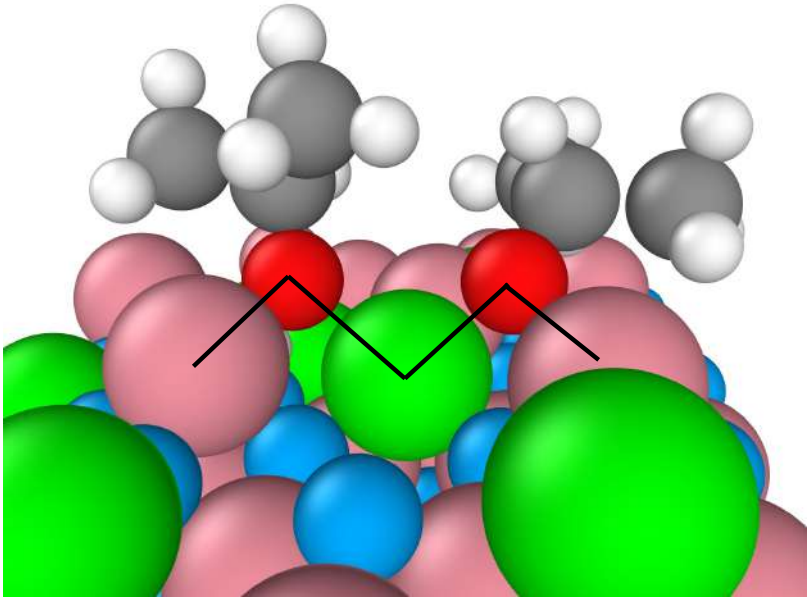

Figure 38: Two Co^{3+}– $O_{2\text{-propoxide}}$ – Co^{2+} bridges on the B-terminated pristine Co_3O_4 (111) surface at 300 K. Co^{3+} (pink), Co^{2+} (green), O in Co_3O_4 (blue), O in 2-propoxide (red), C (gray) and H (white).

Figure 39 showcases the charge density difference (CDD) plot for the AIMD simulation of the final configuration of the system depicted in Figure 36. The system consists of the B-terminated pristine Co_3O_4 (111) surface at 300 K with eight dissociatively adsorbed 2-propanol molecules. Several observations can be made:

- One of the Co^{2+} ions (represented by a black circle) plays a significant role in 2-propanol adsorption through its participation in the Co^{3+}–$O_{2\text{-propoxide}}$–Co^{2+} bridge (Figure 38). The ion is surrounded by cyan color, indicating a loss of electron density upon 2-propanol adsorption.

- The third layer of the slab, consisting of Co^{3+} ions (depicted by an orange rectangle), is also electronically involved, distinguishing it from the B-terminated (001) surface where only the topmost layer and, to a lesser extent, the second layer were involved during adsorption.

- The hydrogen in the CH_3 groups (shown as black rectangles) does not exhibit electron density depletion or accumulation, in contrast to the B-terminated (001) surface. This can be explained by the hydroxylation of all coordinatively unsaturated surface oxygens through proton transfers on the (111) surface (see Figure 36), while the majority of such surface oxygens remain intact on the B-terminated (001) surface. Consequently, the interaction between the H in CH_3 groups and the surface oxygens on the B-terminated (111) surface is less pronounced than on the B-terminated (001) surface.

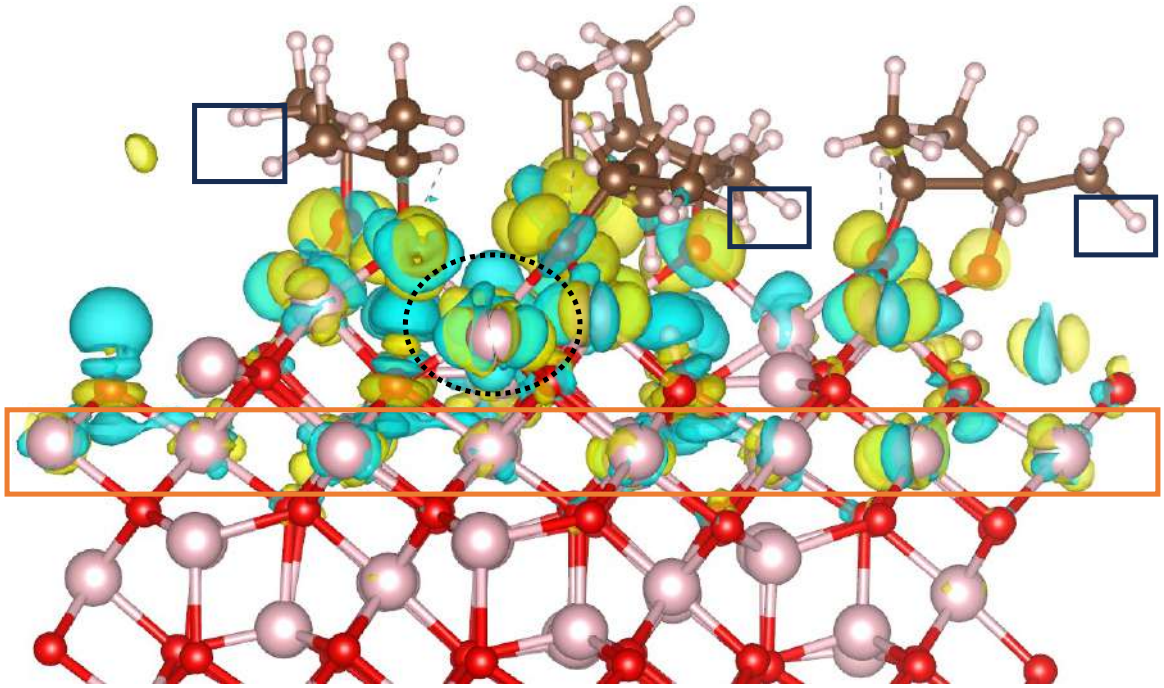

Figure 39: Charge density difference plot for the adsorption of 2-propanol on Co^{3+} sites of the B-terminated Co_3O_4 (111) surface at 300 K. The iso-surfaces are drawn at density levels of – 0.003 (cyan) and + 0.003 (yellow) e $Å^{-3}$. The yellow regions indicate the accumulation of electron density, while the cyan regions indicate the depletion of electron density.

5.3.1 Mars-van Krevelen Mechanism

Utilizing a hydroxylated (111) surface, where the surface is pre-exposed to water and surface OH groups are formed, leads to the generation of water from lattice oxygen through the Mars-van Krevelen mechanism (Figure 40). The initial configuration is shown on the left side, with the lattice oxygen involved in the Mars-van Krevelen mechanism highlighted in red. After 5 ps, the lattice OH group abstracts the hydroxyl hydrogen from 2-propanol, resulting in the conversion of the lattice OH into a water molecule and 2-propanol into 2-propoxide. Consequently, an oxygen vacancy emerges within the lattice at the position previously occupied by the lattice oxygen, as indicated by the black circle.

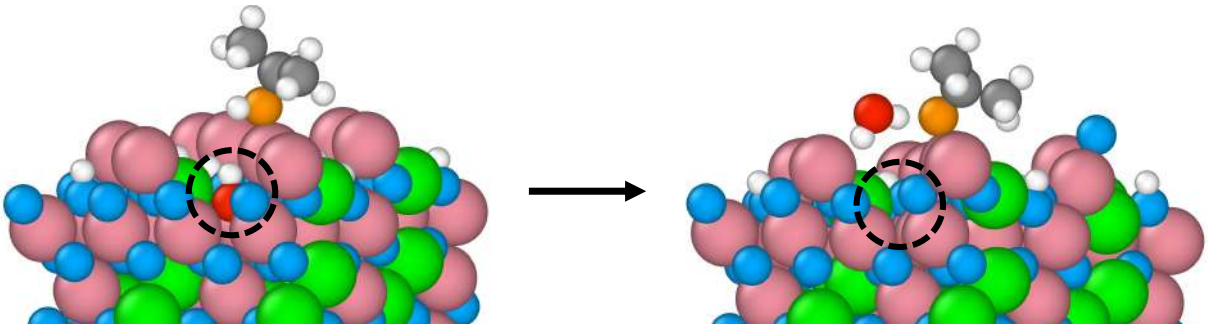

Figure 40: Formation of water from surface oxygen through the Mars-van Krevelen mechanism. Co^{3+} (pink), Co^{2+} (green), O in Co_3O_4 (blue), O in 2-propanol (orange), C (gray) and H (white). The lattice oxygen which participates in the Mars-van Krevelen mechanism is denoted in red. The created vacancy is shown with a black circle on the right side.

5.4 Co_3O_4 (110) / 2-propanol Interaction

AIMD simulations are conducted for a system featuring the B-terminated pristine Co_3O_4 (110) surface at temperatures of 300 K and 450 K. Figure 41 showcases snapshots of the simulation's initial (left) and final configuration (right) at 300 K. In this case, six out of the eight 2-propanol molecules are molecularly adsorbed onto Co^{3+} sites, while the remaining two undergo dissociation on the surface, resulting in the formation of two 2-propoxide molecules. Notably, the associated Co^{3+} adsorption sites remain unchanged throughout the simulation, as evident from the top views of the initial and final configurations. Analogous to the (001) and (111) surfaces, no partial oxidation of 2-propanol occurs, thereby precluding the formation of acetone.

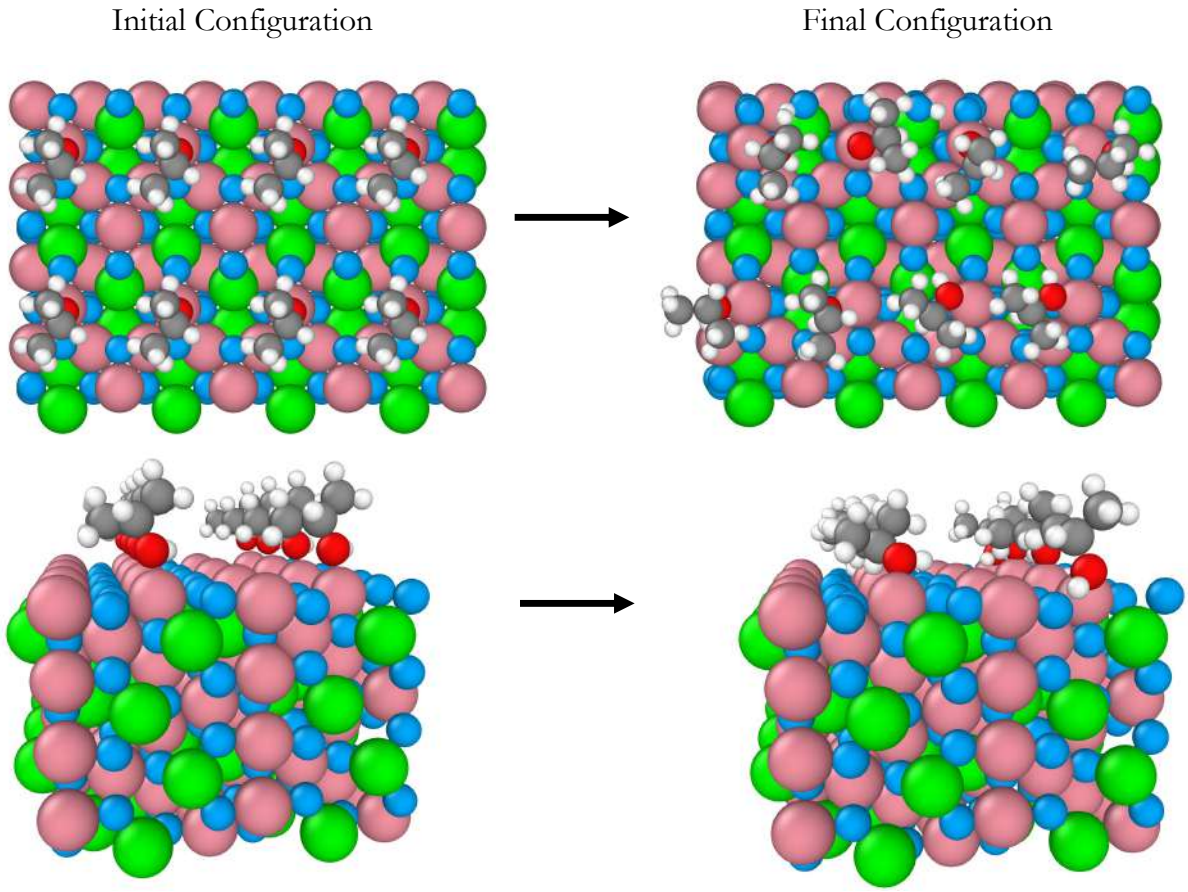

Figure 41: Snapshots of the initial and final configurations of the AIMD simulation (top and perspective views) for 2-propanol adsorption on the B-terminated pristine Co_3O_4 (110) surface at 300 K. Co^{3+} (pink), Co^{2+} (green), O in Co_3O_4 (blue), O in 2-propanol (red), C (gray) and H (white). Two proton transfers to the surface lattice oxygen can be observed.

5.4.1 Two–Fold Lattice Oxygen

The activity (for 2-propanol dissociation) of the (110) surface for 2-propanol activation

significantly increases as the temperature is raised to 450 K, as shown in Figure 42. In fact, six 2-propanol molecules dissociate on the surface, resulting in the formation of six surface OH groups. This is in contrast to the case at 300 K where only two dissociations are observed.

What makes the (110) surface particularly reactive at higher temperatures compared to the (001) and other surfaces? To answer this question, it is important to consider the nature of the lattice oxygen species on the B-terminated (110) surface. On the other surface terminations (i.e. A-terminated and B-terminated (001), A-terminated and B-terminated (111), and A-terminated (110)), the surface lattice oxygen are either three-fold coordinatively unsaturated surface oxygen or four-fold coordinatively saturated oxygen. However, what distinguishes the B-terminated (110) surface is the presence of two-fold coordinatively unsaturated oxygen on the surface, which are highly active. As shown in Figure 42, all protons are transferred to these violet "two-fold" coordinatively unsaturated oxygen, indicating their high reactivity. Therefore, it can be speculated that the increased surface reactivity of the B-terminated (110) surface at higher temperatures is due to the activation of these two-fold coordinatively unsaturated oxygen. The superior catalytic activity of the B-terminated (110) surface has been confirmed experimentally.[31]

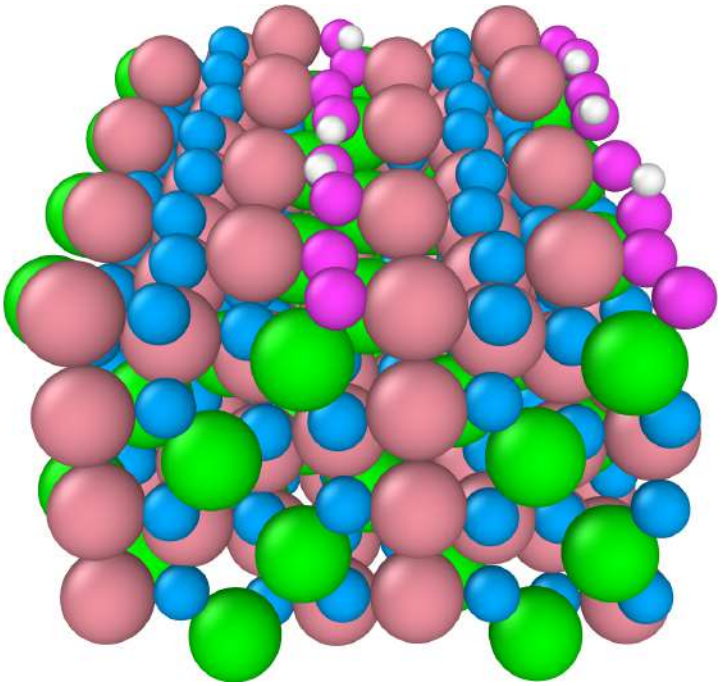

Figure 42: Snapshot of the final configuration of the B-terminated Co_3O_4 (110) surface at 300 K. The adsorbed 2-propoxide molecules are removed for visualization. The "two-fold" surface oxygens are denoted in violet. Co^{3+} (pink), Co^{2+} (green), two-fold O (violet), other O in Co_3O_4 (blue), and H (white).

5.5 Comparison Between (001), (111) and (110) Surfaces

The preceding sections have individually discussed different aspects of the (001), (111), and (110) surfaces. However, this section aims to provide a comparative analysis of these three surfaces. To accomplish this objective, the surfaces will be evaluated and compared based on two criteria: 1) surface reactivity for 2-propanol activation, and 2) surface reconstruction. This section only focuses on the B-terminated surfaces.

2-propanol Activation

The activity of all three surfaces at two different temperatures, 300 K and 450 K, is shown in Table 1. Initially, all 6 systems started with eight 2-propanol molecules. Several observations can be made from this table:

- The highest dissociation activity belongs to the (111) surface either at 300 K or 450 K with 2-propanol converted to 2-propoxide.
- The lowest activity belongs to the (001) surface at 450 K with no molecule being dissociated.
- The activity of the (110) surface is in between the activity of (111) and (001) surfaces at both 300 K and 450 K.
- Temperature has the highest impact on the activity of (110) surface by increasing the activity by overall 60 percent.
- No formation of acetone is observed on any of the surfaces.

	(001)-B		(111)-B		(110)-B	
	300 K	450 K	300 K	450 K	300 K	450 K
No. Initial 2-propanol	8	8	8	8	8	8
No. Final 2-propanol	7	8	0	0	6	2
No. Final 2-propoxide	1	0	8	8	2	6
No. Final Acetone	0	0	0	0	0	0

Table 1: Number of initial 2-propanol, final 2-propanol, final 2-propoxide, and final acetone for (001), (111), and (110) surfaces at 300 K and 450 K temperatures.

Surface Reconstruction

It is a well-known phenomenon that the surface, during interaction with the gas or liquid phases, is not static but rather dynamic. In the AIMD simulation, such dynamic behavior can also be observed. Figure 43 shows the mobility of surface atoms during the 20 ps of the simulation. On the left side, the initial surface configuration for (001), (111), and (110) is shown, respectively. On the right side, the trajectory lines are presented. It can be seen that the (001) surface is the most static surface compared to the other two surfaces, and the (111) surface is the most dynamic surface. Specifically, the higher mobility of the Co^{3+} ions (pink) in (111) can be clearly seen compared to the other two. Such higher activity has been shown previously (see Figure 38) to reconstruct the surface and form Co^{3+}– $O_{2\text{-propoxide}}$ – Co^{2+} bridges.

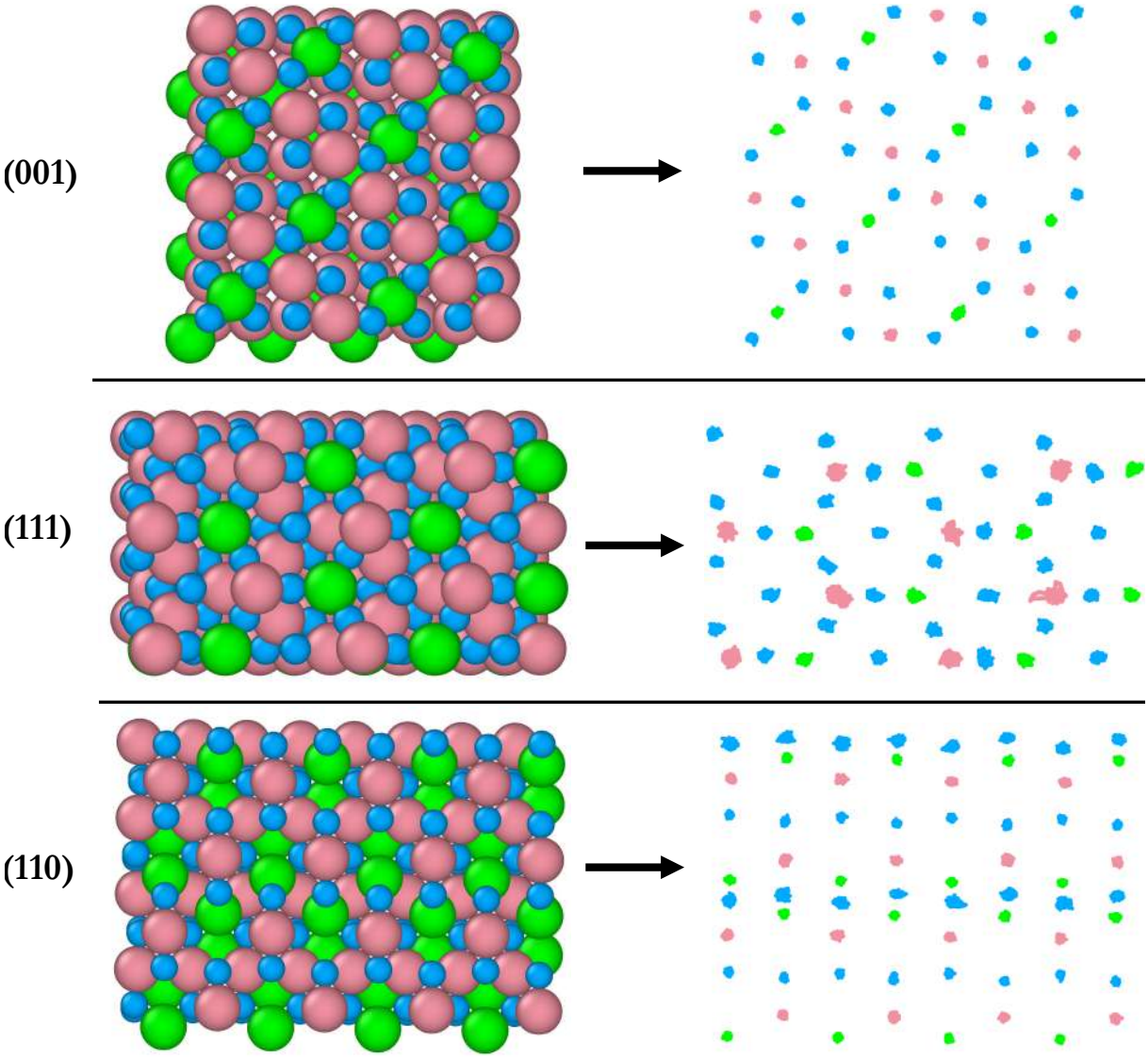

Figure 43: Initial configuration (left) of AIMD simulation (top-view) and trajectory lines (right) of surface atoms for (001), (111), and (110) surfaces at 300 K. Co^{3+} (pink), Co^{2+} (green), and O in Co_3O_4 (blue)).

The most dynamic atoms of the (110) surface are some of the surface oxygen atoms (blue). These are indeed the previously described "two-fold" surface oxygens that were responsible for all the 2-propanol dissociation on (110) surface. The mobility of atoms on the (110) surface falls between that of the atoms on the (001) and (111) surfaces.

Overall, it can be concluded that both (111) and (110) surfaces exhibit higher reactivity towards 2-propanol activation compared to the (001) surface. The (111) surface shows slightly higher activity than the (110) surface, although this claim should be made cautiously due to the limited statistical significance of the results based on only eight molecules. Additionally, the reactivity of the (110) surface was observed to increase by 60% by increasing temperature, mostly in the later stages of the simulation. Thus, further investigation using longer simulations is necessary to make more robust predictions. In summary, this thesis concludes that the (111) and (110) surfaces are more active for 2-propanol activation, although it is difficult to confidently determine a preference between them. Nonetheless, it was found that the temperature has the most significant impact on the reactivity of the (110) surface.

5.6 Digression: Power Spectra

Recently, researchers from the CRC/TRR 247 project were able to provide spectra of 2-propanol adsorbed on various transition metal oxides using diffuse reflectance infrared Fourier transform spectroscopy (DRIFTS) techniques.[29] However, some peaks in the spectra cannot be ascribed to specific bands. Motivated by this difficulty, the aim of this section is to provide power spectra from AIMD trajectories at various conditions. The power spectrum, also known as the vibrational density of states (VDOS), is obtained from the Fourier transform of the atomic velocity autocorrelation function. Unlike experimentally accessible vibrational spectra, the power spectrum encompasses all motions of a system without being restricted by selection rules.[17] It is hoped that this procedure can complement the experimental DRIFTS results and aid in elucidating the experimental spectra. The advantage of this computational technique is that specific structures can be intentionally included/excluded to include/exclude their signature from the global spectra.

To achieve this goal, an AIMD simulation of a gas-phase 2-propanol molecule is performed to provide a reference spectrum of the 2-propanol molecule. By comparing it to the adsorbed 2-propanol and 2-propoxide species (discussed in previous sections), useful information regarding the effect of various parameters on the power spectra can be obtained. In the next chapter, the effect of solvation on the power spectra can be traced when 2-propanol is solvated in aqueous solution. Figure 44 illustrates the power spectrum of a gas-phase 2-propanol molecule equilibrated at 300 K (black dash-dotted line) and the power spectrum of an adsorbed 2-propanol molecule on the B-terminated Co_3O_4 (001)

surface at 300 K (blue line).

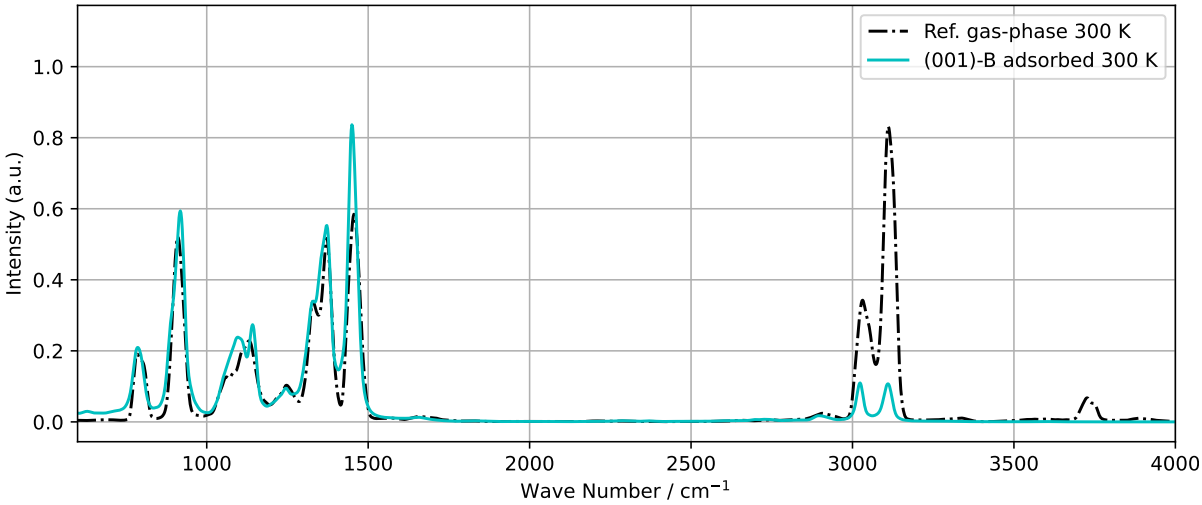

Figure 44: Power spectra of a gas-phase 2-propanol molecule equilibrated at 300 K (black dash-dot line) and adsorbed 2-propanol molecule on the B-terminated Co_3O_4 (001) surface at 300 K (blue line).

Some of the characteristic peaks in Figure 44 can be ascribed to specific bands, as follows:

- C–H stretching modes: These vibrations involve stretching of the C–H bonds in the molecule. The peaks around 3050 cm^{-1} and 3100 cm^{-1} may be ascribed to the symmetric and asymmetric stretching modes of CH_3, respectively, while the small band at 2850 cm^{-1} might be attributed to the CH bonds.
- C–H bending modes: These vibrations involve bending of the C-H bonds in the molecule. The in-plane bending modes may appear as peaks around 1350-1450 cm^{-1}, while the out-of-plane bending modes may appear as peaks around 650-900 cm^{-1}.
- O–H stretching mode: This vibration involves stretching of the O-H bond in the molecule. The peak around 3600-3700 cm^{-1} may be ascribed to this band.
- O–H bending mode: This vibration involves bending of the O–H bond in the molecule. This mode may appear as a peak around 1200-1400 cm^{-1}.
- C–O bending mode: This mode contributes to the bands around 1700 cm^{-1} and is indicative of acetone.

Figure 45 shows the power spectra of adsorbed 2-propanol on B-terminated surfaces (001), (111), and (110). The main difference between the three spectra is the region between 2800-3100 cm^{-1}. The peaks around 3050 cm^{-1} and 3100 cm^{-1} can be assigned to

the symmetric and asymmetric stretching modes of CH_3, respectively, and the small band at 2850 cm^{-1} to the C–H bonds. Additionally, the difference in the 1100-1300 cm^{-1} region can be attributed to the O–H bending mode.

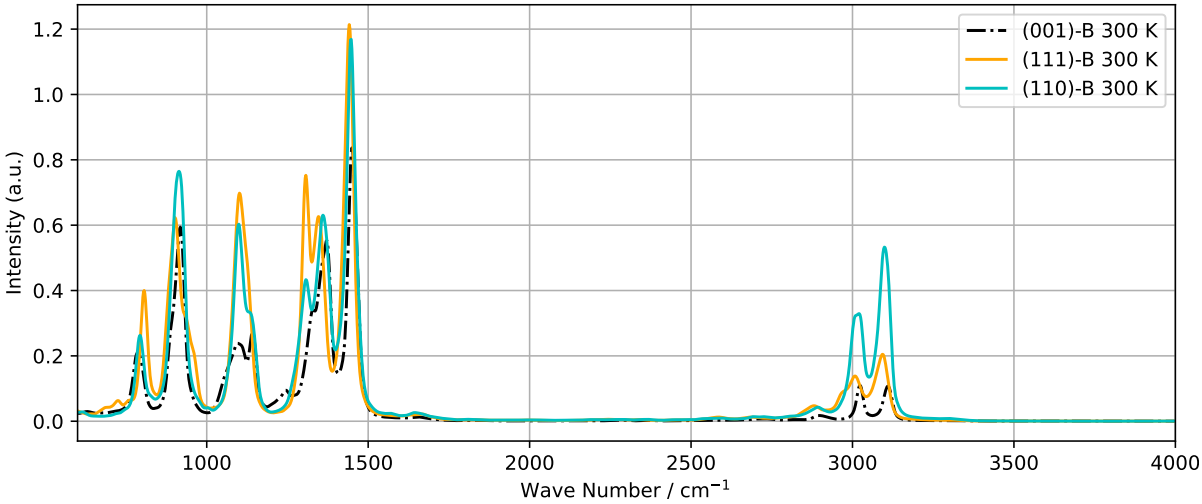

Figure 45: Power spectra of a adsorbed 2-propanol molecule equilibrated at 300 K on B-terminated surfaces (001), (111), and (110).

6 Structure, Dynamics and Reactivity of Co_3O_4 (001)/2-propanol/ Water and Co_3O_4 (001)/2-propanol/Oxygen Interfaces

Note: some parts of this chapter have been previously published in the journal of Applied Surface Science Advances under the title "Influence of Temperature, Surface Composition and Electrochemical Environment on 2-propanol Decomposition at the Co_3O_4 (001)/H_2O Interface".[79]

6.1 Overview

The interaction between water and A-terminated and B-terminated Co_3O_4 (001) surfaces has been extensively studied by Kox et al.[64] In this chapter, the investigation focuses on the interaction between 2-propanol and the Co_3O_4 (001)/H_2O interface, building upon their research and the previous chapter. The objective is to gain insights into the oxidation process of 2-propanol to acetone at this interface, considering factors such as temperature, surface structure, and electrochemical environment.

Ab initio molecular dynamics simulations are conducted to examine the behavior of a single hydrated 2-propanol molecule at the interface. On the A-terminated and B-terminated surfaces, adsorption of 2-propanol occurs on the Co^{2+} and Co^{3+} sites, respectively, without experiencing bond cleavage. Under oxidative conditions, achieved by partially dehydrogenating the hydroxyl/water adsorbate layer, dehydrogenation of the hydroxyl group is observed on both surface terminations. This results in the formation of adsorbed 2-propoxide. On the B-terminated surface, which is less hydroxylated, the reaction progresses with C–H bond cleavage at the 2-carbon atom. Throughout the approximately 20 ps simulation, the oxidation product, acetone, remains adsorbed on the Co^{3+} site. The presence of adsorbed hydroxyl groups facilitates the deprotonation steps, as hydrogen atoms from the reactant molecule are transferred to form adsorbed water molecules. However, increasing the system temperature from 300 K to 450 K does not lead to oxidation through deprotonation of the 2-propanol molecule.

Furthermore, the role of the B-terminated (001) surface in the partial oxidation of 2-propanol is investigated and found to be favorable due to the formation of an epitaxial water layer. Additionally, a comparison is made between the partial oxidation of 2-propanol in the gas phase and liquid phase. The findings highlight fundamental differences between the two environments. In aqueous solution, oxidation occurs through stepwise reactions with stabilized proton transfer facilitated by the presence of liquid water. In contrast, oxidation in the gas phase involves simultaneous/concerted charge transfers. Oxidation in the gas phase at high temperature reveals the formation of water from the

adsorbed oxygen species.

6.2 2-propanol Oxidation in the Liquid Phase

6.2.1 Simulation Systems

A-terminated Co_3O_4 (001) Surfaces

An 11-layer Co_3O_4 slab with one 2-propanol molecule and 60 water molecules is simulated at room temperature as the reference system. The topmost and bottommost layers of the slab consisted of 8 Co^{2+} ions in a (2×2×2) supercell configuration. To investigate the influence of an increased temperature, a system with the same composition was studied at T = 450 K. Subsequently, the redox conditions near the interface were modified at room temperature to enhance reactivity and stimulate hydrogen transfer and/or the oxidation reaction to acetone. This was achieved by removing several hydrogen atoms from the water film. The reported results correspond to a system where 8 hydrogen atoms were removed, resulting in a film composed of 52 water molecules and 8 hydroxyl groups.

Figure 46 shows snapshots of the final equilibrium configurations obtained from the equilibrated production trajectories. Water undergoes partial dissociation on the topmost Co^{2+} layer as well as on the mixed layer below, consisting of 16 Co^{3+} and 32 O^{2-} ions. Two types of hydroxyl groups should be distinguished: those resulting from water dissociation, which coexist with intact water molecules on Co^{2+} and Co^{3+} sites, and surface hydroxyls formed through proton transfer from the water film to surface oxygen. In the reference system, 2-propanol binds molecularly to the Co^{2+} site. At T = 450 K and under oxidative conditions, 2-propoxide is present at the interface. In all cases, the Co^{2+} ions serve as the adsorption sites, indicated by green circles in Figure 46.

B-terminated Co_3O_4 (001) Surfaces

To investigate the effect of the electrochemical environment and temperature on 2-propanol decomposition on the less reactive B-terminated surface, the same procedure as for the A-terminated surface is followed. Figure 47 presents snapshots of the final equilibrium configurations of the contact layer of the B-terminated (001) surface. This layer consists of 16 Co^{3+} and 32 O^{2-} ions interacting with 2-propanol and a water film under stoichiometric reference conditions at 300 K (left), in a hydrogen-deficient oxidative environment at 300 K (center), and in a stoichiometric environment at T = 450 K (right). The displayed water molecules in the contact layers illustrate that the 2-propanol/acetone molecules are adsorbed on the Co^{3+} adsorption sites, indicated by pink circles in Figure 47. Notably, an epitaxial water layer forms on the B-terminated (001) surface, as can be observed in the front view of Figure 47 in all three systems. The significance of this epitaxial water layer for the partial oxidation of 2-propanol will be discussed in section 6.2.6.

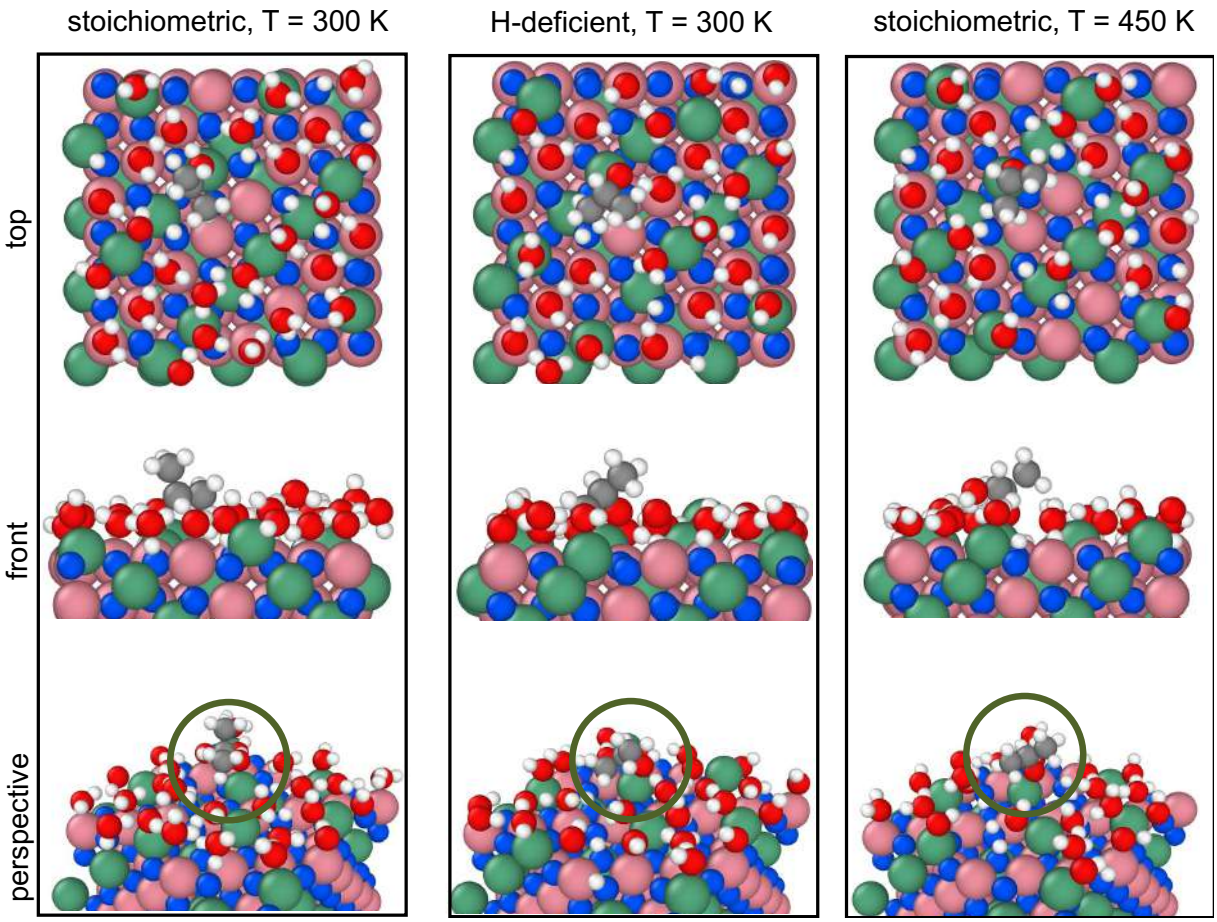

Figure 46: Snapshots of the final configurations of the AIMD simulations are depicted, showcasing the adsorption of 2-propanol at the A-terminated Co_3O_4 (001)/H_2O interface. The images present top, front, and perspective views. On the left, the stoichiometric reference system at 300 K is displayed, while the center image represents the H-deficient oxidative environment at 300 K. Additionally, the configuration in a stoichiometric environment at T = 450 K is shown. The adsorption sites are indicated by green circles. Extra water molecules are removed for the sake of clarity. Co^{3+} (pink), Co^{2+} (green), O in Co_3O_4 (blue), O in water and 2-propanol (red), C (gray) and H (white).

6.2.2 Surface/Water Interaction

Proton Transfer

Figure 48 shows the O_s–H RDfs for the A-terminated and B-terminated systemps. Since in all six simulations the surface is exposed to water before adding the 2-propanol molecule, the surface hydroxylations are mainly due to proton transfers from water film to the surface oxygen.

For the A-terminated systems (Figure 48 (a)), the significant peak observed at a distance of 1 Å confirms the presence of surface hydroxyl groups. These groups form when the Co^{2+}–O–Co^{2+} bridge on the surface breaks due to water dissociation, resulting in the transfer of a proton to the surface oxygen atom. Under oxidative conditions, the

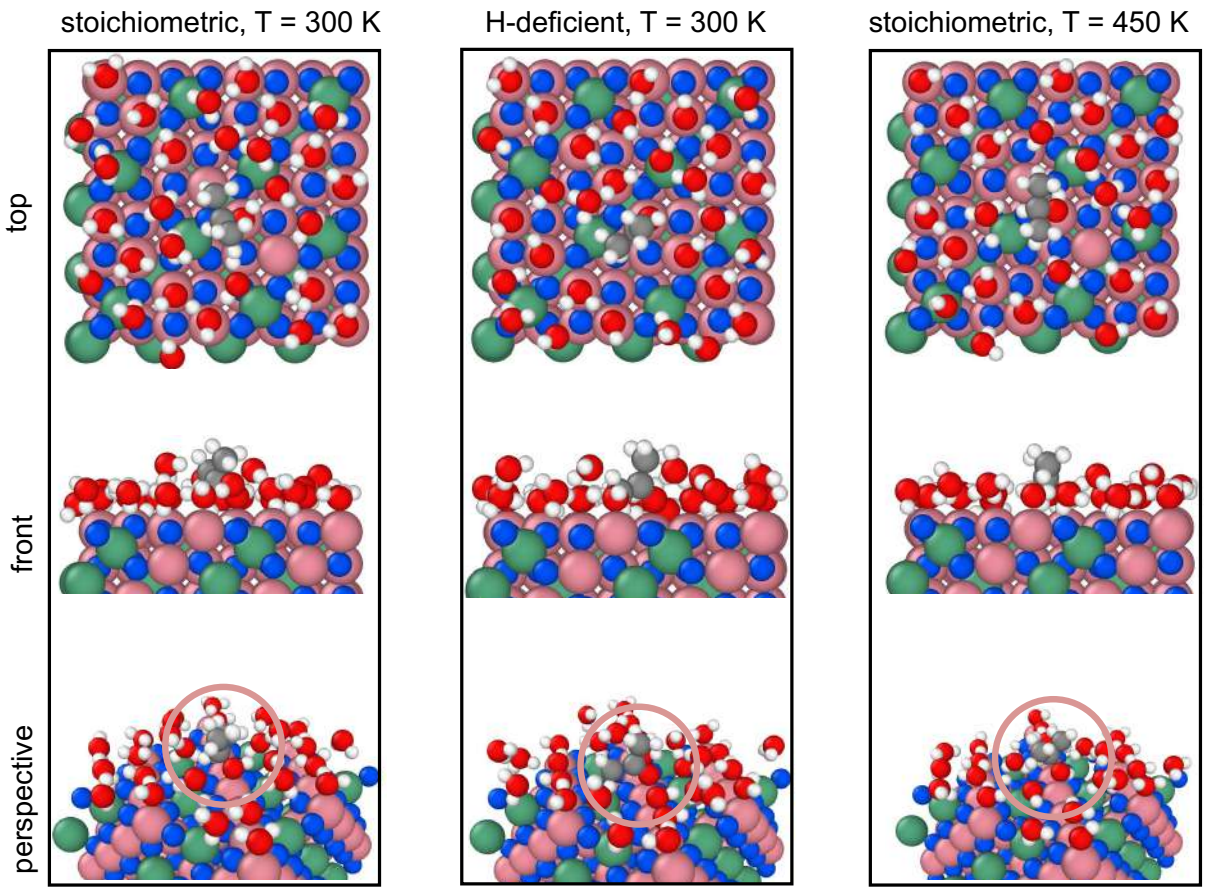

Figure 47: Snapshots of the final configurations of the AIMD simulations are depicted, showcasing the adsorption of 2-propanol at the B-terminated Co_3O_4 (001)/H_2O interface. The images present top, front, and perspective views. On the left, the stoichiometric reference system at 300 K is displayed, while the center image represents the H-deficient oxidative environment at 300 K. Additionally, the configuration in a stoichiometric environment at T = 450 K is shown. The adsorption sites are indicated by pink circles. Extra water molecules are removed for the sake of clarity. Co^{3+} (pink), Co^{2+} (green), O in Co_3O_4 (blue), O in water and 2-propanol (red), C (gray) and H (white).

first peak's height decreases notably, indicating a reduction in the number of hydrogen atoms within the adsorbed water film. Additionally, a smaller peak around 2.8 Å suggests a weak interaction between water and surface oxygen through hydrogen bonding.

The characteristic peak at 1 Å for the B-terminated system (Figure 48 (b)) confirms the the surface hydroxylation in the stoichiometric system at both 300 K and 450 K, but not in the H-deficient environment. In the H-deficient environment at 300 K, the peak is flattened, indicating the absence of surface hydroxylation. This occurs due to the removal of hydrogens from the water film, causing proton transfer from the weakly hydroxylated surface back to the water film, particularly to water hydroxyls that recombine to form molecular water. The broader peaks around 1.7 Å suggest the existence of relatively strong hydrogen bonds between the water films and the surface. Furthermore, the peaks around

2.6 Å indicate a weak interaction between water and surface oxygen through hydrogen bonding, which is stronger than in the A-terminated systems.

It can be also noted that the A-terminated surfaces exhibit about 5 times higher levels of hydroxylation compared to the B-terminated surfaces, as evident from the greater values for the first peaks.

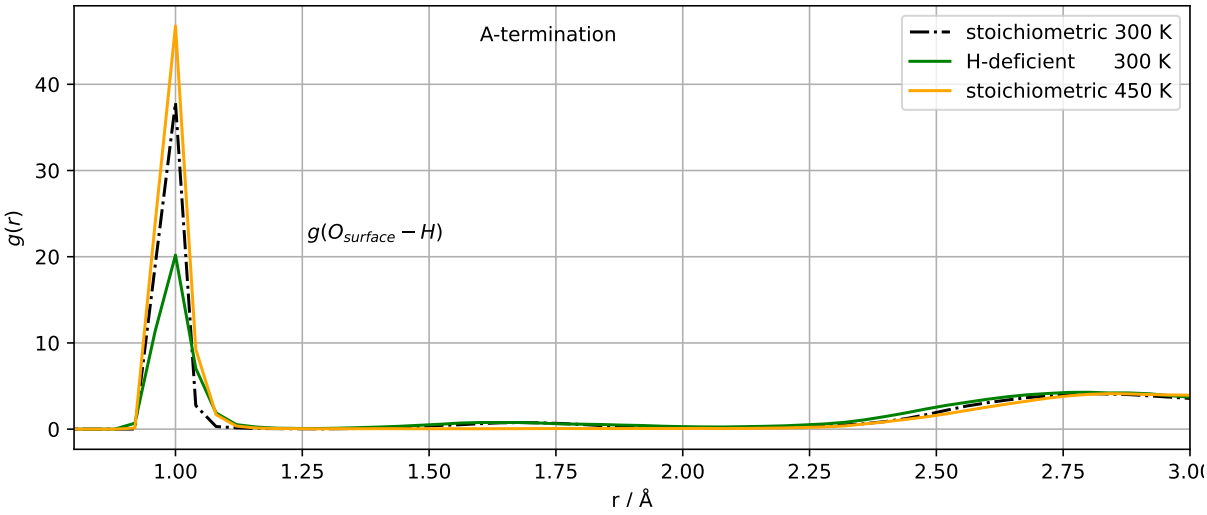

(a)

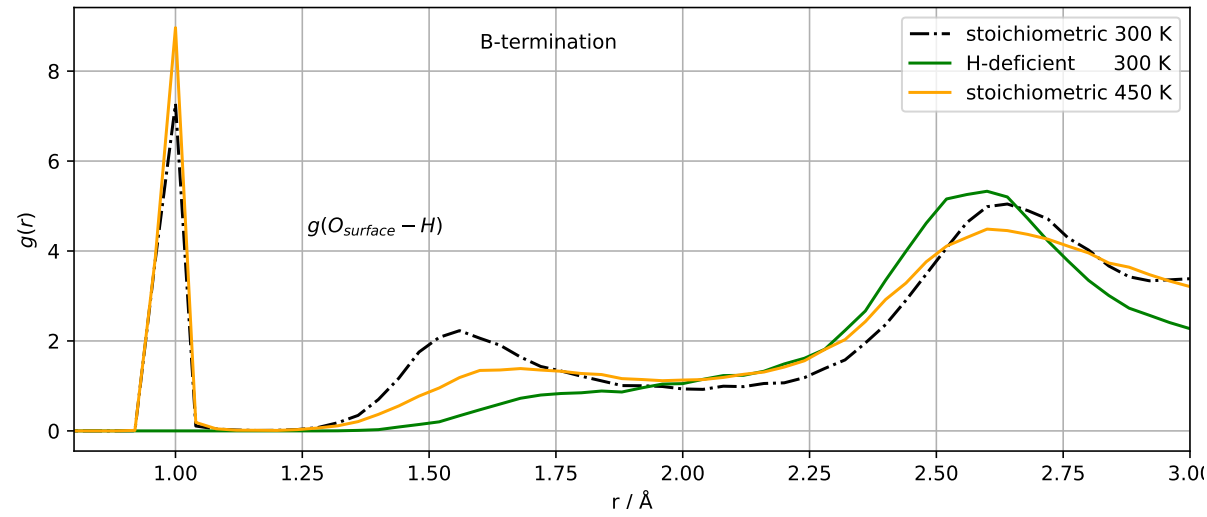

(b)

Figure 48: Distribution of distances between surface oxygen (O_s) and hydrogen: (a) A-terminated (001) surface (b) B-terminated (001) surface.

H_2O/OH^- Adsorption

The RDFs illustrating the distances between oxygen atoms of H_2O/OH^- adsorbates (referred to as O_w) are presented in Figure 49. These RDFs offer insights into the adsorption behavior of H_2O/OH^- species on both the Co^{2+} (A-terminated surface) and Co^{3+} (B-terminated surface) adsorption sites. The A-terminated and B-terminated systems exhibit comparable Co–O distances of approximately 2 Å. This similarity might imply

that the adsorbates are bonded with similar strengths on both surface terminations, irrespective of their different adsorption sites.

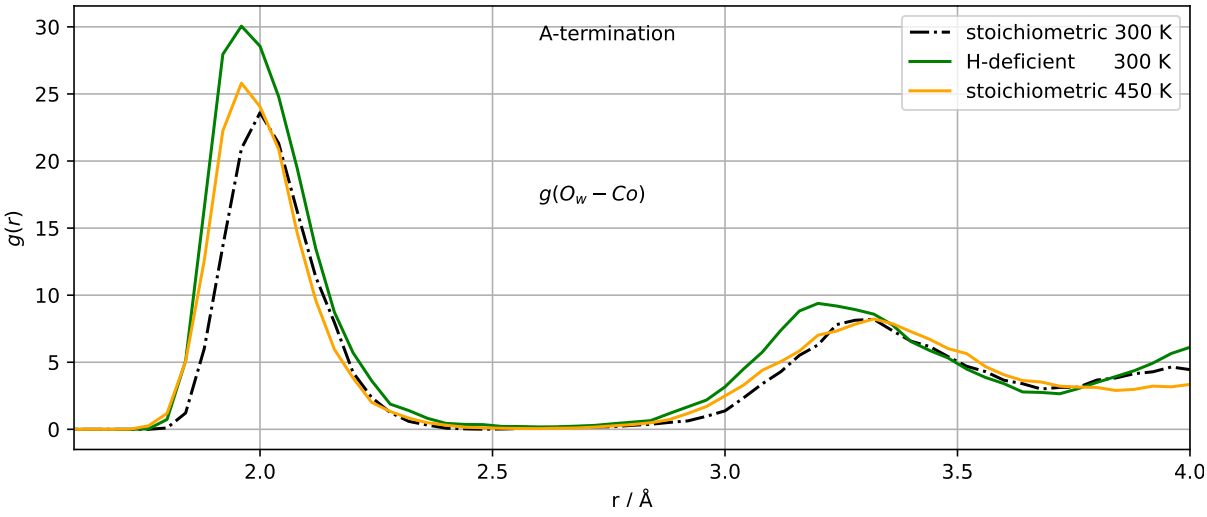

(a)

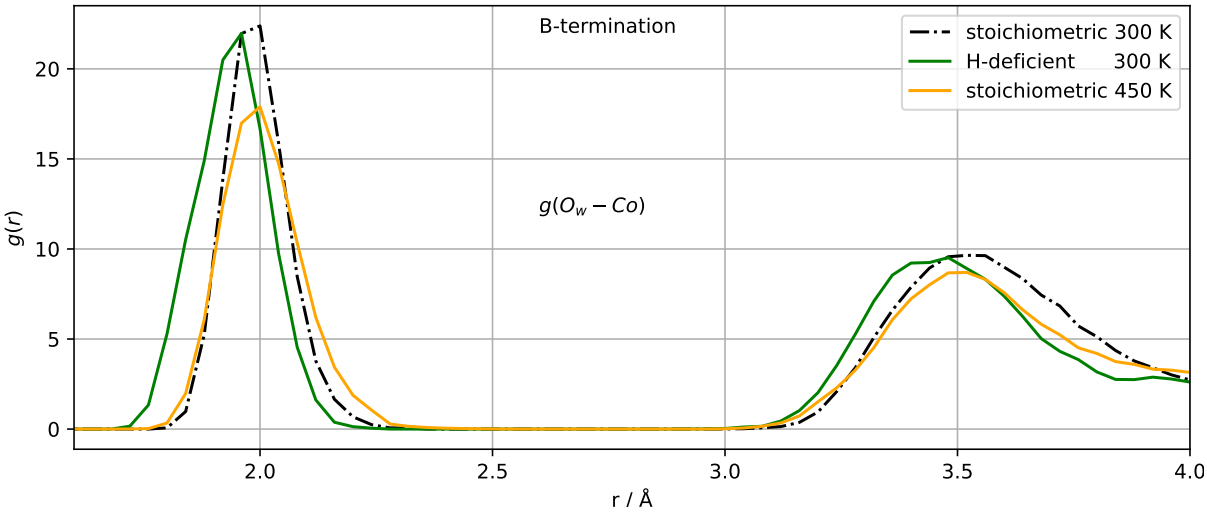

(b)

Figure 49: Distribution of distances between oxygen of H_2O/OH^- adsorbed species (O_w) to the closest cobalt ion: (a) A-terminated (001) surface (b) B-terminated (001) surface.

Furthermore, a comparison between the H-deficient systems (green curves) reveals a slight shift towards lower distances, indicating stronger adsorption of the species compared to the stoichiometric systems. This phenomenon can be attributed to the increased availability of OH^- groups in the H-deficient systems, which form stronger bonds with the adsorption sites in comparison to the water molecules. At higher temperatures (orange curves), the RDFs show a similar trend to that observed at 300 K (black curves), albeit with broader distributions. The increased width can be attributed to thermal fluctuations.

6.2.3 2-propanol Dynamics at the Interface

Evolution of O–H, C–H, C–O, and Co–O Distances

The time-dependent evolution of the O–H, C–H, C–O, and Co^{2+}–O distances of 2-propanol on the A-terminated surfaces is depicted in Figure 50. In the case of the stoichiometric reference system at 300 K (a), the O–H bond length oscillates between 2.8 Å and 3.8 Å, indicating 2-propanol deprotonation and recombination through proton exchange with the water film (supported by information from the O–H radial distribution functions in Figure 52 (a)). Under oxidative conditions and at a higher temperature (T = 450 K), as shown in Figure 50 (b) and (c), respectively, the recombination process is hindered, leading to 2-propanol decomposition and the formation of 2-propoxide. The other distances (C–H, C–O, and Co^{2+}–O) exhibit similar trends, weakly oscillating around average values throughout the simulation time. The average bond lengths for C–H, C–O, and Co^{2+}–O distances are approximately 1 Å, 1.5 Å, and 2 Å, respectively. This observation supports the finding that neither desorption nor further dehydrogenation of 2-propanol occurs.

Similar analyses are performed for the B-terminated systems (Figure 51). In the case of the stoichiometric system at 300 K (Figure 51 (a)), all distances oscillate around their equilibrated values throughout the 20 ps of the simulation, indicating that 2-propanol decomposition does not occur in the reference system. The average equilibrated distances for O–H, C–H, C–O, and Co^{3+}–O distances are approximately 1 Å, 1.1 Å, 1.5 Å, and 2 Å, respectively. Similar trends can be observed for the system at T = 450 K (Figure 51 (c)). However, in a H-deficient environment with 8 protons removed from the aqueous solution, 2-propanol decomposition is promoted, as is evident in Figure 51 (b). In fact, both O–H and C–H bond cleavages are observed early in the simulation, resulting in the formation of acetone. Consequently, the C–O bond (green curve) is contracted.

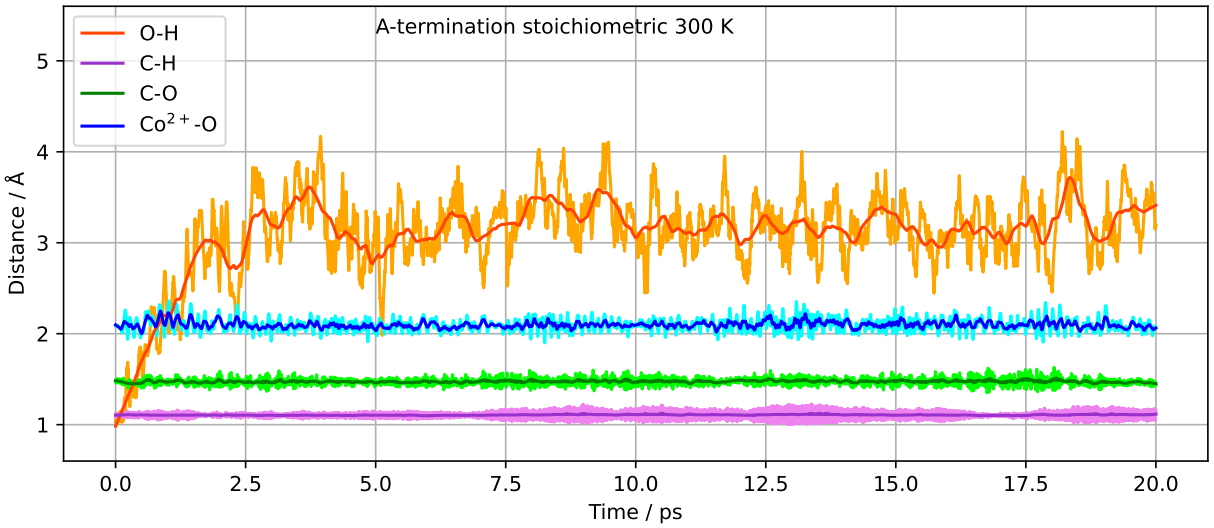

(a)

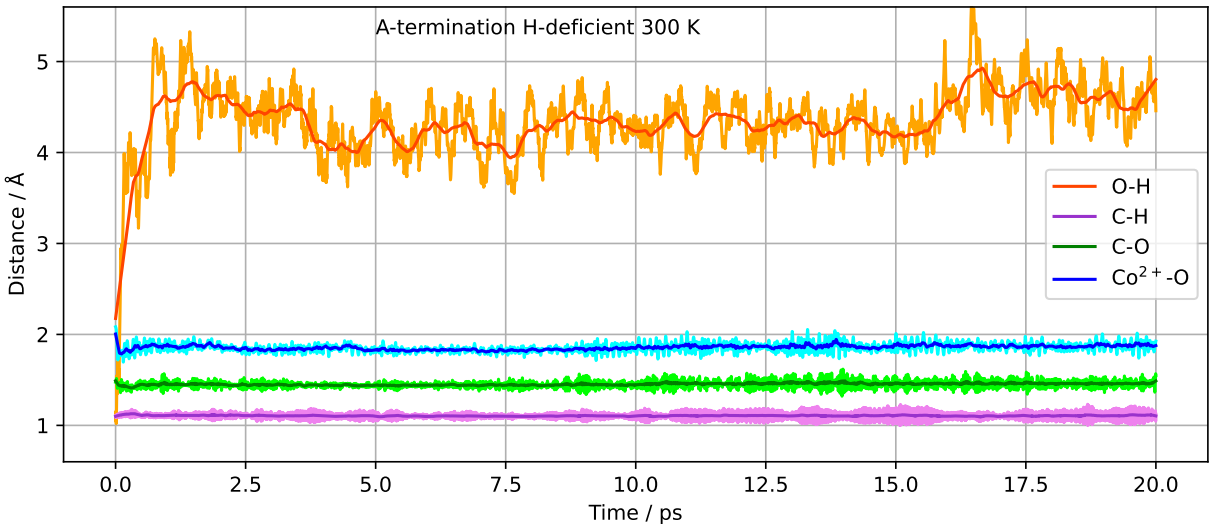

(b)

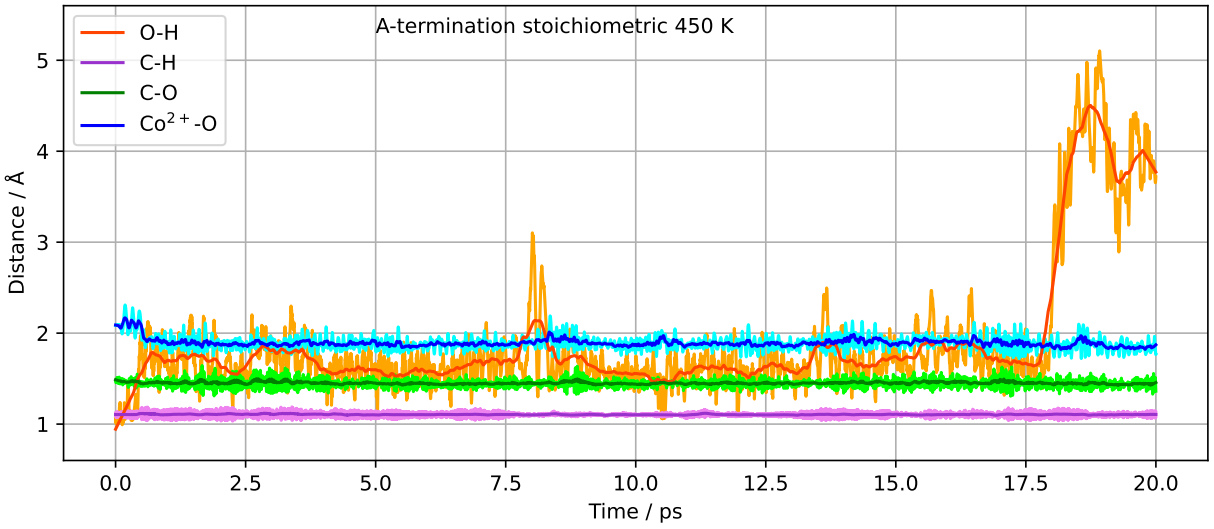

(c)

Figure 50: Evolution of O–H, C–H, C–O, and Co^{2+}–O distances during the AIMD simulations for the stoichiometric reference system at 300 K (a), in a hydrogen-deficient (oxidative) environment at 300 K (b), and in a stoichiometric environment at T = 450 K (c) for 2-propanol deprotonation at the A-terminated Co_3O_4 (001)/H_2O interface.

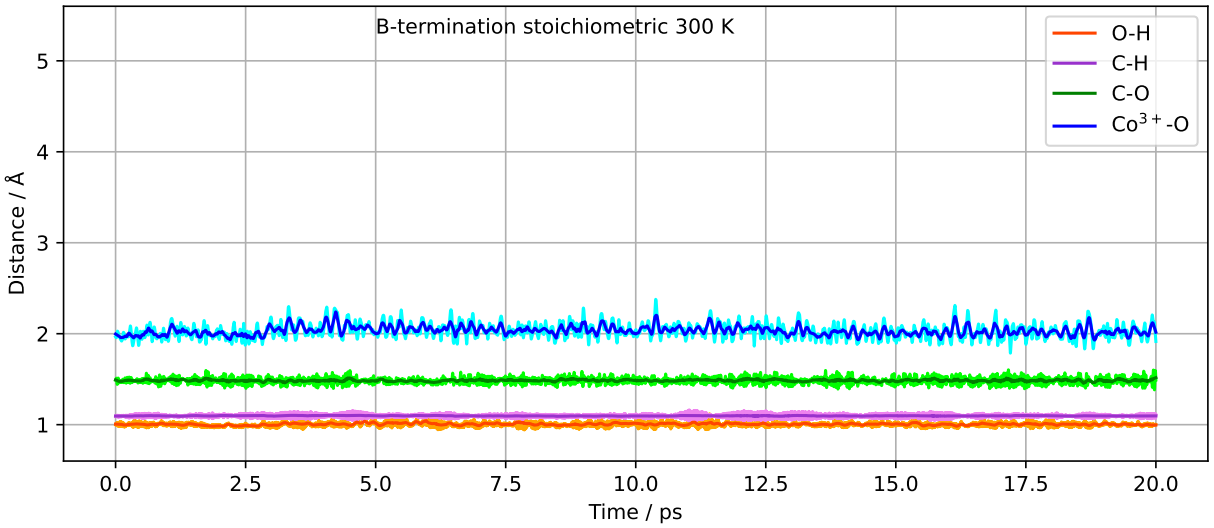

(a)

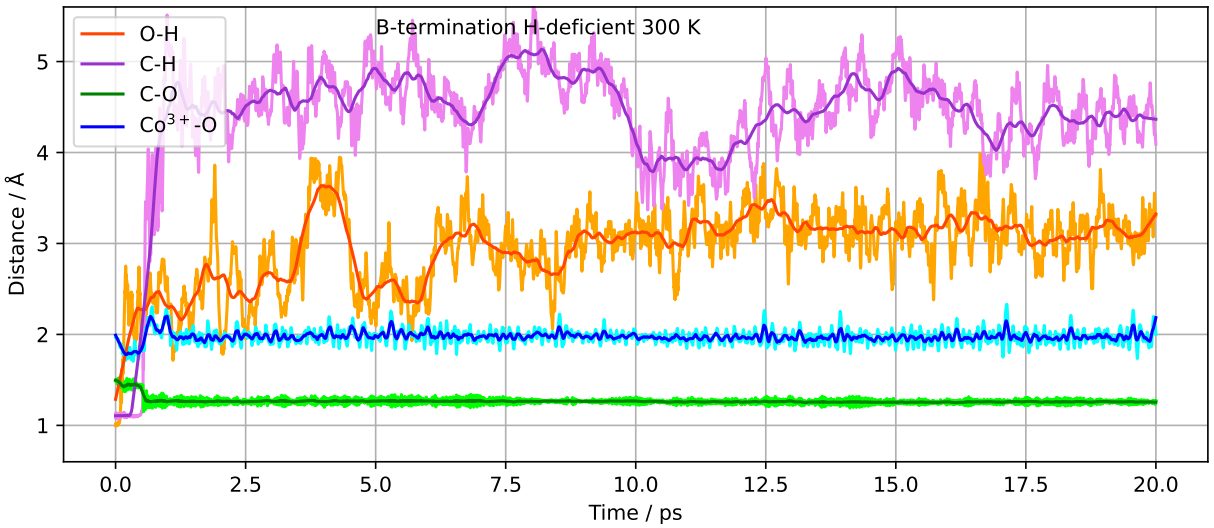

(b)

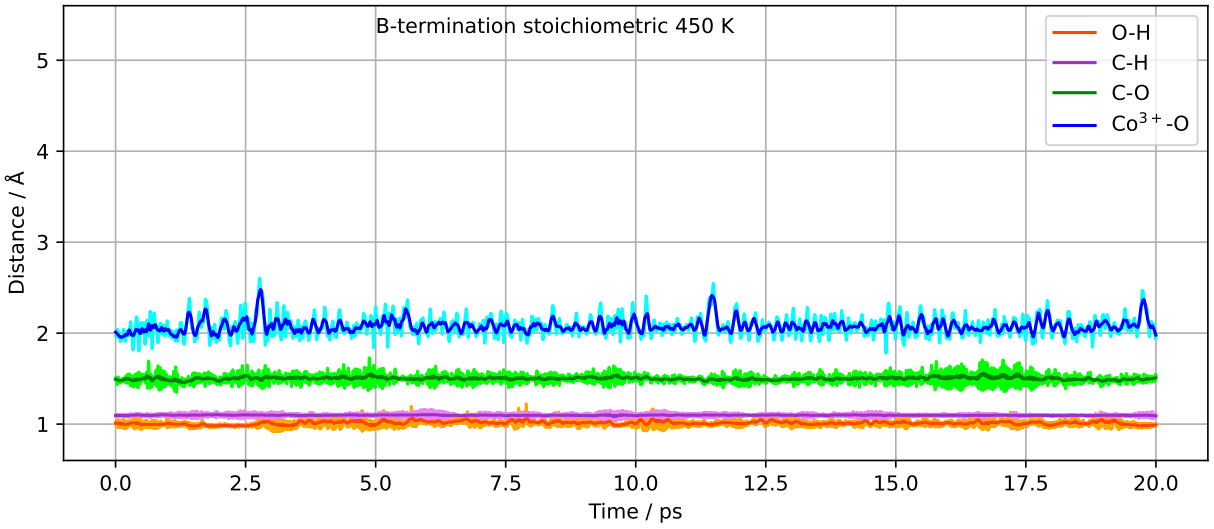

(c)

Figure 51: Evolution of O–H, C–H, C–O, and Co^{3+}–O distances during the AIMD simulations for the stoichiometric reference system at 300 K (a), in a hydrogen-deficient (oxidative) environment at 300 K (b), and in a stoichiometric environment at T = 450 K (c) for 2-propanol deprotonation at the B-terminated Co_3O_4 (001)/H_2O interface.

O–H bond

Analysis, as shown in Figure 50, while displaying the time dependence of specific distances over time, is unable to directly differentiate between proton abstraction and proton exchanges. However, such information can be provided by the O–H radial distribution functions.

In Figure 52 (a), the $O_{alcohol}$–H distances in different environments of the A-terminated surfaces are compared. The RDF for the stoichiometric reference system (black curve) at 300 K exhibits a peak at 1 Å, indicating an intramolecular $O_{alcohol}$–H bond. This supports the deprotonation of 2-propanol and subsequent recombination via proton exchange with the water film, as mentioned earlier. On the other hand, both the H-deficient system (blue curve) and the system at 450 K (red curve) have zero probability at the 1 Å distance, indicating hydrogen abstraction and formation of 2-propoxide in both cases. At distances around 1.7 Å, these systems have a higher probability compared to the reference system, indicating that the hydrogen from the C2–H bond is closer to the oxygen of the 2-propoxide molecule.

The RDFs of the B-terminated surfaces (Figure 52 (b)) for the stoichiometric system at 300 K (black) and 450 K (red) exhibit similar behavior near the 1 Å distance, indicating that unlike on the A-terminated systems, temperature does not promote the decomposition of 2-propanol into 2-propoxide. However, around the 1.7 Å distance, the system at 450 K shows a higher probability compared to the 300 K system, suggesting that increasing the temperature brings the H from the C2–H bond closer to the oxygen of 2-propanol. In a H-deficient environment at 300 K (blue), the peak at 1 Å disappears, providing clear evidence of 2-propanol deprotonation in this system. The peak around 2 Å for the H-deficient system is also flattened, suggesting that the hydrogen of the C2–H bond is not in the vicinity of $O_{alcohol}$, indicating partial oxidation of 2-propanol.

C–O bond

The length of the C–O distance provides insights into whether the initial 2-propanol molecule is converted into 2-propoxide or acetone, or remains unchanged. Figure 53 illustrates the distribution of C–O distances, shedding light on these transformations.

In Figure 53 (a), corresponding to the A-terminated systems, perturbations the electrochemical environment (blue curve) or temperature (red curve) result in a shift of the curve towards the lower region between the 1.4 Å and 1.5 Å distances. This shift indicates that the C2–O bond in 2-propoxide is slightly stronger than the C2–O bond in 2-propanol. More importantly, Figure 53 (b) demonstrates that the C2–O bond in acetone (blue curve) is significantly stronger than both 2-propanol and 2-propoxide, suggesting the formation of a double bond between C2 and O (i.e., C=O).

The second peaks in the RDFs, located around the 2.4 Å distance, correspond to the C1–O and C3–O distances. Notably, the second peak is shorter for the H-deficient system

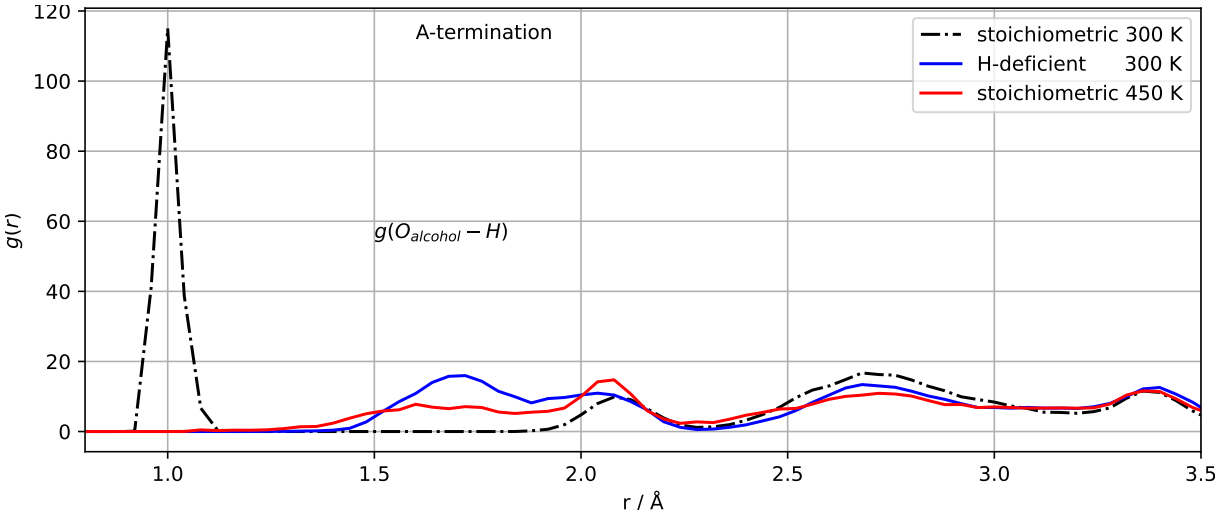

(a)

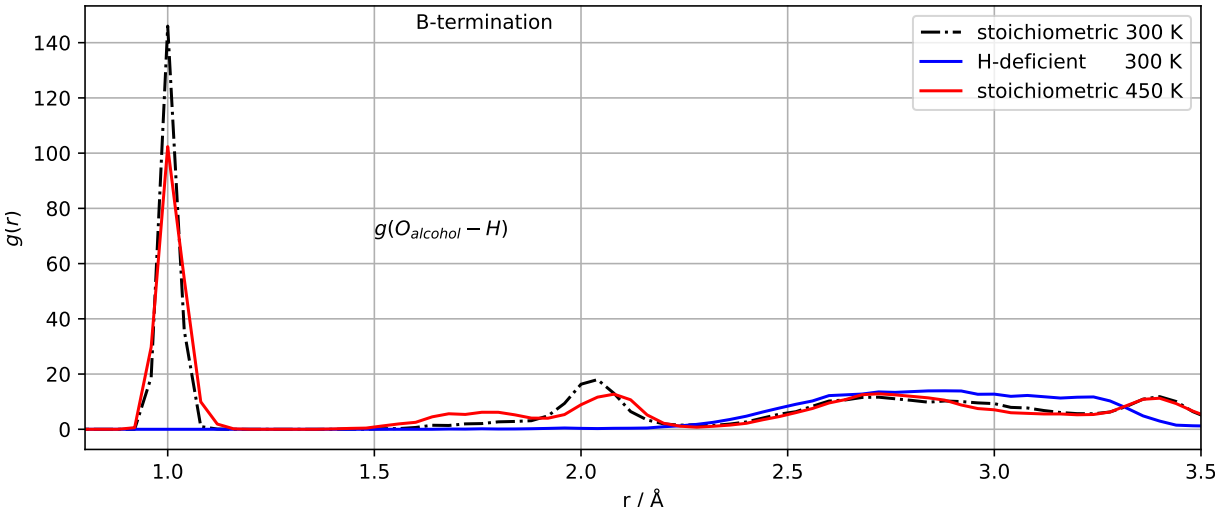

(b)

Figure 52: Radial distribution function of $O_{alcohol}$ and all H: (a) A-terminated Co_3O_4 (001) surfaces, and (b) B-terminated Co_3O_4 (001) surfaces.

(blue curve in Figure 53 (b)), indicating that even the C1–O and C3–O distances are shorter in acetone compared to both 2-propanol and 2-propoxide molecules.

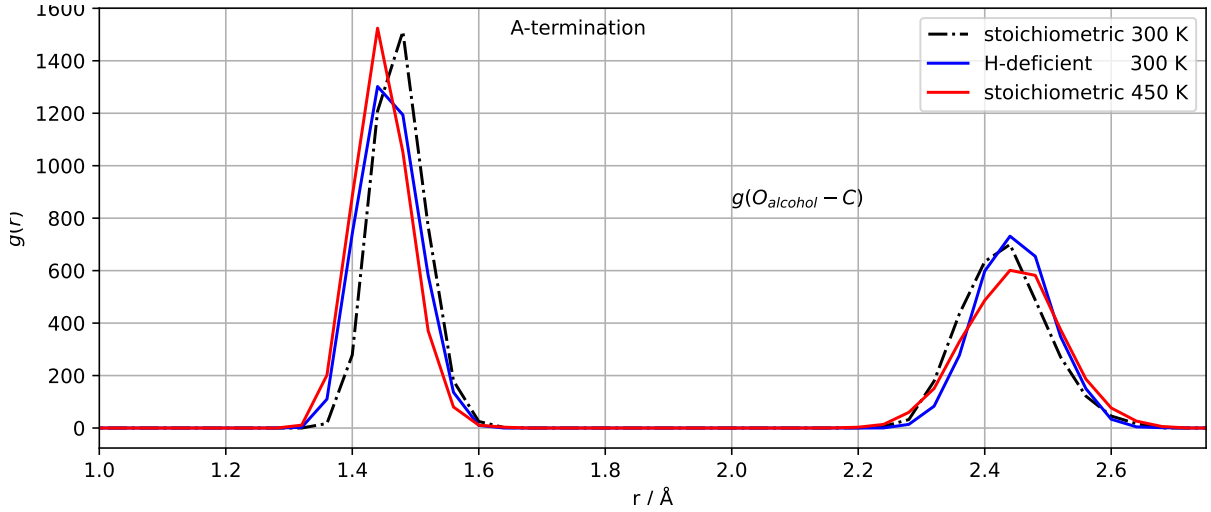

(a)

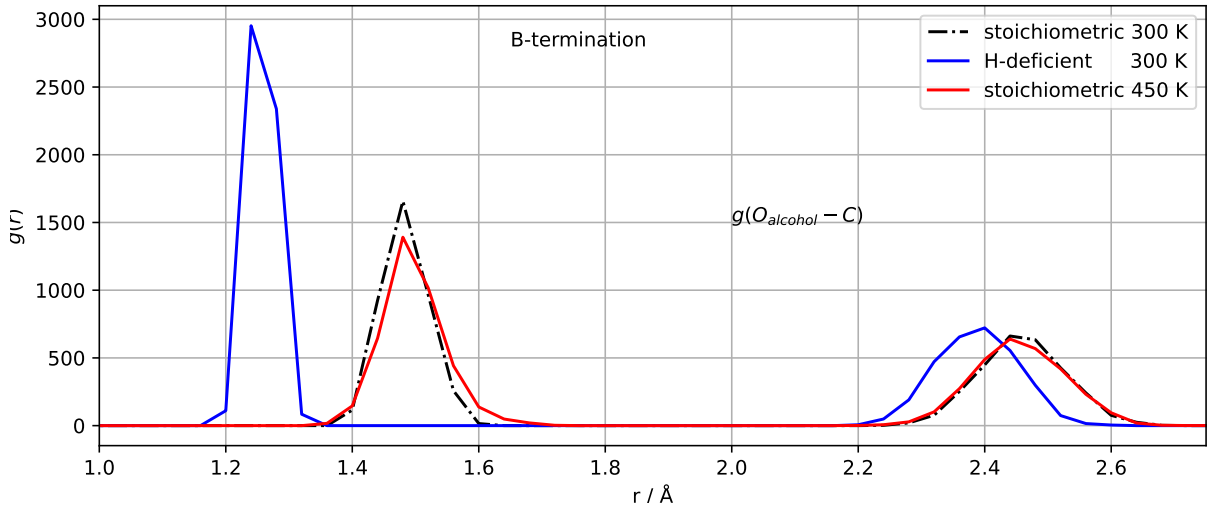

(b)

Figure 53: Radial distribution function of $O_{alcohol}$ and all C: (a) A-terminated Co_3O_4 (001) surfaces, and (b) B-terminated Co_3O_4 (001) surfaces.

6.2.4 Adsorption Geometry

The time evolution of distance between the alcoholic oxygen and its Co adsorption site (curve Co^{3+}-O in Figure 51 (b) provides a hint that the distance between acetone and Co is somewhat shorter, and thus probably stronger, than the bond between 2-propanol and Co (Figure 51 (a) and (c)), as is visible from the slight reduction of the distance in the time interval from about 0.1 to 0.5 ps.

Figure 54 compares the simulation-averaged distribution function, denoted as $g(O_{alcohol}-Co)$, for the shortest distance between the alcoholic (2-propanol, 2-propoxide, or acetone) oxygen and its Co adsorption sites across all simulations. As previously shown, 2-propanol undergoes dehydrogenation on the A-terminated surface in stoichiometric systems at elevated temperatures and in hydrogen-deficient environments even at room temperature. This deprotonation process results in shorter and potentially stronger bonds, as indicated

by the shift towards smaller values in the distribution functions for the elevated temperature run (red) and the H-deficient system (blue) compared to the room temperature reference (black).

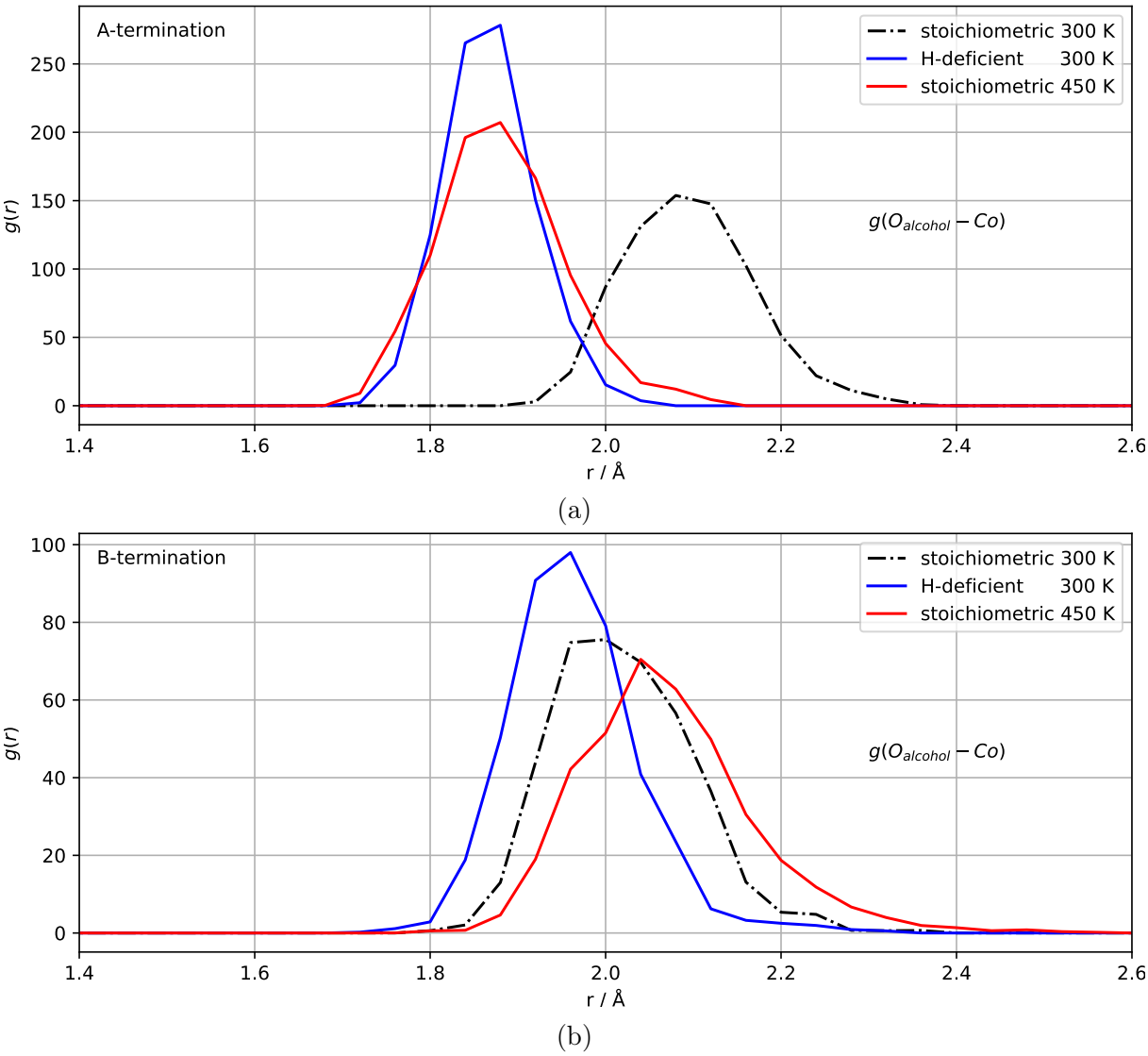

Figure 54: Distribution of distances between alcohol oxygen and closest cobalt ion: (a) A-terminated Co_3O_4 (001) surfaces, and (b) B-terminated Co_3O_4 (001) surfaces.

On the B-terminated surface (Figure 54 (b)), the behavior is different. The 2-propanol molecule does not undergo chemical transformations at high temperatures, leading to only a small shift in the distance distribution towards larger values, likely due to increased thermal fluctuations. In contrast, the formation of acetone in the hydrogen-deficient system is accompanied by slight shifts towards smaller distances. This downward shift in the distance distribution can be attributed to reduced steric requirements in the absence of two hydrogen atoms, although there is no indication that acetone forms a stronger bond with the Co^{3+} adsorption site. Overall, the differences in the distribution of pristine uncharged 2-propanol relative to its corresponding base 2-propoxide (Figure 54 (a)) are

more pronounced than the differences between the neutral alcohol 2-propanol and the ketone acetone (Figure 54 (b)).

Another aspect of the adsorbate geometry is depicted in Figure 55, which shows the distribution of the angle θ between the surface normal and the intramolecular $O_{alcohol} - C$ vector. An angle of 0° indicates that the OC bond is parallel to the surface normal, suggesting vertical adsorption of the 2-propanol molecule on the (001) surface. Conversely, an angle of 90° indicates that the OC vector lies parallel to the surface plane.

Figure 55 (b) illustrates the distribution of the $OC - Z$ angle for the A-terminated surfaces. In the reference system, this angle ranges from 35° to 75°, with the highest probability occurring around 50°. Increasing the temperature to 450 K broadens the range of possible orientations to 20°-75° (upon formation of the 2-propionate base), with the maximum probability between 40° and 50°. The H-deficient system at 300 K exhibits slightly higher angle ranges compared to the reference system. In all cases, the OC vector points away from the surface plane and is never directed towards the surface, as all angles are at least 15° lower than 90°.

Figure 55 (c) demonstrates the distribution of the $OC - Z$ angle for the B-terminated (001) surfaces. The reference system shows an angle range of 35°-65°, with the highest probability occurring around 50°, slightly lower than that of the A-terminated (001) surface. Increasing the temperature to 450 K broadens the range to 35°-75° (attributable to increasing thermal disorder), with the maximum probability around 60°. The angle ranges for the H-deficient system at 300 K are slightly lower than those of the reference system. As with the A-terminated systems, the OC vector always points away from the surface plane, with all angles being at least 20° lower than 90°.

Overall, both A-terminated and B-terminated systems exhibit adsorption of 2-propanol at an approximate angle of 50°. Furthermore, when compared to the highly concentrated regime in the previous section (Figure 35), it can be concluded that there is limited variation in 2-propanol adsorption orientation under various conditions, concentrations, and surface terminations. The adsorption angle remains around 50°±10°. These observations align with the vSFG experimental findings mentioned in the previous chapter.[80]

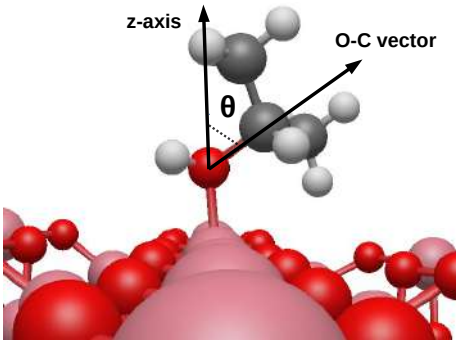

(a)

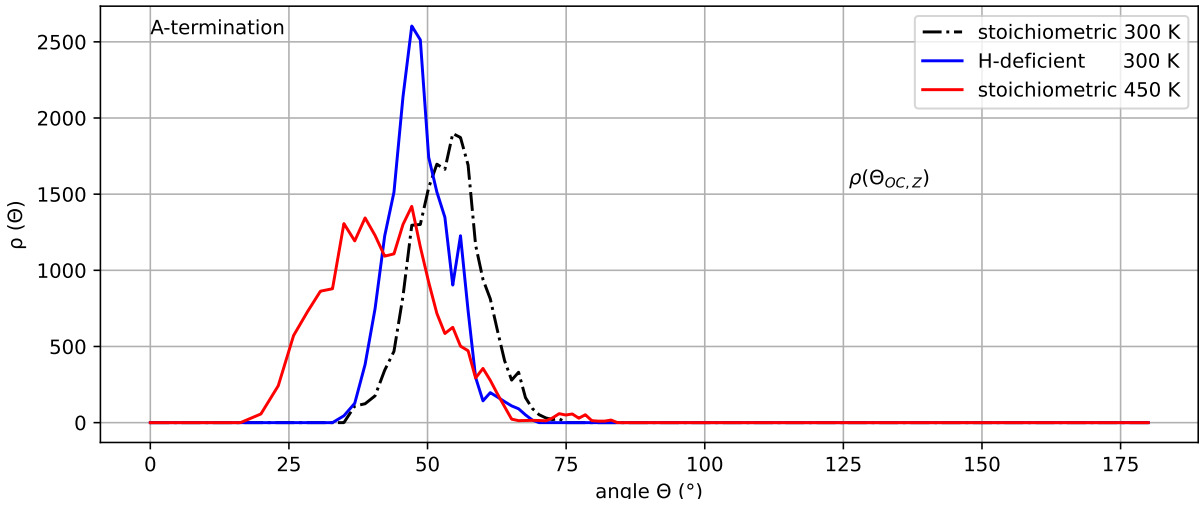

(b)

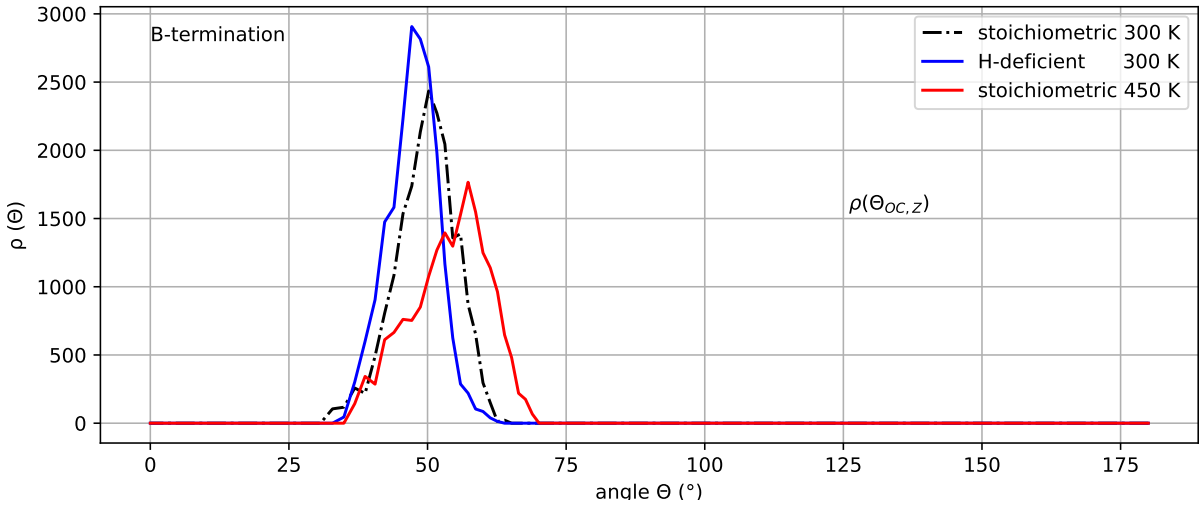

(c)

Figure 55: Distribution of angle between $O_{alcohol}$-C2 vector and surface normal Z (001) axis: (a) schematic representation of the angle, (b) the distribution for the A-terminated Co_3O_4 (001) surfaces, and (c) the distribution for the B-terminated Co_3O_4 (001) surfaces.

6.2.5 Reaction Mechanism: 2-propanol Activation and Oxidation

2-propanol Activation (on A-terminated surface)

It was shown in Figure 50 that on the A-terminated surfaces, either in H-deficient environment or at 450 K, 2-propanol dissociation occurs. To further illustrate this, Figure 56 presents the two stages of 2-propanol deprotonation for the stoichiometric system at 450 K (as shown in Figure 50 (c)). The hydroxylation of the surface is evident in Figure 56, with hydroxyl groups being transferred from the water film to the surface oxygen (since the initial system consisted of 60 water molecules without any electrochemical perturbation). One such dissociated water molecule (producing OH^- and H^+) approaches the vicinity of the 2-propanol molecule (Figure 56 (a)). This OH^-, abstracts the hydroxyl hydrogen (green) from 2-propanol, resulting in the formation of a 2-propoxide molecule and a water molecule (Figure 56 (b)). The resulting 2-propoxide molecule remains adsorbed on the same Co^{2+} site.

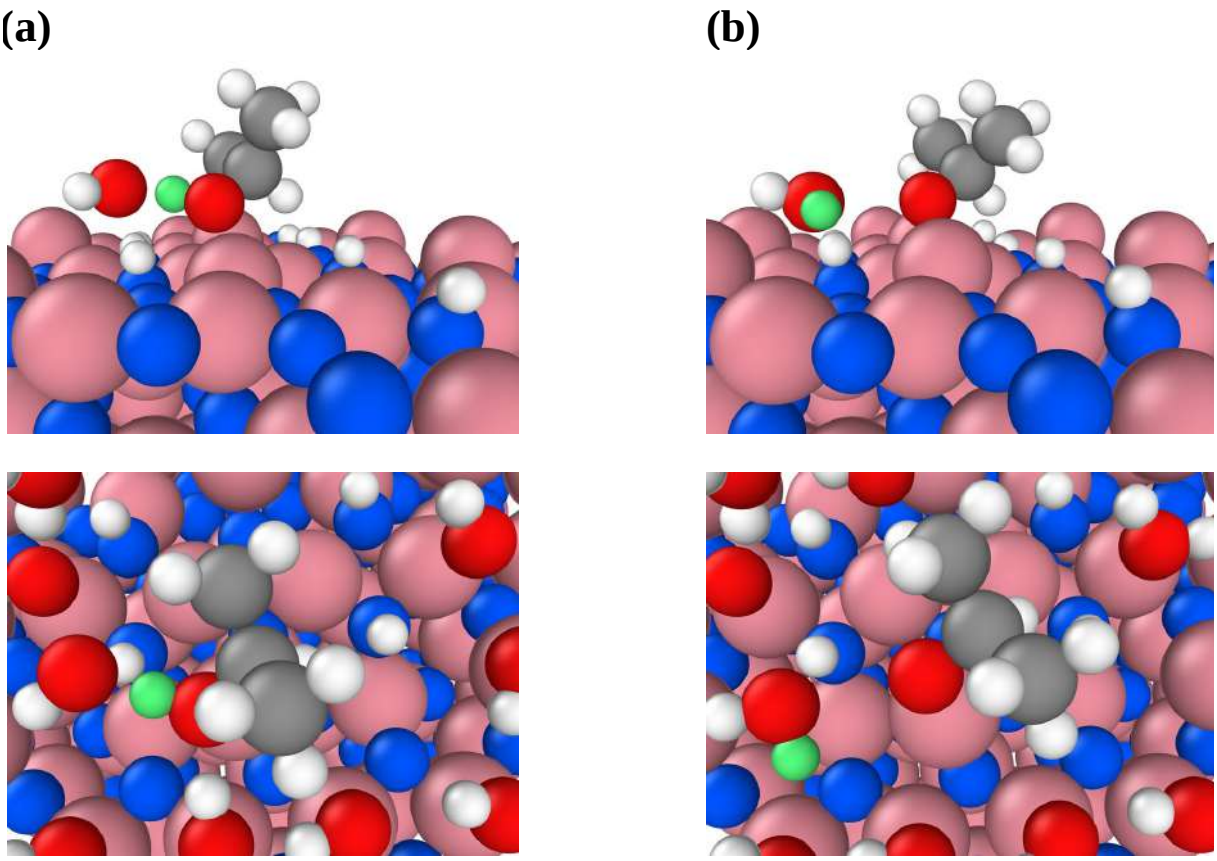

Figure 56: Snapshots of the A-terminated (001) surface at 450 K (top and perspective views) before (a) and after (b) 2-propanol deprotonation. Co^{3+} (pink), Co^{2+} (green), O in Co_3O_4 (blue), O in water and 2-propanol (red), C (gray), H in hydoroxyl hydrogen (green), and other H (white). Extra water are removed for clarity.

2-propanol Oxidation (on B-terminated surface)

In the previous section, it was demonstrated that out of the six different simulation systems (three different cases of A-terminated (001) surface and three different cases of B-terminated (001) surface), only one exhibited the partial oxidation of 2-propanol and the formation of acetone.

Figure 57 provides a view of the first 0.5 ps of the B-terminated H-deficient system (Figure 51 (b)), capturing the deprotonation and dehydrogenation process. The four stages of the 2-propanol partial oxidation reaction can be summarized as follows (see Figure 58):

1. The 2-propanol molecule is adsorbed molecularly on a Co^{3+} adsorption site via a Co^{3+}–O bond (Figure 58 (a)).

2. The hydroxyl hydrogen (from 2-propanol) is abstracted by a neighbor OH^- group present in the water film. This leads to the formation of an adsorbed 2-propoxide intermediate and water (Figure 58 (b)).

3. After about 400 fs, C–H bond cleavage and proton transfer to another neighboring OH^- groups takes place (Figure 58 (c)).

4. The formation of an acetone molecule adsorbed on the same Co^{3+} site and molecular water present in the surrounding environment occurs (Figure 58 (d)).

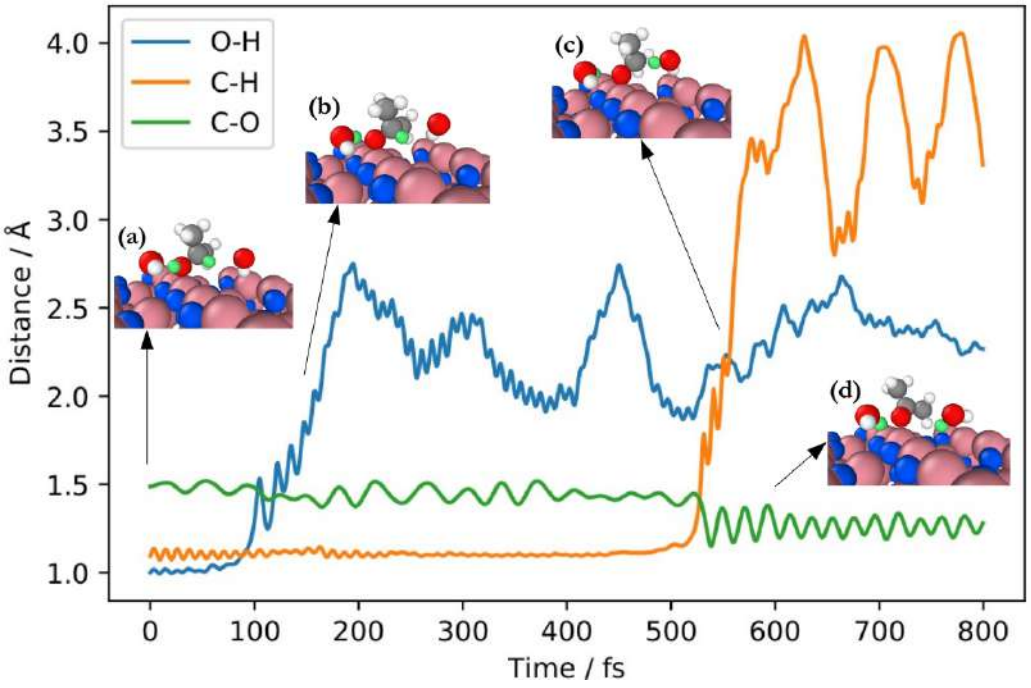

Figure 57: The first 0.5 ps time evolution of the B-terminated H-deficient system at 300 K (see Figure 51 (b)) in which the partial oxidation of 2-propanol takes place.

The fact that the Co^{3+} adsorption site remains the same during the 2-propanol oxidation reaction during the whole simulation time is in line with the recent experimental reports[6,7,32] showing that the Co^{3+} sites to be the *stable* adsorption sites during the 2-propanol oxidation.

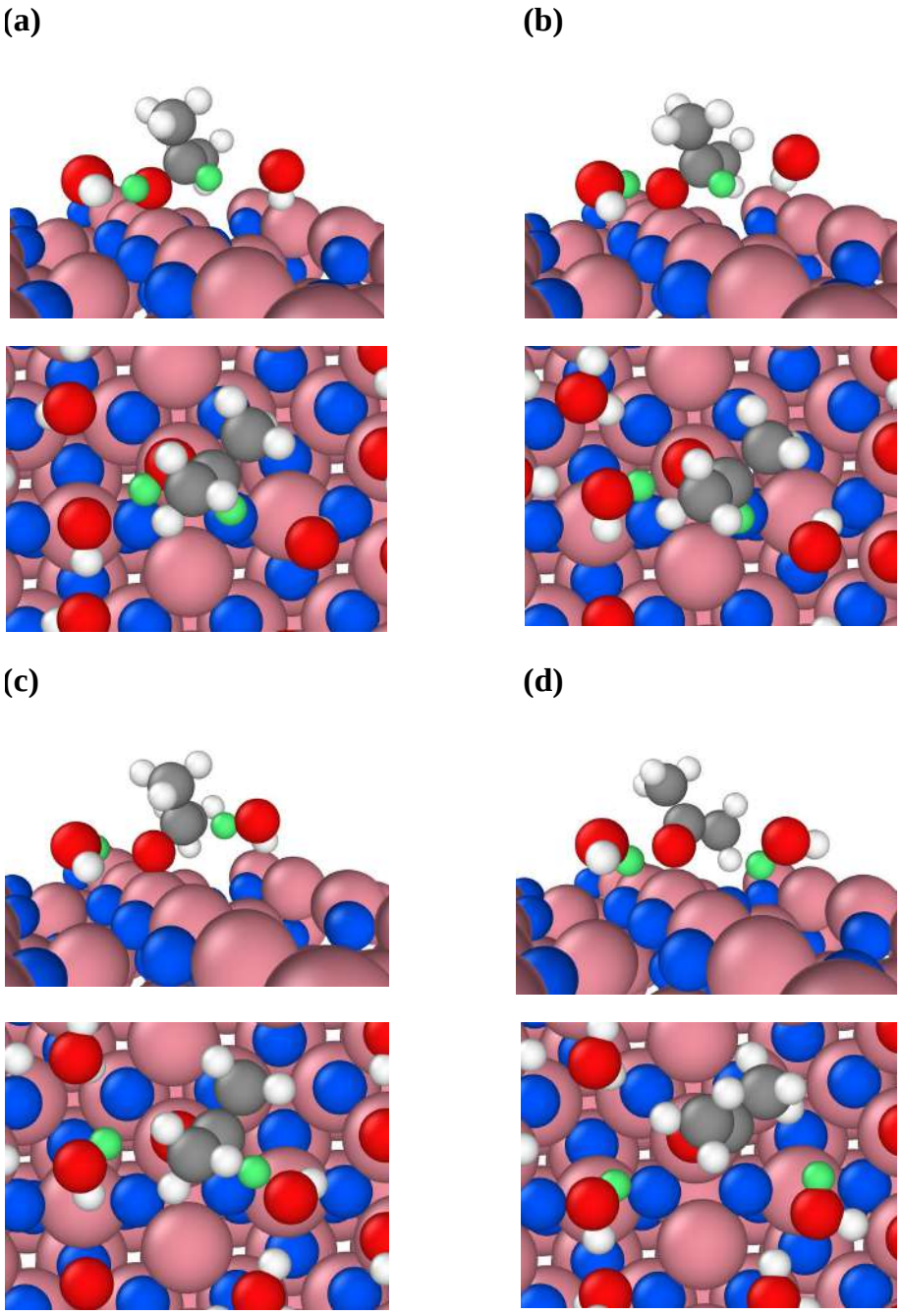

Figure 58: Snapshots of the four stages of 2-propanol partial oxidation reaction on the B-terminated H-deficient system at 300 K (top view and perspective view). Co^{3+} (pink), Co^{2+} (green), O in Co_3O_4 (blue), O in water and 2-propanol (red), C (gray), H in 2-propanol hydroxyl and CH group (green), and other H (white). Extra water are removed for clarity.

Figure 59 presents the charge density difference (CDD) observed at the oxidation steps of 2-propanol on the B-terminated Co_3O_4 (001) surface. The CDDs were computed based on equilibrium trajectories obtained from the snapshots shown in Figure 58. Specifically, the figure displays the calculated CDDs for four specific states along the oxidation pathway to acetone, labeled (a) through (d) in Figure 58.

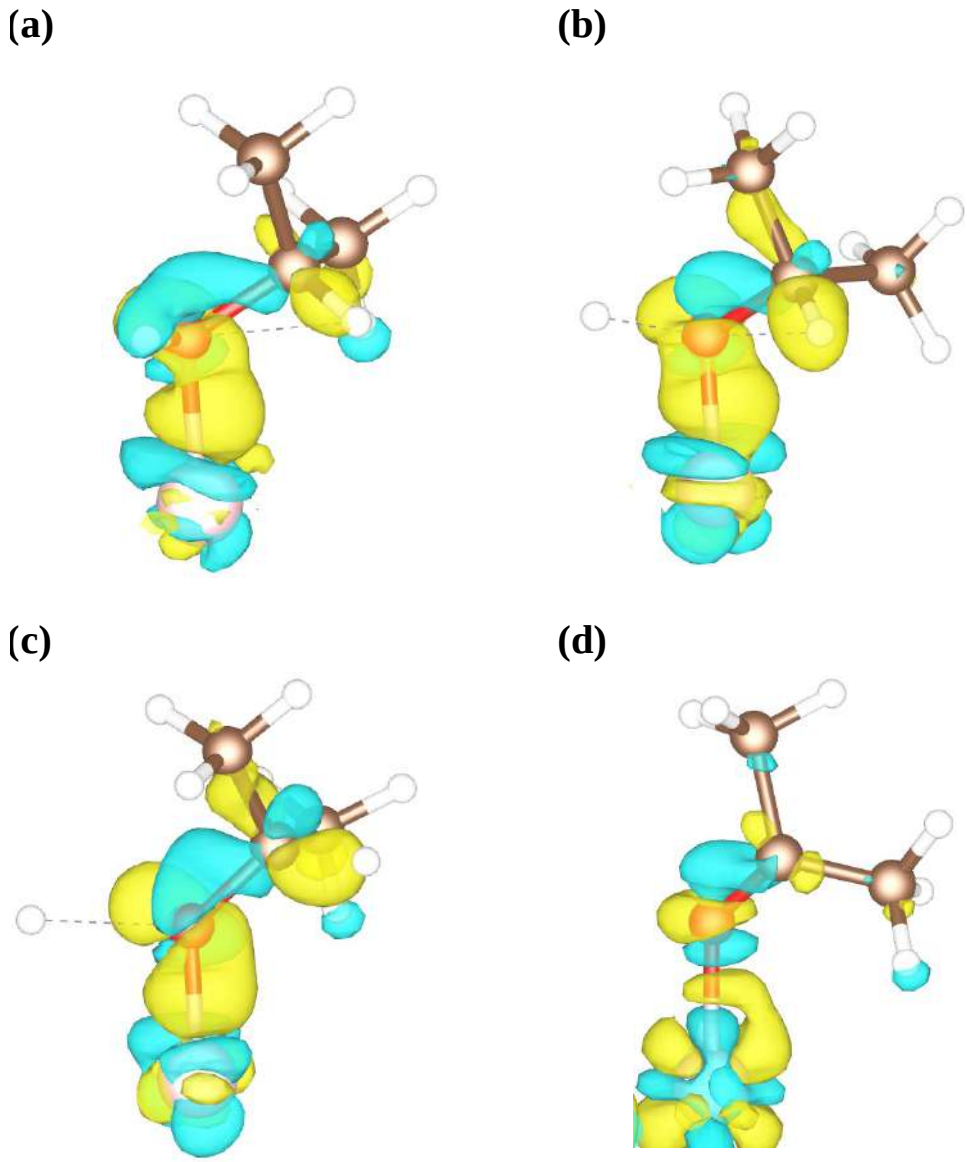

Figure 59: Charge density difference of adsorbed 2-propanol molecule on the Co^{3+} site through the simulation time for H-deficient environment at 300 K: (a), (b), (c) and (d) correspond to the same snapshots from Figure 58. The iso-surfaces are drawn at the – 0.003 (cyan) and + 0.003 (yellow) e $Å^{-3}$ density levels. The yellow regions indicate the accumulation of electron density, while the cyan regions indicate the depletion of electron density.

To compute the CDD, the electron densities of the substrate (Co_3O_4 slab) and the adsorbates (water + 2-propanol) were subtracted from the total electron density of the

compound system. In Figure 59, our focus is on the 2-propanol molecule, so the remaining differences that reflect the bonding of water and hydroxy groups with the oxide surface have been removed.

In this figure, yellow regions indicate the accumulation of (negative) charge, while cyan regions indicate local reduction of electron density. State (a) shows that initially, upon adsorption of 2-propanol, the electron density is shifted from the Co^{3+} binding site and the O–C bond towards the formation of a Co^{3+}–O bond.

During the acidic proton transfer, which breaks the O–H bond (b), and the subsequent oxidative hydrogen bond transfer, which breaks the C–H bond (c), the charge accumulation between oxygen and Co^{3+} remains largely intact. Once the oxidation to acetone is complete (d), the charge accumulation between oxygen and the cobalt ion is reduced, indicating weaker interactions despite the small overall shift of the distance distribution towards smaller values shown in Figure 54.

6.2.6 A-terminated vs. B-terminated (001) Surfaces for 2-propanol Oxidation

One question that naturally arises is why the oxidative reaction occurs exclusively on the B-terminated surface and not on the A-terminated surface. This observation is particularly intriguing considering previous research[64] indicating that the A-terminated surface of Co_3O_4 (001)/H_2O interface is significantly more reactive than the B-terminated surface. For instance, it has been demonstrated that when the Co_3O_4 (001) surface is fully covered by water, approximately 16 water dissociations take place on the surface, whereas the degree of hydroxylation for the B-terminated surface is less than 5 dissociations.[64]

To address this question, it is crucial to examine the specific details of the interface on the B-terminated surface, as depicted in Figure 60. This figure shows different views (top, front, left, and perspective) of the Co_3O_4 (001)/H_2O/2-propanol interface for the H-deficient B-terminated system at 300 K (refer to Figure 47 (b) and Figure 51 (b)). From a side view, it is evident that an epitaxial water layer forms on the Co_3O_4 (001) surface, which is absent on the A-terminated (001) surface. By considering all the oxygen atoms of the adsorbed species (i.e., 2-propanol, H_2O, or OH^-), trajectory lines are depicted (in green) for these atoms during the 20 ps of AIMD simulation (as shown below).

Figure 60 reveals two significant observations: (1) there are two types of H_2O/OH^- species present on the surface: those that are strongly adsorbed on the Co^{3+} adsorption sites, exhibiting lower mobility, and those that are weakly bound to the surface, demonstrating higher mobility; and (2) both deprotonation and dehydrogenation occur due to the approach of two OH^- groups in the water film to the 2-propanol molecule. Consequently, it can be deduced that the "mobile OH^- groups in the epitaxial water film" are responsible for the partial oxidation of 2-propanol, and such OH^- groups are exclusively present on the B-terminated (001) surface.

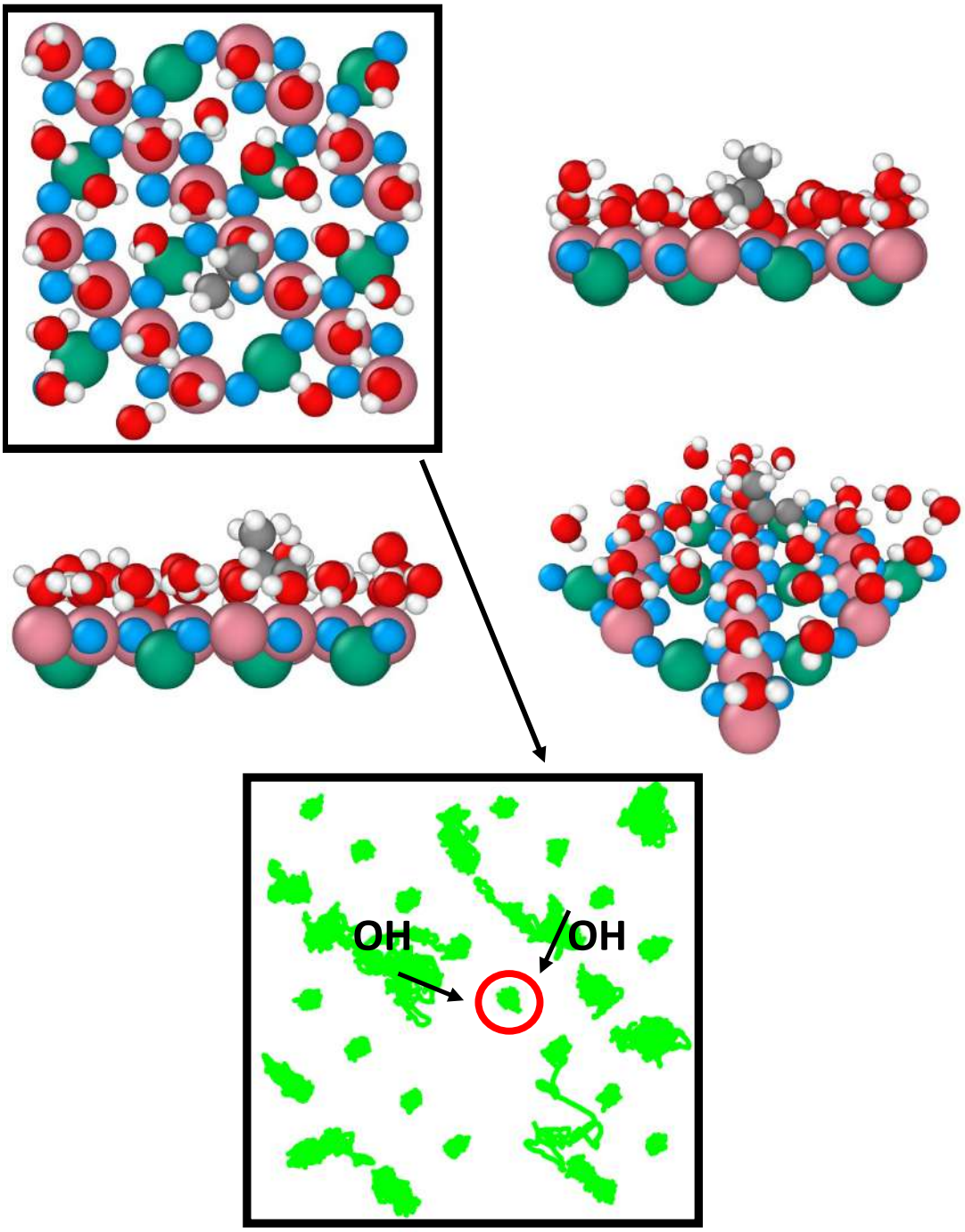

Figure 60: Different views (top, front, left, and perspective) of the Co_3O_4 (001)/H_2O/2-propanol interface for the H-deficient B-terminated system at 300 K (refer to Figure 47 (b) and Figure 51 (b)). Trajectory lines (green) depict the movement of the oxygen atoms of all adsorbed species. The oxygen atom of the 2-propanol molecule is represented by a red circle. Two OH^- groups approach the 2-propanol, abstracting both hydrogens from the 2-propanol molecule. Color scheme: Co^{3+} (pink), Co^{2+} (green), oxygen in Co_3O_4 (blue), oxygen in water and 2-propanol (red), carbon (gray), and hydrogen (white).

6.2.7 Further Discussion

In summary, this section investigated the possible oxidative transformations of an isolated 2-propanol molecule embedded in a water layer on a Co_3O_4 (001) surface. Simulations were performed for both the A-terminated surface (with a mixture of Co^{2+}/Co^{3+} surface ions) and the B-terminated oxide surface (only Co^{3+} ions). The influence of temperature for a stoichiometric water layer was studied by comparing identical systems at 300 K and 450 K, as well as comparing a stoichiometric water layer with a H-deficient water layer where 8 hydrogen atoms were removed. Both systems were electroneutral.

On the A-terminated surface, the alcoholic species and its base were adsorbed via the oxygen atom to a Co^{2+} site. In the reference system at room temperature over a period of 20 ps, no bond breaking was observed. In both the thermal and electrochemical models, only proton transfer of the weakly acidic 2-proponal proton to the basic oxide was observed. No further reaction took place.

On the B-terminated surface, adsorption took place on Co_3O_4 sites. In contrast to the case of the A-terminated surface, no bond breaks via thermal activation of the stoichiometric water system on the B-terminated surface were observed, for which a lower degree of hydroxylation than for the A-terminated Co_3O_4 (001) surface[64] has been reported. For the H-deficient system, the reaction did not stop with the formation of 2-propanol. Again, different from the case of the A-terminated surface, the reaction proceeded to the full 2-electron oxidation step to form acetone. The hydrogen abstraction from the carbon atom occurred as a distinct second step several hundred femtoseconds later than the proton abstraction step from the oxygen. Stabilization of the various species and intermediates by hydrogen bonding from neighboring co-adsorbed water molecules and hydroxy groups was evident from the analysis presented above. The neighboring OH groups were essential for the reaction as they cooperated to accept the hydrogen atoms from the alcohol molecule. The Co^{3+} ions were the adsorption sites, and the organic oxygen atom remained attached to the adsorption site throughout all observed reaction steps.

The six simulations presented in this section were performed in the dilute limit and showed that the presence of the aqueous solvent is important. Thermal contributions to oxidation appeared to be less influential than the local oxidative character in an electrochemical environment. As observed, an increase in temperature to 450 K only facilitated the initial proton exchange between the organic solute and adsorbed solvent products, irrespective of the nature of the surface termination. The first acid-base proton transfer step was indeed more prevalent on the more strongly hydroxylated A-terminated surface than on the B-terminated surface. However, partial oxidation, including electron transfer, occurred in the studied systems only in an electrochemically oxidative environment.

At variance with such theoretical observations, recent experimental work[32] has reported a remarkable conversion of 2-propanol to acetone in the temperature range from

373 K to 573 K, with a maximum conversion around 430 K for liquid phase but also for gas phase oxidation. One possible shortcoming of the simulated model systems here is the absence of a true oxidant such as an active oxygen or peroxo species so that hydrogen atoms and electrons in the oxidation process must be accepted by the aqueous phase and the oxide, respectively. Studying such a system with a true oxidant is the objective of the next section.

6.3 2-propanol Oxidation in the Gas Phase

The motivation behind studying the oxidation of 2-propanol in the gas phase is to gain insights into the similarities and differences, as well as the general characteristics, between gas phase and liquid phase oxidation. Furthermore, by utilizing a true oxidizing agent like oxygen (as discussed in section 6.2.7), the realistic impact of temperature can be considered.

To investigate gas phase oxidation, dioxygen can be employed as the oxidizing agent, which has been reported to dissociate on the Co_3O_4 surface into two atomic oxygen species in a previous experimental study.[6] For practicality, we assume that this dissociation has already occurred. Therefore, the simulation consists of a system comprising the B-terminated (001) surface, eight 2-propanol molecules, and eight adsorbed atomic oxygen species. Figure 61 showcases the top (a), front (b), left (c), and perspective (d) views of this system.

Partial oxidation of 2-propanol to form acetone occurs in only one out of the eight 2-propanol molecules, while the remaining seven molecules remain adsorbed in their molecular state. The evolution of O–H, C–H, C–O, and Co^{3+}–O distances, for the dissociating 2-propanol molecule during the 20 ps of AIMD simulation is depicted in Figure 62. Initially, all bond lengths exhibit fluctuations around their original values. Throughout the first 19 ps of the simulation, no dissociation takes place. However, in the final picosecond of the simulation, both the hydroxyl hydrogen and hydrogen in CH group undergo abstraction, leading to the formation of an acetone molecule. Subsequently, as the O–H and C–H bonds break, the C–O bond becomes shorter, indicating the formation of a double bond due to acetone creation.

A distinct observation, in comparison to oxidation in the liquid phase, is that after 19 ps of inactivity (i.e., no dissociation), the system undergoes immediate deprotonation and dehydrogenation. This behavior is specific to this particular simulation and has not been observed in any of the previous simulations conducted in this study.

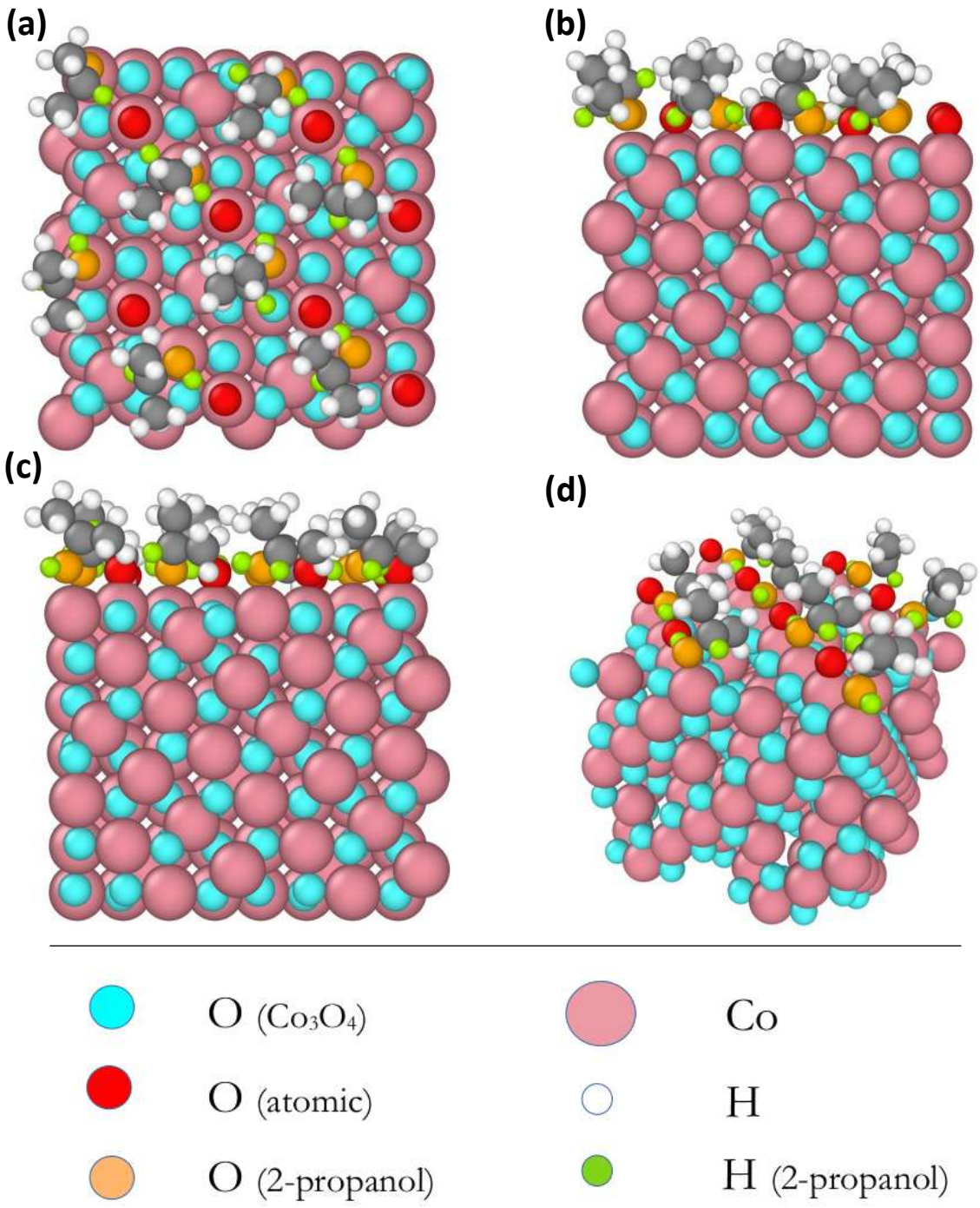

Figure 61: Initial snapshots of the AIMD simulation (top, front, left and perspective views) for system consisted of the B-terminated (001) surface, eight 2-propanol molecules and 8 adsorbed atomic oxygens at 300 K. Co (pink), O in Co_3O_4 (cyan), atomic O (red), O in 2-propanol (orange), C (gray), H in O–H and C2–H (green), and other H (white).

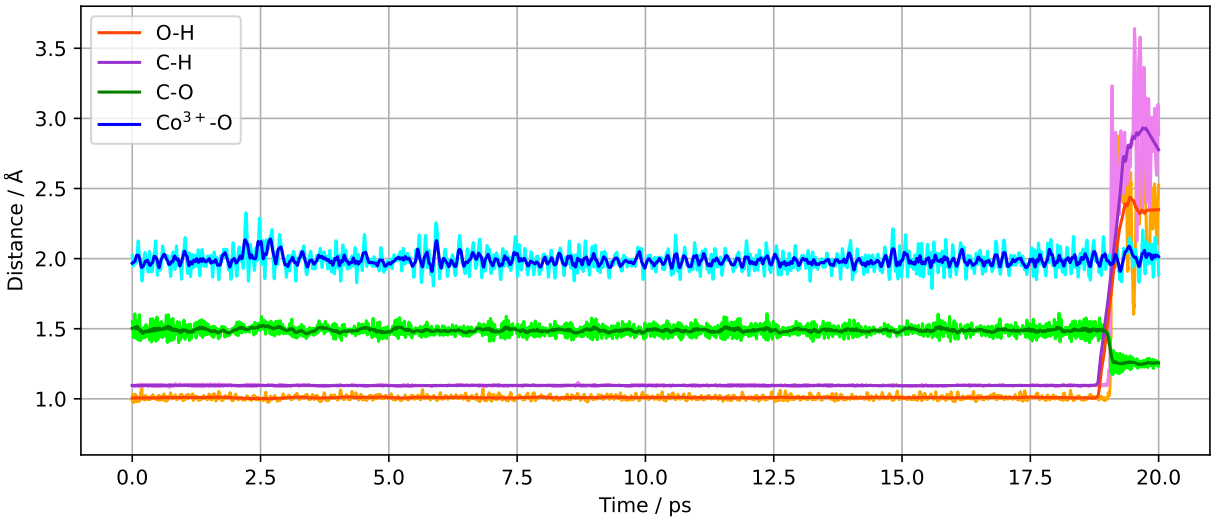

Figure 62: Evolution of O–H, C–H, C–O and Co^{3+}–O distances for the B-terminated (001) surface at 300 K during the 20 ps of AIMD simulation.

6.4 Comparison Between 2-propanol Oxidation in Liquid Phase and Gas Phase

The comparison between oxidation in the liquid and gas phases raises the question of whether there are fundamental differences between the two. To investigate this, we examined the time evolution of both cases to determine the exact timing of the reaction. In Figure 63 (a), we observe the first 2 ps of the simulation for liquid-phase oxidation, while Figure 63 (b) illustrates the last 2 ps of the simulation for gas-phase oxidation. A noticeable distinction becomes apparent: in the liquid phase, the cleavage of O–H and C–H bonds occurs sequentially, whereas in the gas phase, these cleavages happen simultaneously.

Figure 64 presents the evolution of Hirshfeld atomic charges for both liquid-phase (a) and gas-phase (b) oxidations. In Figure 64 (a), we initially observe a higher positive charge on the hydroxyl hydrogen compared to the hydrogen in C2–H, which aligns with chemical intuition. As the oxidation reaction progresses and both hydrogens are abstracted and transferred to neighboring OH groups, their atomic charges become equivalent. The oxygen atom of the 2-propanol molecule starts with a charge of approximately – 0.2 e but loses some electron density after the oxidation reaction, resulting in a total charge of about – 0.05 e. C2 begins with a charge of approximately – 0.1 e and experiences a decrease in electron density after the oxidation reaction, maintaining its new charge of approximately + 0.35 e until the end of the simulation.

Similar trends and initial/final charge values are observed for the 2-propanol molecule oxidized in the gas phase (Figure 64 (b)). The main difference lies in the simultaneous charge transfer observed in gas-phase oxidation compared to the step-wise charge transfer

in liquid-phase oxidation.

Overall, the oxidation process in aqueous solution can be characterized as proceeding through "stepwise reactions". Water plays an active role in facilitating oxidation by participating in deprotonation and dehydrogenation reactions. In contrast, oxidation in the gas phase can be characterized as involving "simultaneous/concerted" charge transfers. This distinction can be attributed to the presence of OH groups (in the liquid phase), which enable the temporary storage of transferring protons, allowing the oxidation reaction to proceed stepwise—a process that is not possible in the gas phase.

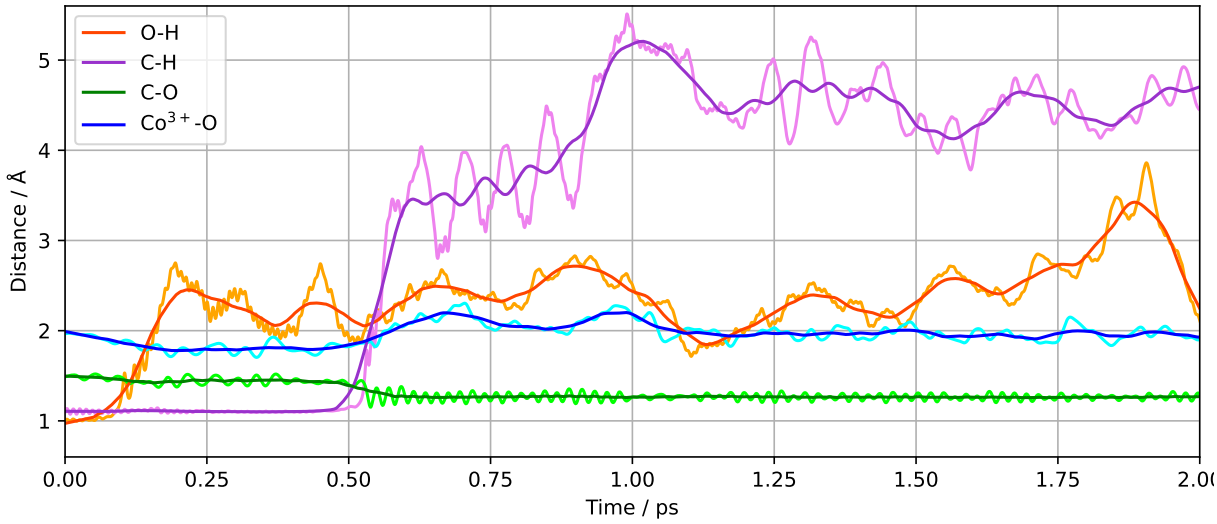

(a)

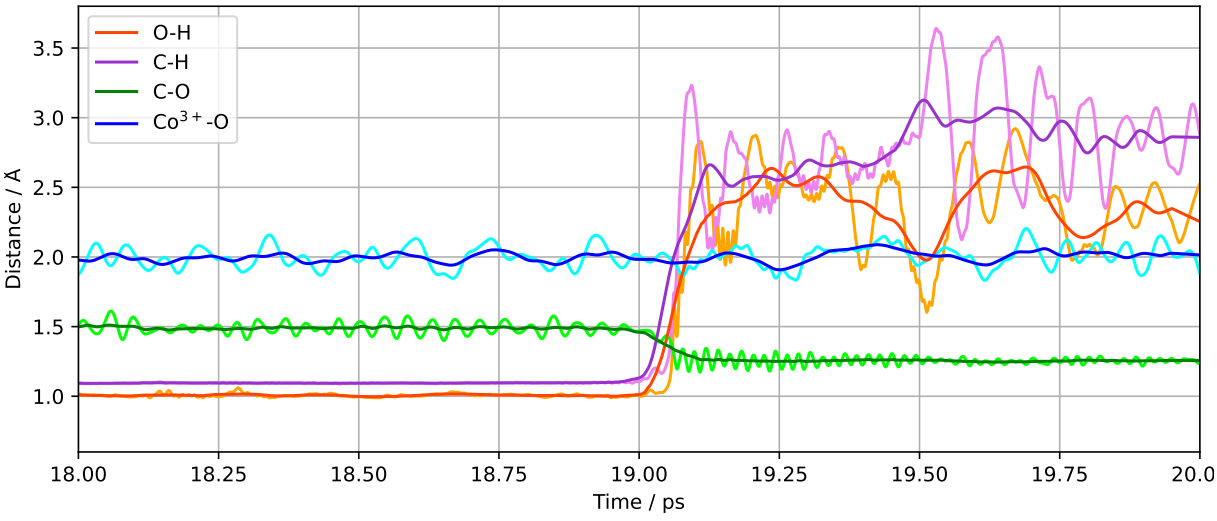

(b)

Figure 63: Evolution of O–H, C–H, C–O and Co^{3+}–O distances for the B-terminated (001) surface at 300 K during the 2 ps of AIMD simulation when the oxidation reaction take place: (a) in the liquid phase and (b) in the gas phase.

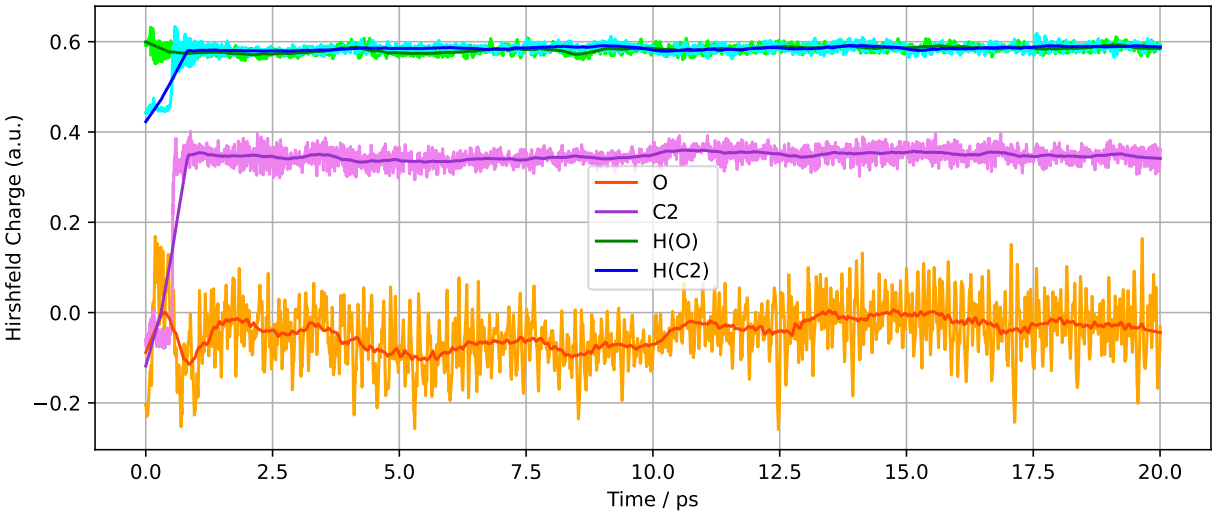

(a)

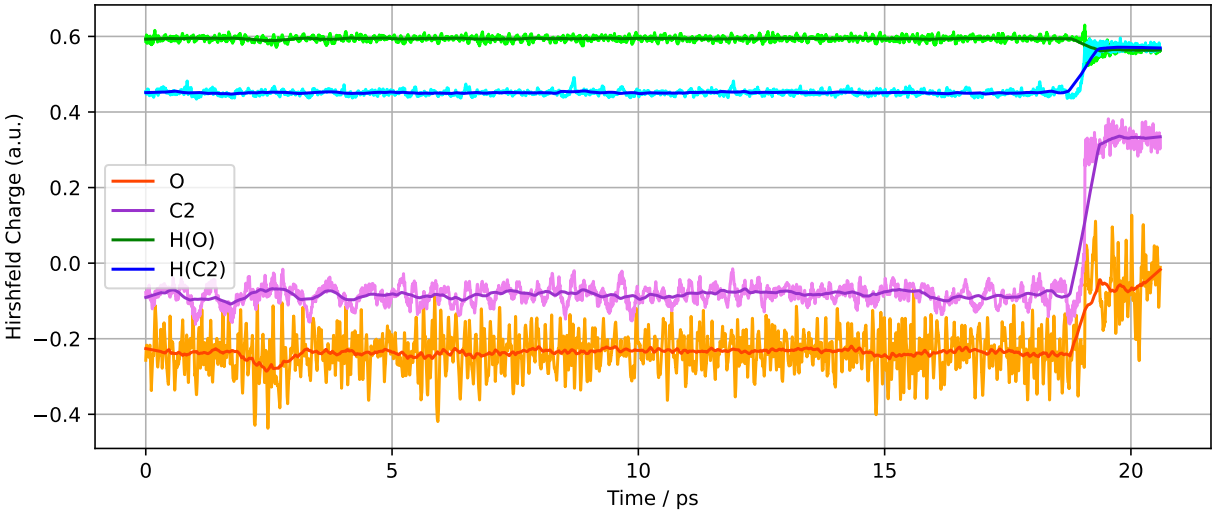

(b)

Figure 64: Evolution of Hirshfeld atomic charges of O (orange), C2 (violet), hydroxyl hydrogen (green) and hydrogen in C2–H (blue) during the 20 ps of AIMD simulation when the oxidation reaction take place: (a) in the liquid phase and (b) in the gas phase.

6.5 2-propanol Oxidation in the Gas Phase at High Temperature

Recent experimental work[32] has highlighted the significant conversion of 2-propanol to acetone within a temperature range of 373 K to 573 K both in liquid and gas phase oxidation. In our previous models, it was suggested (as discussed in section 6.2.7) that the absence of a true oxidant, such as an active oxygen or peroxo species, might explain the limitations in capturing the temperature impact observed in the aforementioned experimental study. To test this hypothesis, the following investigation is conducted:

(1) The exact initial system described in section 6.3 (Figure 61) is employed consisting of (Figure 65 (left)):

- 8 2-propanol molecules
- 8 atomic oxygen species

(2) The temperature is subsequently raised from 300 K to 700 K. The final result is displayed in Figure 65 (right), which includes:

- 3 water molecules (indicated by black circles)
- 4 OH groups
- 1 atomic oxygen species
- 4 acetone molecules
- 2 2-propoxide molecules
- 2 2-propanol molecules

Therefore, a total of four 2-propanol molecules are oxidized during the simulation. The formation of water is a distinctive feature of this particular simulation. By comparing these results with the system at 300 K, where only one 2-propanol oxidation took place, it can be concluded that the earlier hypothesis regarding the impact of temperature in a system with a true oxidant is confirmed.

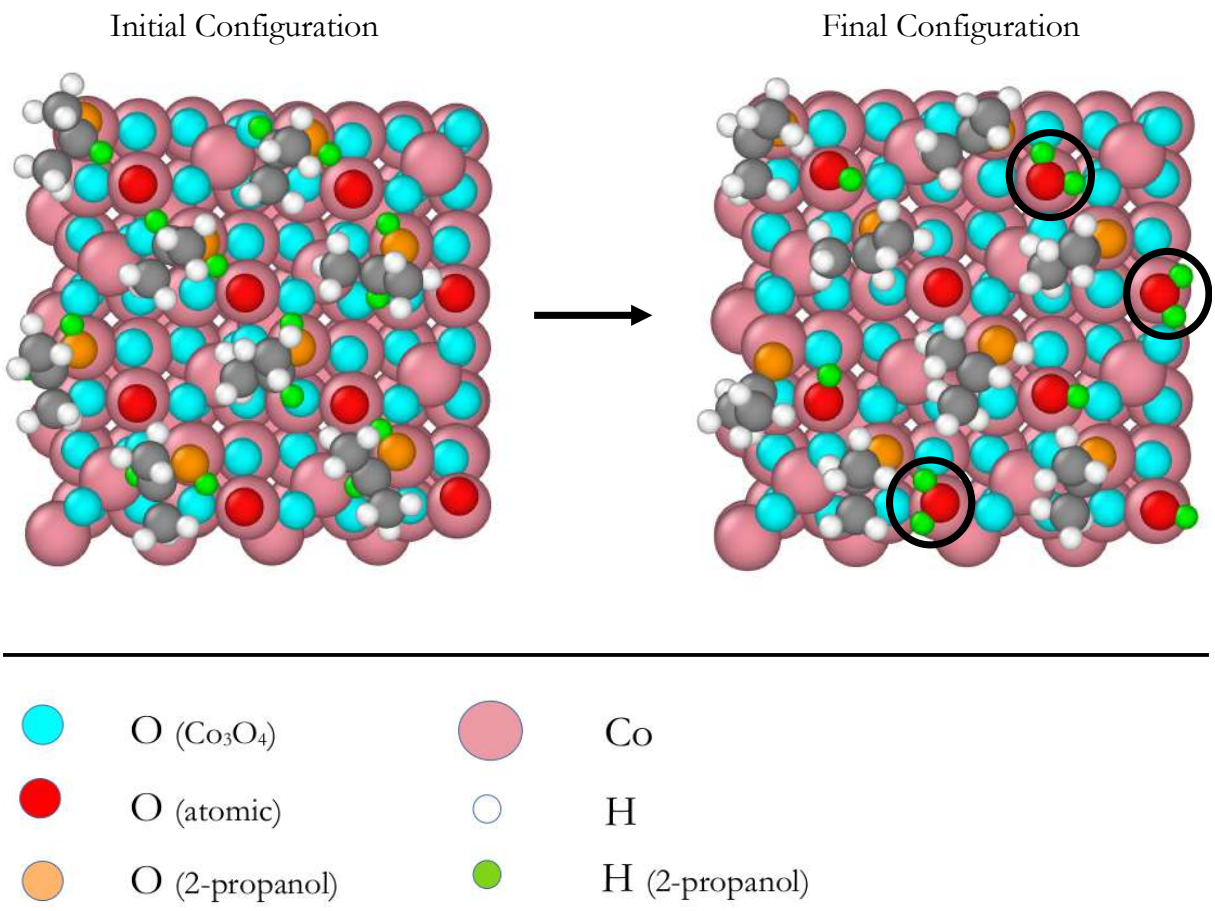

Figure 65: Initial (left) and final (right) configurations of the AIMD simulation (top, front, left and perspective views) for system consisted of the B-terminated (001) surface, eight 2-propanol molecules and 8 adsorbed atomic oxygens at 700 K. Co (pink), O in Co_3O_4 (cyan), atomic O (red), O in 2-propanol (orange), C (gray), H in O–H and C2–H (green), and other H (white).

7 Summary and Conclusions

In this work, ab initio Molecular Dynamics (AIMD) simulations are employed to investigate the structure, dynamics, and reactivity of Co_3O_4 spinel interacting with 2-propanol, water, and oxygen. The following conclusions are made:

Co_3O_4 (001)/2-Propanol Interaction

On the B-terminated Co_3O_4 (001) surface, 2-propanol adsorbs molecularly on the Co^{3+} adsorption sites, although minor dissociation is also observed. The presence of water in the environment hinders the dissociation of the 2-propanol molecule by deactivating the lattice oxygen. The simulation results are in agreement with the vibrational sum frequency generation spectroscopy (vSFG) experiment.[80] The distribution of the angles between the O–H vector and surface normal (z-axis) reveals that this angle varies between 70° and 90°, indicating that the O–H bonds slightly point away from the surface. Elevated temperature slightly reduces the 2-propanol/Co_3O_4 (001) interaction by increasing the adsorbate/Co_3O_4 (001) distances. Although the Co^{3+} ions are the primary adsorption sites on the B-terminated (001) surface, Co^{2+} ions also participate electronically upon 2-propanol adsorption. On the A-terminated (001) surface, the adsorption sites are mainly Co^{2+} ions. The 2-propanol dissociation is more pronounced on the A-terminated (001) surface, particularly at high temperatures.

Co_3O_4 (111)/2-Propanol and Co_3O_4 (110)/2-Propanol Interactions

On the Co_3O_4 (111) surface, 2-propanol molecules adsorb on Co^{3+} sites, and in contrast to the Co_3O_4 (001) surface, all 2-propanol molecules fully dissociate. Co^{2+} ions on the B-terminated (111) surface are significantly more involved compared to the B-terminated (001) surface. This participation leads to the formation of Co^{3+}–$O_{2\text{-propoxide}}$–Co^{2+} bridges between adsorption sites and the adsorbates. Additionally, the Mars-van Krevelen mechanism is observed on the (111) surface, in which a surface OH group is converted to water by abstracting the hydroxyl hydrogen of a 2-propanol molecule, leaving an oxygen vacancy in the lattice.

The B-terminated Co_3O_4 (110) surface exhibits higher activity for 2-propanol dissociation compared to the B-terminated (001) surface. The reactivity of the B-terminated Co_3O_4 (110) surface increases sharply with temperature. This temperature-dependent surface activity is attributed to the presence of peculiar "two-fold" coordinatively unsaturated surface oxygen, which is unique to the B-terminated Co_3O_4 (110) surface. The activity of these "two-fold" surface oxygens substantially increases with temperature.

Overall, both B-terminated (111) and (110) surfaces demonstrate higher activity towards 2-propanol dissociation compared to the (001) surface. While the (111) surface exhibits higher reactivity at lower temperatures, at higher temperatures, the (110) sur-

face can be as active as the (111) surface.

2-Propanol Oxidation in the Liquid Phase

On the A-terminated (001) surface, the hydrated 2-propanol molecularly adsorbs on a Co^{2+} ion. However, increasing the temperature or creating an H-deficient environment causes the 2-propanol molecule to dissociate, producing 2-propoxide.

On the B-terminated (001) surface, the hydrated 2-propanol molecularly adsorbs on a Co^{3+} ion. Increasing the temperature does not impact the molecular adsorption of 2-propanol. However, manipulating the electrochemical potential of the water film by removing a few H atoms leads to the partial oxidation of 2-propanol. The produced acetone is shown to remain adsorbed on the same Co^{3+} adsorption site for the rest of the simulation. The various stages of 2-propanol partial oxidation are discussed in detail, supplemented by charge analysis. The B-terminated (001) surface is found to be favorable for the partial oxidation of 2-propanol due to the existing "mobile OH^- groups" available in the epitaxial water film.

2-Propanol Oxidation in the Gas Phase

One limitation of the previous model for simulating 2-propanol oxidation was its inability to realistically capture the impact of temperature, mainly due to the lack of a true oxidizing agent such as active oxygen species. By introducing oxygen species into the system, the oxidative dehydrogenation of 2-propanol is observed at high temperature. During this reaction, 2-propanol and oxygen, as the reactants, are converted into acetone and water.

By comparing the oxidation of 2-propanol in the liquid phase and gas phase, it is shown that the oxidation process in the aqueous solution occurs through stepwise reactions. Water plays an active role by participating in deprotonation and dehydrogenation reactions, facilitating the oxidation process. In contrast, oxidation in the gas phase involves simultaneous or concerted charge transfers. This distinction can be attributed to the presence of hydroxide groups (OH^-) in the liquid phase, which enable the temporary storage of transferring protons. This allows for the stepwise progression of the oxidation reaction, a process that is not possible in the gas phase.

Final Remark

Overall, it can be said that the interaction between water and transition metal oxides (TMOs), such as Co_3O_4, exhibits a higher level of complexity compared to the water/metal interface. Water plays a multifaceted role at this interface, with both positive and negative effects on the 2-propanol oxidation process. On the positive side, water facilitates 2-propanol oxidation by providing "mobile OH^- groups" that can temporarily store protons. Additionally, previous studies[73] have demonstrated that water also promotes the

activation of O_2 in gas-phase oxidation. On the negative side, water can compete with 2-propanol molecules for the adsorption sites. It also diminishes the surface reactivity by deactivating the lattice oxygens of the TMOs. Determining which of these competing factors ultimately plays the decisive role for the oxidation reaction remains an open question.

References

[1] B. J. Alder and T. E. Wainwright. Phase transition for a hard sphere system. *The Journal of chemical physics*, 27(5):1208–1209, 1957.

[2] B. J. Alder and T. E. Wainwright. Studies in molecular dynamics. i. general method. *The Journal of Chemical Physics*, 31(2):459–466, 1959.

[3] H. C. Andersen. Molecular dynamics simulations at constant pressure and/or temperature. *The Journal of chemical physics*, 72(4):2384–2393, 1980.

[4] V. I. Anisimov, F. Aryasetiawan, and A. Lichtenstein. First-principles calculations of the electronic structure and spectra of strongly correlated systems: the LDA+U method. *Journal of Physics: Condensed Matter*, 9(4):767, 1997.

[5] V. I. Anisimov, J. Zaanen, and O. K. Andersen. Band theory and Mott insulators: Hubbard U instead of Stoner I. *Physical Review B*, 44(3):943, 1991.

[6] S. Anke, G. Bendt, I. Sinev, H. Hajiyani, H. Antoni, I. Zegkinoglou, H. Jeon, R. Pentcheva, B. Roldan Cuenya, S. Schulz, et al. Selective 2-propanol oxidation over unsupported Co_3O_4 spinel nanoparticles: mechanistic insights into aerobic oxidation of alcohols. *ACS Catalysis*, 9(7):5974–5985, 2019.

[7] S. Anke, T. Falk, G. Bendt, I. Sinev, M. Haevecker, H. Antoni, I. Zegkinoglou, H. Jeon, A. Knop-Gericke, R. Schlögl, et al. On the reversible deactivation of cobalt ferrite spinel nanoparticles applied in selective 2-propanol oxidation. *J. Catal.*, 382:57–68, 2020.

[8] B. Axilrod and E. Teller. Interaction of the van der waals type between three atoms. *The Journal of Chemical Physics*, 11(6):299–300, 1943.

[9] A. D. Becke and E. R. Johnson. Exchange-hole dipole moment and the dispersion interaction: High-order dispersion coefficients. *The Journal of chemical physics*, 124(1):014104, 2006.

[10] D. Beeman. Some multistep methods for use in molecular dynamics calculations. *Journal of computational physics*, 20(2):130–139, 1976.

[11] L. Bengtsson. Dipole correction for surface supercell calculations. *Physical Review B*, 59(19):12301, 1999.

[12] H. J. Berendsen, J. v. Postma, W. F. Van Gunsteren, A. DiNola, and J. R. Haak. Molecular dynamics with coupling to an external bath. *The Journal of chemical physics*, 81(8):3684–3690, 1984.

[13] F. Bloch. Über die Quantenmechanik der Elektronen in Kristallgittern. *Zeitschrift für physik*, 52(7-8):555–600, 1929.

[14] M. Born and W. Heisenberg. Zur Quantentheorie der Molekeln. *Original Scientific Papers Wissenschaftliche Originalarbeiten*, pages 216–246, 1985.

[15] M. Born, W. Heisenberg, and P. Jordan. Zur Quantenmechanik. II. *Zeitschrift für Physik*, 35(8-9):557–615, 1926.

[16] M. Born and P. Jordan. Zur Quantenmechanik. *Zeitschrift für Physik*, 34(1):858–888, 1925.

[17] M. Brehm, M. Thomas, S. Gehrke, and B. Kirchner. Travis—a free analyzer for trajectories from molecular simulation. *The Journal of chemical physics*, 152(16):164105, 2020.

[18] K. Burke. Perspective on density functional theory. *The Journal of chemical physics*, 136(15):150901, 2012.

[19] E. Caldeweyher, C. Bannwarth, and S. Grimme. Extension of the d3 dispersion coefficient model. *The Journal of chemical physics*, 147(3):034112, 2017.

[20] D. Chandler. Introduction to modern statistical. *Mechanics. Oxford University Press, Oxford, UK*, 5:449, 1987.

[21] J. Chen, X. Wu, and A. Selloni. Electronic structure and bonding properties of cobalt oxide in the spinel structure. *Phys. Rev. B*, 83(24):245204, jun 2011.

[22] I. Choudhuri and D. G. Truhlar. Calculating and characterizing the charge distributions in solids. *Journal of Chemical Theory and Computation*, 16(9):5884–5892, 2020.

[23] J. Čížek. On the correlation problem in atomic and molecular systems. calculation of wavefunction components in ursell-type expansion using quantum-field theoretical methods. *The Journal of Chemical Physics*, 45(11):4256–4266, 1966.

[24] M. Cococcioni and S. De Gironcoli. Linear response approach to the calculation of the effective interaction parameters in the LDA+U method. *Physical Review B*, 71(3):035105, 2005.

[25] F. Creazzo, D. R. Galimberti, S. Pezzotti, and M. P. Gaigeot. DFT-MD of the (110)-Co_3O_4 cobalt oxide semiconductor in contact with liquid water, preliminary chemical and physical insights into the electrochemical environment. *Journal of Chemical Physics*, 150(4), 2019.

[26] M. Dion, H. Rydberg, E. Schröder, D. C. Langreth, and B. I. Lundqvist. Van der waals density functional for general geometries. *Physical review letters*, 92(24):246401, 2004.

[27] M. Doheim and H. El-Shobaky. Catalytic conversion of ethanol and iso-propanol over zno-treated Co_3O_4/Al_2O_3 solids. *Colloids and Surfaces A*, 204(1-3):169–174, 2002.

[28] D. H. Douma, K. N. Nono, A. H. Omranpoor, A. Lamperti, A. Debernardi, and S. Kenmoe. Probing the local environment of active sites during 2-propanol oxidation to acetone on the Co_3O_4 (001) surface: insights from first principles O K-edge XANES spectroscopy. *The Journal of Physical Chemistry C*, 2023.

[29] M. Dreyer, D. Cruz, U. Hagemann, P. Zeller, M. Heidelmann, S. Salamon, J. Landers, A. Rabe, K. F. Ortega, S. Najafishirtari, et al. The effect of water on the 2-propanol oxidation activity of Co-substituted $LaFe_{1-x}Co_xO_3$ perovskites. *Chemistry–A European Journal*, 27(68):17127–17144, 2021.

[30] R. Eisenschitz and F. London. Über das Verhältnis der van der Waalsschen Kräfte zu den homöopolaren Bindungskräften. *Zeitschrift für Physik*, 60(7-8):491–527, 1930.

[31] T. Falk, S. Anke, H. Hajiyani, S. Saddeler, S. Schulz, R. Pentcheva, B. Peng, and M. Muhler. Influence of the particle size on selective 2-propanol gas-phase oxidation over Co_3O_4 nanospheres. *Catal. Sci. Technol.*, 11:7552–7562, 2021.

[32] T. Falk, E. Budiyanto, M. Dreyer, C. Pflieger, D. Waffel, J. Büker, C. Weidenthaler, K. F. Ortega, M. Behrens, H. Tüysüz, et al. Identification of active sites in the catalytic oxidation of 2-propanol over $Co_{1+x}Fe_{2-x}O_4$ spinel oxides at solid/liquid and solid/gas interfaces. *ChemCatChem*, 13(12):2942–2951, 2021.

[33] E. Finocchio, R. J. Willey, G. Busca, and V. Lorenzelli. FTIR studies on the selective oxidation and combustion of light hydrocarbons at metal oxide surfaces part 3.–comparison of the oxidation of C_3 organic compounds over Co_3O_4, $MgCr_2O_4$ and CuO. *J. Chem. Soc., Faraday Trans.*, 93(1):175–180, 1997.

[34] V. Fock. Näherungsmethode zur Lösung des quantenmechanischen Mehrkörperproblems. *Zeitschrift für Physik*, 61:126–148, 1930.

[35] D. Frenkel and B. Smit. *Understanding molecular simulation: from algorithms to applications*, volume 1. Elsevier, 2001.

[36] C. W. Gear. Numerical initial value problems in ordinary differential equations. *Prentice-Hall series in automatic computation*, 1971.

[37] J. W. Gibbs. *Elementary principles in statistical mechanics: developed with especial reference to the rational foundations of thermodynamics*. C. Scribner's sons, 1902.

[38] S. Grimme. Accurate description of van der waals complexes by density functional theory including empirical corrections. *Journal of computational chemistry*, 25(12):1463–1473, 2004.

[39] S. Grimme. Semiempirical GGA-type density functional constructed with a long-range dispersion correction. *Journal of computational chemistry*, 27(15):1787–1799, 2006.

[40] S. Grimme, J. Antony, S. Ehrlich, and H. Krieg. A consistent and accurate ab initio parametrization of density functional dispersion correction (dft-d) for the 94 elements h-pu. *J. Chem. Phys.*, 132(15):154104, 2010.

[41] S. Grimme, S. Ehrlich, and L. Goerigk. Effect of the damping function in dispersion corrected density functional theory. *Journal of computational chemistry*, 32(7):1456–1465, 2011.

[42] S. Grimme, A. Hansen, J. G. Brandenburg, and C. Bannwarth. Dispersion-corrected mean-field electronic structure methods. *Chemical reviews*, 116(9):5105–5154, 2016.

[43] O. Gunnarsson and B. I. Lundqvist. Exchange and correlation in atoms, molecules, and solids by the spin-density-functional formalism. *Physical Review B*, 13(10):4274, 1976.

[44] A. Haas. Die Quantenstatistik und ihre Anwendung auf die Elektronentheorie der Metalle: L. Brillouin, Aus dem Französischen übersetzt von E. Rabinowitsch, Göttingen. 530 S., 57 Abb.(Band XIII der Sammlung Struktur der Materie in Einzeldarstellungen.) verlag julius springer, berlin 1933. preis rm 42. *Monatshefte für Mathematik und Physik*, 40:A38–A39, 1933.

[45] J. M. Haile. *Molecular dynamics simulation: elementary methods*. John Wiley & Sons, Inc., 1992.

[46] D. R. Hartree. The wave mechanics of an atom with a non-coulomb central field. part i. theory and methods. In *Mathematical Proceedings of the Cambridge Philosophical Society*, volume 24, pages 89–110. Cambridge university press, 1928.

[47] A. H. Hashim, S. M. Zain, V. S. Lee, S. M. Said, et al. Electronic, magnetic and structural properties of Co_3O_4 (100) surface: a DFT+U study. *Applied Surface Science*, 427:1090–1095, 2018.

[48] W. Heisenberg. *Über quantentheoretische Umdeutung kinematischer und mechanischer Beziehungen.* Springer, 1985.

[49] C. K. Hill and J. F. Hartwig. Site-selective oxidation, amination and epimerization reactions of complex polyols enabled by transfer hydrogenation. *Nat. Chem.*, 9(12):1213–1221, 2017.

[50] F. L. Hirshfeld. Bonded-atom fragments for describing molecular charge densities. *Theoretica chimica acta*, 44:129–138, 1977.

[51] R. W. Hockney and J. W. Eastwood. *Computer simulation using particles*. crc Press, 2021.

[52] P. Hohenberg and W. Kohn. Inhomogeneous electron gas. *Physical review*, 136(3B):B864, 1964.

[53] W. G. Hoover. Canonical dynamics: Equilibrium phase-space distributions. *Physical review A*, 31(3):1695, 1985.

[54] L. Hu, Q. Peng, and Y. Li. Selective synthesis of Co_3O_4 nanocrystal with different shape and crystal plane effect on catalytic property for methane combustion. *Journal of the American Chemical Society*, 130(48):16136–16137, 2008.

[55] J. Hubbard. Electron correlations in narrow energy bands. *Proceedings of the Royal Society of London. Series A. Mathematical and Physical Sciences*, 276(1365):238–257, nov 1963.

[56] J. Hutter, M. Iannuzzi, F. Schiffmann, and J. VandeVondele. cp2k: atomistic simulations of condensed matter systems. *Wiley Interdisciplinary Reviews: Computational Molecular Science*, 4(1):15–25, 2014.

[57] F. Jiao and H. Frei. Nanostructured cobalt oxide clusters in mesoporous silica as efficient oxygen-evolving catalysts. *Angewandte Chemie*, 121(10):1873–1876, 2009.

[58] E. R. Johnson and A. D. Becke. A post-hartree–fock model of intermolecular interactions. *The Journal of chemical physics*, 123(2):024101, 2005.

[59] B. Katryniok, S. Paul, and F. Dumeignil. Recent developments in the field of catalytic dehydration of glycerol to acrolein. ACS Catal 3: 1819–1834, 2013.

[60] S. Kenmoe, D. H. Douma, A. T. Raji, B. M'Passi-Mabiala, T. Götsch, F. Girgsdies, A. Knop-Gericke, R. Schlögl, and E. Spohr. X-ray Absorption Near-Edge Structure (XANES) at the O K-Edge of Bulk Co_3O_4: Experimental and Theoretical Studies. *Nanomaterials*, 12(6):921, 2022.

[61] K. J. Kim and Y. R. Park. Optical investigation of charge-transfer transitions in spinel Co_3O_4. *Solid state communications*, 127(1):25–28, 2003.

[62] W. Kohn and L. J. Sham. Self-consistent equations including exchange and correlation effects. *Physical review*, 140(4A):A1133, 1965.

[63] K. Koumoto and H. Yanagida. Electrical conduction in pure and Li-substituted Co_3O_4. *Journal of the American Ceramic Society*, 64(11):C–156, 1981.

[64] T. Kox, E. Spohr, and S. Kenmoe. Impact of solvation on the structure and reactivity of the Co_3O_4 (001)/H_2O interface: Insights from molecular dynamics simulations. *Front. Energy Res.*, 8:312, 2020.

[65] T. D. Kühne, M. Iannuzzi, M. Del Ben, V. V. Rybkin, P. Seewald, F. Stein, T. Laino, R. Z. Khaliullin, O. Schütt, F. Schiffmann, et al. Cp2k: An electronic structure and molecular dynamics software package-quickstep: Efficient and accurate electronic structure calculations. *The Journal of Chemical Physics*, 152(19):194103, 2020.

[66] M. Langell, M. Anderson, G. Carson, L. Peng, and S. Smith. Valence-band electronic structure of Co_3O_4 epitaxy on CoO (100). *Physical Review B*, 59(7):4791, 1999.

[67] W.-Y. Li, L.-N. Xu, and J. Chen. Co_3O_4 nanomaterials in lithium-ion batteries and gas sensors. *Advanced Functional Materials*, 15(5):851–857, 2005.

[68] A. Liechtenstein, V. I. Anisimov, and J. Zaanen. Density-functional theory and strong interactions: Orbital ordering in mott-hubbard insulators. *Physical Review B*, 52(8):R5467, 1995.

[69] G. J. Martyna, M. L. Klein, and M. Tuckerman. Nosé–hoover chains: The canonical ensemble via continuous dynamics. *The Journal of chemical physics*, 97(4):2635–2643, 1992.

[70] D. Marx and J. Hutter. Ab initio molecular dynamics: Theory and implementation. *Modern methods and algorithms of quantum chemistry*, 1(301-449):141, 2000.

[71] C. Møller and M. S. Plesset. Note on an approximation treatment for many-electron systems. *Physical review*, 46(7):618, 1934.

[72] R. S. Mulliken. Electronic population analysis on LCAO–MO molecular wave functions. i. *The Journal of Chemical Physics*, 23(10):1833–1840, 1955.

[73] D. Muñoz-Santiburcio, M. Farnesi Camellone, and D. Marx. Inside cover: Solvation-induced changes in the mechanism of alcohol oxidation at gold/titania nanocatalysts in the aqueous phase versus gas phase (angew. chem. int. ed. 13/2018). *Angew. Chem. Int. Ed.*, 57(13):3266–3266, 2018.

[74] T. Murayama, B. Katryniok, S. Heyte, M. Araque, S. Ishikawa, F. Dumeignil, S. Paul, and W. Ueda. Role of crystalline structure in allyl alcohol selective oxidation over Mo_3VOx complex metal oxide catalysts. *ChemCatChem*, 8(14):2415–2420, 2016.

[75] S. Najafishirtari, K. Friedel Ortega, M. Douthwaite, S. Pattisson, G. J. Hutchings, C. J. Bondue, K. Tschulik, D. Waffel, B. Peng, M. Deitermann, et al. A perspective on heterogeneous catalysts for the selective oxidation of alcohols. *Chemistry–A European Journal*, 27(68):16809–16833, 2021.

[76] J. Neugebauer and T. Hickel. Density functional theory in materials science. *Wiley Interdisciplinary Reviews: Computational Molecular Science*, 3(5):438–448, 2013.

[77] S. Nosé. A molecular dynamics method for simulations in the canonical ensemble. *Molecular physics*, 52(2):255–268, 1984.

[78] S. Nosé. A unified formulation of the constant temperature molecular dynamics methods. *The Journal of chemical physics*, 81(1):511–519, 1984.

[79] A. Omranpoor, T. Kox, E. Spohr, and S. Kenmoe. Influence of temperature, surface composition and electrochemical environment on 2-propanol decomposition at the Co_3O_4 (001)/H_2O interface. *Applied Surface Science Advances*, 12:100319, 2022.

[80] A. H. Omranpoor, A. Bera, D. Bullert, M. Linke, S. Salamon, S. Webers, H. Wende, E. Hasselbrink, E. Spohr, and S. Kenmoe. 2-Propanol interacting with Co_3O_4(001): A combined vSFS and AIMD study. *The Journal of Chemical Physics*, 158(16), 04 2023. 164703.

[81] M. Pant and A. Rajagopal. Theory of inhomogeneous magnetic electron gas. *Solid State Communications*, 10(12):1157–1160, 1972.

[82] J. P. Perdew, K. Burke, and M. Ernzerhof. Generalized gradient approximation made simple. *Phys. Rev. Lett.*, 77(18):3865–3868, 1996.

[83] J. P. Perdew, J. A. Chevary, S. H. Vosko, K. A. Jackson, M. R. Pederson, D. J. Singh, and C. Fiolhais. Atoms, molecules, solids, and surfaces: Applications of the generalized gradient approximation for exchange and correlation. *Physical review B*, 46(11):6671, 1992.

[84] J. P. Perdew and K. Schmidt. Jacob's ladder of density functional approximations for the exchange-correlation energy. In *AIP Conference Proceedings*, volume 577, pages 1–20. American Institute of Physics, 2001.

[85] R. Peverati and D. G. Truhlar. Quest for a universal density functional: the accuracy of density functionals across a broad spectrum of databases in chemistry and physics. *Philosophical Transactions of the Royal Society A: Mathematical, Physical and Engineering Sciences*, 372(2011):20120476, 2014.

[86] W. Ritz. Über eine neue Methode zur Lösung gewisser Variationsprobleme der mathematischen Physik. 1909.

[87] W. Roth. The magnetic structure of Co_3O_4. *Journal of Physics and Chemistry of Solids*, 25(1):1–10, 1964.

[88] T. Sato and H. Nakai. Density functional method including weak interactions: Dispersion coefficients based on the local response approximation. *The Journal of chemical physics*, 131(22):224104, 2009.

[89] R. Schlögl. Handbook of heterogeneous catalysis. *Bd*, 5:2501–2575, 2008.

[90] R. Schlögl. Heterogeneous catalysis. *Angewandte Chemie International Edition*, 54(11):3465–3520, 2015.

[91] E. Schrödinger. Quantisierung als Eigenwertproblem. *Annalen der physik*, 385(13):437–490, 1926.

[92] V. Shinde, S. Mahadik, T. Gujar, and C. Lokhande. Supercapacitive cobalt oxide (Co_3O_4) thin films by spray pyrolysis. *Applied Surface Science*, 252(20):7487–7492, 2006.

[93] J. C. Slater. The theory of complex spectra. *Physical Review*, 34(10):1293, 1929.

[94] T. K. Slot, D. Eisenberg, D. van Noordenne, P. Jungbacker, and G. Rothenberg. Cooperative catalysis for selective alcohol oxidation with molecular oxygen. *Chemistry–A European Journal*, 22(35):12307–12311, 2016.

[95] W. C. Swope, H. C. Andersen, P. H. Berens, and K. R. Wilson. A computer simulation method for the calculation of equilibrium constants for the formation of physical clusters of molecules: Application to small water clusters. *The Journal of chemical physics*, 76(1):637–649, 1982.

[96] A. Tkatchenko and M. Scheffler. Accurate molecular van der waals interactions from ground-state electron density and free-atom reference data. *Physical review letters*, 102(7):073005, 2009.

[97] M. Tuckerman. *Statistical mechanics: theory and molecular simulation*. Oxford university press, 2010.

[98] J. C. Védrine. Heterogeneous catalysis on metal oxides. *Catalysts*, 7(11):341, 2017.

[99] L. Verlet. Computer "experiments" on classical fluids. i. thermodynamical properties of lennard-jones molecules. *Physical review*, 159(1):98, 1967.

[100] U. Von Barth and L. Hedin. A local exchange-correlation potential for the spin polarized case. i. *Journal of Physics C: Solid State Physics*, 5(13):1629, 1972.

[101] F. Waidhas, S. Haschke, P. Khanipour, L. Fromm, A. Görling, J. Bachmann, I. Katsounaros, K. J. Mayrhofer, O. Brummel, and J. Libuda. Secondary alcohols as rechargeable electrofuels: Electrooxidation of isopropyl alcohol at pt electrodes. *ACS Catalysis*, 10(12):6831–6842, 2020.

[102] H.-F. Wang, R. Kavanagh, Y.-L. Guo, Y. Guo, G.-Z. Lu, and P. Hu. Structural origin: water deactivates metal oxides to CO oxidation and promotes low-temperature CO oxidation with metals. *Angew. Chem. Int. Ed.*, 51(27):6657–6661, 2012.

[103] Y. Wang and J. P. Perdew. Correlation hole of the spin-polarized electron gas, with exact small-wave-vector and high-density scaling. *Physical Review B*, 44(24):13298, 1991.

[104] X. Xie, Y. Li, Z.-Q. Liu, M. Haruta, and W. Shen. Low-temperature oxidation of CO catalysed by Co_3O_4 nanorods. *Nature*, 458(7239):746–749, 2009.

[105] T. Yang, M. Kastenmeier, M. Ronovskỳ, L. Fusek, T. Skála, F. Waidhas, M. Bertram, N. Tsud, P. Matvija, K. C. Prince, et al. Selective electrooxidation of 2-propanol on pt nanoparticles supported on Co_3O_4: an in-situ study on atomically defined model systems. *J. Phys. D*, 54(16):164002, 2021.

[106] S. Zerebecki, K. Schott, S. Salamon, J. Landers, H. Wende, E. Budiyanto, H. Tüysüz, S. Barcikowski, and S. Reichenberger. Gradually Fe-doped Co_3O_4 nanoparticles in 2-propanol and water oxidation catalysis with single laser pulse resolution. *The Journal of Physical Chemistry C*, 126(36):15144–15155, 2022.

Appendix

A1. DFT Settings

The following (Table 2) is the DFT settings for performing the Born-Oppenheimer Molecular Dynamics simulation in CP2K :

Table 2: DFT setting in CP2K.

Keyword	**Setting**
BASIS_SET_FILE_NAME	BASIS_MOLOPT
POTENTIAL_FILE_NAME	GTH_POTENTIALS
CUTOFF	500
REL_CUTOFF	60
NGRIDS	5
METHOD	GPW
EPS_DEFAULT	1.0E-10
EXTRAPOLATION	LINEAR_WF
PERIODIC	XYZ
SURF_DIP_DIR	Z
EPS_SCF	1.0E-6
MAX_SCF	50
PRECONDITIONER	FULL_KINETIC
ENERGY_GAP	1.2
MINIMIZER	BROYDEN
BROYDEN_BETA	8.50000000E-001
XC_FUNCTIONAL	PBE
DISPERSION_FUNCTIONAL	PAIR_POTENTIAL
TYPE	DFTD3(BJ)
CALCULATE_C9_TERM	.TRUE.
REFERENCE_C9_TERM	.TRUE.
PARAMETER_FILE_NAME	./dftd3.dat
REFERENCE_FUNCTIONAL	PBE

A2. Basis Sets, Pseudopotentials and Spin Configurations

The basis sets, pseudopotentials and spin configurations of the Co^{3+}, Co^{2+} and O^{2-} (as discussed in section 1.4) are as follows:

Table 3: Basis Sets, Pseudopotentials and Spin Configurations for Co^{3+} (type 1).

Keyword	**Setting**
KIND	Co1
ELEMENT	Co
BASIS_SET	DZVP-MOLOPT-SR-GTH
POTENTIAL	GTH-PBE-q17
DFT_PLUS_U	
L	2
U_MINUS_J	2.0 (eV)
ALPHA	
NEL	-1 -2
L	2 0
N	3 4
BETA	
NEL	-1 -2
L	2 0
N	3 4

Table 4: Basis Sets, Pseudopotentials and Spin Configurations for Co^{2+} (type 2).

Keyword	**Setting**
KIND	Co2
ELEMENT	Co
BASIS_SET	DZVP-MOLOPT-SR-GTH
POTENTIAL	GTH-PBE-q17
DFT_PLUS_U	
L	2
U_MINUS_J	2.0 (eV)
ALPHA	
NEL	+3 -2
L	2 0
N	3 4
BETA	
NEL	-3 -2
L	2 0
N	3 4

Table 5: Basis Sets, Pseudopotentials and Spin Configurations for Co^{2+} (type 3).

Keyword	**Setting**
KIND	Co3
ELEMENT	Co
BASIS_SET	DZVP-MOLOPT-SR-GTH
POTENTIAL	GTH-PBE-q17
DFT_PLUS_U	
L	2
U_MINUS_J	2.0 (eV)
ALPHA	
NEL	-3 -2
L	2 0
N	3 4
BETA	
NEL	+3 -2
L	2 0
N	3 4

Table 6: Basis Sets, Pseudopotentials and Spin Configurations for O^{2-}.

Keyword	**Setting**
KIND	O
BASIS_SET	DZVP-MOLOPT-SR-GTH
POTENTIAL	GTH-PBE-q6
ALPHA	
NEL	+2
L	1
N	2
BETA	
NEL	+2
L	1
N	2

Table 7: Basis Sets and Pseudopotentials for H and C atoms.

Keyword	**Setting**
KIND	C
BASIS_SET	DZVP-MOLOPT-SR-GTH
POTENTIAL	GTH-PBE-q4
KIND	H
BASIS_SET	DZVP-MOLOPT-SR-GTH
POTENTIAL	GTH-PBE-q1

A3. Simulation Cells and MD Settings

Table 8: Simulation cells for the (001), (111), and (110) surfaces.

Keyword	**Setting**
ABC (001)	16.177 16.177 50.0
ABC (111)	19.812 11.438 50.0
ABC (110)	22.877 16.177 50.0
MULTIPLE_UNIT_CELL	1 1 1
COORD_FILE_FORMAT	XYZ
COORD_FILE_NAME	initial_config.xyz

Table 9: MD settings in CP2K.

Keyword	**Setting**
ENSEMBLE	NVT
STEPS	40000
TIMESTEP	0.50
TEMPERATURE	300.0
COMVEL_TOL	1.0E-10
REGION	GLOBAL
TYPE	NOSE
TIMECON	100 (fs)

A4. Simulation Data

The simulation data utilized in this work can be accessed through the repository of the Faculty of Theoretical Chemistry at Universität Duisburg-Essen. The following categorization outlines the specific simulation data utilized in each chapter:

Chapter 5 Simulation Data

Co_3O_4 (001) Surface (section 5.2):

Directory:
Trieste:/Cache/aomranpoor/CobaltOxide/Simus/pure-2prop/

Simulation Names:
198_MD_A_8x2prop_Co2+_300K
199_MD_B_8x2prop_Co3+_300K
205_MD_A_8x2prop_Co2+_450K
206_MD_B_8x2prop_Co3+_450K
213_199_MD_B_8x2prop_1H_300K

Description:
198: 20 ps MD simulation consisted of 8 2-propanol molecules on the A-terminated (001) surface at 300 K (Reference System)
199: 20 ps MD simulation consisted of 8 2-propanol molecules on the B-terminated (001) surface at 300 K (Reference System)
205: 20 ps MD simulation consisted of 8 2-propanol molecules on the A-terminated (001) surface at 450 K
206: 20 ps MD simulation consisted of 8 2-propanol molecules on the B-terminated (001) surface at 450 K
213: 20 ps MD simulation consisted of 8 2-propanol molecules on the hydroxylated B-terminated (001) surface at 300 K

Co_3O_4 (111) Surface (section 5.3):

Directory:
Trieste:/Cache/aomranpoor/CobaltOxide/Simus/111/

Simulation Names:
214_MD_111_B_8x2prop_300K

228_MD_111_B_8x2prop_+8H_300K
229_MD_111_B_8x2prop_+8H_450K

Description:
214: 20 ps MD simulation consisted of 8 2-propanol molecules on the B-terminated (111) surface at 300 K (Reference System)
228: 20 ps MD simulation consisted of 8 2-propanol molecules on the hydroxylated B-terminated (111) surface at 300 K
229: 20 ps MD simulation consisted of 8 2-propanol molecules on the hydroxylated B-terminated (111) surface at 450 K

Co_3O_4 (110) Surface (section 5.4):

Directory:
Trieste:/Cache/aomranpoor/CobaltOxide/Simus/110/

Simulation Names:
203_MD_110_B_8x2prop_Co3+_300K
204_MD_110_B_8x2prop_Co3+_450K

Description:
203: 20 ps MD simulation consisted of 8 2-propanol molecules on the B-terminated (110) surface at 300 K (Reference System)
204: 20 ps MD simulation consisted of 8 2-propanol molecules on the B-terminated (110) surface at 450 K

Power Spectra – 2-propanol gas molecule (section 5.6):

Directory:
Trieste:/Cache/aomranpoor/CobaltOxide/Simus/gas-phase/

Simulation Name:
267_MD__gas-phase_1x2prop_300K

Description:
267: 70 ps MD simulation of a single 2-propanol gas molecule (to be used as the reference spectrum)

Chapter 6 Simulation Data

2-propanol Oxidation in Liquid-phase (section 6.2):

Directory:
Trieste:/Cache/aomranpoor/CobaltOxide/Simus/2-propanol/long-run/20ps/

Simulation Names:
133_MD_B_1x2prop_Co3+_+60WM_300K_Ref
131_MD_B_1x2prop_Co3+_+60WM_-8H_300K
134_MD_A_1x2prop_Co2+_+60WM_300K_Ref
135_MD_A_1x2prop_Co2+_+60WM_-8H_300K
136_MD_B_1x2prop_Co3+_+60WM_450K
137_MD_A_1x2prop_Co2+_+60WM_450K

Description:
133: 20 ps MD simulation consisted of a single 2-propanol molecules + 60 water molecules on the B-terminated (001) surface at 300 K (Reference System)
131: 20 ps MD simulation consisted of a single 2-propanol molecules + 60 water molecules on the B-terminated (001) surface at 300 K (8 H atoms are removed from the system)
134: 20 ps MD simulation consisted of a single 2-propanol molecules + 60 water molecules on the A-terminated (001) surface at 300 K (Reference System)
135: 20 ps MD simulation consisted of a single 2-propanol molecules + 60 water molecules on the A-terminated (001) surface at 300 K (8 H atoms are removed from the system)
136: 20 ps MD simulation consisted of a single 2-propanol molecules + 60 water molecules on the B-terminated (001) surface at 450 K
137: 20 ps MD simulation consisted of a single 2-propanol molecules + 60 water molecules on the A-terminated (001) surface at 450 K

2-propanol Oxidation in Gas-phase (section 6.3 - 6.5):

Directory:
Trieste:/Cache/aomranpoor/CobaltOxide/Simus/TC/

Simulation Names:
194_MD_B_8x2prop_8xO_300K_2
193_MD_B_8x2prop_8xO_700K

Description:

194: 20 ps MD simulation consisted of 8 2-propanol molecules + 8 atomic Oxygen on the B-terminated (001) surface at 300 K (Reference System)
193: 20 ps MD simulation consisted of 8 2-propanol molecules + 8 atomic Oxygen on the B-terminated (001) surface at 700 K

Chapter 4 Simulation Data

Directory:
Trieste:/Cache/aomranpoor/CobaltOxide/Simus/Bulk/

Simulation Names:
272_MD_Bulk_300K

Description:
272: 72 ps of MD simulation consisted of the bulk Co_3O_4 spinel at 300 K

Acknowledgements

I am deeply grateful to Prof. Dr. Eckhard Spohr for his invaluable support throughout my Ph.D. studies. His guidance has played a pivotal role in shaping my research journey. I want to express my sincere appreciation for Prof. Spohr's unwavering support in allowing me the freedom to explore various research directions while always being available for in-depth scientific and technical discussions.

I would also like to extend my gratitude to Dr. Stephane Kenmoe for the insightful discussions we have had over the past three years, particularly in helping me grasp the broader picture of my research. Additionally, I am thankful to Tim Kox for providing the initial simulation systems, offering numerous chemical insights during our discussions, and collaborating during the teaching of the "Numerical Methods in Theoretical Chemistry" course. I also want to express my sincere thanks to all other members of Prof. Spohr's group, especially Dinah Tiets (secretary), and Torsten de Montigny (technical support) for their help with the administrative paperwork and technical issues, respectively.

Furthermore, I would like to acknowledge the financial support provided by the International Max Planck Research School (IMPRS-SurMat) throughout my Ph.D. work.